ADVANCED ELECTRIC PROPULSION RESEARCH

Prepared for

LEWIS RESEARCH CENTER

NATIONAL AERONAUTICS AND SPACE ADMINISTRATION

Grant NGR-06-002-112

Annual Report

January 1988

Paul J. Wilbur
Department of Mechanical Engineering
Colorado State University
Fort Collins, CO 80523

TABLE OF CONTENTS

LIST OF FIGURES

HOLLOW CATHODES FOR ARCJET THRUSTERS

An experimental study designed to determine the suitability of hollow cathodes as electron sources for arcjets was completed during this grant period. The tests, which were conducted using ammonia propellant and a wide variety of hollow cathode designs, had the general objective of demonstrating whether or not hollow cathodes could be operated reliably in the high pressure (of order 1000 Torr) regime where arcjet thrusters operate. Although operation of the cathodes was demonstrated on ammonia and several guidelines were identified that facilitated operation at high pressures for short periods of time, reliable hollow cathode operation at high pressure was not demonstrated. A description of the tests conducted together with the results obtained and conclusions drawn from the tests were organized into a paper that was presented during the grant period. A copy of that paper is included as Appendix A to this report.

CONSTRAINED-SHEATH OPTICS FOR HIGH THRUST DENSITY, LOW SPECIFIC IMPULSE ION THRUSTERS

The concept of using a contoured, fine wire mesh attached to the screen grid as a means of controlling the focusing of ion beamlets emerging from ion thrusters operating at low net-to-total accelerating voltage ratios was investigated experimentally during this grant period. Comparative tests conducted using free and constrained-sheath ion optics systems suggested that the constraining sheath facilitated operation at lower accelerator grid impingement currents, to higher perveance levels and with slightly less divergent beamlets than those produced using the conventional free-sheath scheme. Results suggest

additional gains in optical performance might be realized by optimizing the shape of the constraining mesh. In the course of conducting this work a new concept that can be used to probe ion beamlets emerging from extraction grids was identified. The usefulness of this probing concept, which can be used to study the structure and focusing characteristics of ion beamlets as the parameters associated with their formation, was demonstrated. The details of this work were described in a paper presented during the grant period. A copy of that paper is included as Appendix B to this report.

8 CM DIA RING CUSP DISCHARGE CHAMBER RESEARCH

Jason Vaughn

INTRODUCTION

A study conducted by Hiatt[1] on a specially designed 8 cm diameter ring-cusp ion source demonstrated some conditions that had to be met in order to realize good discharge chamber performance. In that study good performance was realized when 1) the surface of revolution of the innermost magnetic field line that intercepted the anode (i.e. the virtual anode field line) also intercepted the outermost holes in the screen grid and 2) the surface of revolution of the outermost field line that intercepted the outer boundary of the electron source (i.e. the virtual cathode field line) was located relative to the virtual anode so the discharge was on the threshold of extinction at the prevailing discharge voltage. By operating so that these criteria were met, Hiatt was able to demonstrate operation on argon at beam ion energy cost/propellant utilization efficiency conditions that were particularly attractive for the small discharge chamber he used in his study.

Hiatt's results were, however, obtained on an ion source that utilized a refractory metal filament cathode located downstream of the ring cusp near the screen grid. In order to make those results more useful it is desirable that similar criteria be defined for discharge chamber designs that utilize a hollow cathode rather than a refractory metal filament electron source. This is desirable because hollow cathodes are needed in space applications where long lifetime operation and prelaunch testing to assure good performance are required. Since hollow cathodes have generally been located on the

centerline near the upstream ends of discharge chambers, it was felt that this study should focus on this hollow cathode location at least for preliminary phases of the study.

The objective of this study had been to identify criteria that assure operation of a discharge chamber utilizing a hollow cathode at peak performance conditions. In order to maximize the understanding of discharge phenomena being sought, this objective has been undertaken in two steps. First, the performance-related effects of moving a refractory metal filament cathode from downstream to upstream of the ring cusp were studied and then the effects of changing the size and axial location of this filament cathode were studied. Next, the performance-related effects induced by replacing this upstream filament cathode with a hollow cathode and changing its axial position and the parameters associated with operation were investigated.

THEORY

Experimental results obtained in this study will be analyzed in terms of the discharge chamber model developed by Brophy.[2] Specifically, the experimentally measured performance will be described using plasma ion energy cost vs. discharge chamber neutral density plots and the extracted ion fraction (f_B) data that are used in this model to characterize discharge chambers. In order to do this, plasma ion energy cost data (ϵ_p) will be measured in a discharge chamber when it is operating at an argon flowrate ($\dot{m}$) as a function of propellant utilization efficiency (η_u). It should be noted that the argon flowrate sought is the true flowrate, i.e. the one that accounts for neutral atom backflow from the vacuum system through the ion optics system. Once the plasma ion energy cost/utilization efficiency

data are obtained, they will be used in a non-linear, least-squares computer program to find values of the parameters ϵ_P^* (the baseline plasma ion energy cost) and C_0 (the primary electron utilization factor) that assure the best fit of the data to the equation

$$\epsilon_P = \epsilon_P^* \left\{1-\exp[-C_0\dot{m}(1-\eta_u)]\right\}^{-1} \quad . \tag{1}$$

The primary electron utilization factor, which appears in this equation, is a parameter that describes the probability that primary electrons coming from the cathode will have an inelastic (excitation or ionization) collision before it reaches an anode surface and is lost. The baseline plasma ion energy cost is the average energy required to produce a ion in the discharge chamber when the neutral atom density is sufficiently high so that all primary electrons have inelastic collisions before they can reach the anode. Ideally, the baseline plasma ion energy cost is determined by the propellant, the discharge voltage and the potential from which electrons are drawn into the discharge chamber (cathode potential for a filament cathode or internal plasma potential for a hollow cathode). This ideal situation is realized, however, only if the production rate for all of the ions can be measured. In the apparatus used in these tests an effort has been made to minimize the discharge chamber ion production current that cannot be measured, but there are ions that are lost to anode and cathode surfaces that do escape measurement. Thus, increases in the baseline plasma ion energy cost that cannot be related to changes in discharge voltage, propellant, or electron source potential are assumed to reflect an increase in the rate at which discharge chamber plasma ions are escaping measurement.

Generally, such increases are induced by ions reaching either the hollow cathode or the ring cusp anode because the areas of other cathode and anode surfaces exposed to the plasma are sufficiently small so losses to them should be negligible.

The complete performance model proposed by Brophy also requires determination of the fraction of the ions produced in the discharge chamber that are extracted from the discharge chamber into the ion beam (f_B) and this quantity can be computed directly using measured ion currents. Once the three parameters describing a discharge chamber (ϵ_P^*, C_0 and f_B) have been determined from experimental data obtained at a discharge voltage V_D, the discharge chamber performance [the beam ion energy cost (ϵ_B) vs. propellant utilization efficiency (η_u) plot] can be computed using

$$\epsilon_B = \frac{\epsilon_P^* \left\{1-\exp[-C_0\dot{m}(1-\eta_u)]\right\} + (1-f_B)\ V_D}{f_B} \quad . \tag{2}$$

The advantage of presenting data in terms of the discharge chamber model reviewed in the above paragraphs is that one can generally identify specific reasons why hardware changes induce changes in the discharge chamber performance. For example, one can determine if a detrimental change causes performance to degrade because of increased losses of primary electrons to the anode (a decrease in the value of C_0), increased losses of ions to the hollow cathode (an increase in the value of ϵ_P^*) or increased losses of ions to some other discharge chamber surface (a decrease in the value of f_B). Further, because the ion loss currents to all surfaces but those of the anode and cathode

are measured, the specific surface(s) to which the ion losses are occurring is (are) also known.

The effects that induce changes in C_0 and f_B mentioned in the preceeding paragraph have been demonstrated by Brophy, but his tests did not involve use of a hollow cathode so some discussion of the suggestion that increases in the value of the baseline plasma ion energy cost (ϵ_p^*) reflect increased ion losses to a hollow cathode is considered desirable. In Brophy's work the value of (ϵ_p^*) was found to be determined by the propellant being used and the discharge voltage, and if these two variables were held constant it was found that (ϵ_p^*) did not change. There were, however, ions that were produced and then lost to anode and cathode surfaces in Brophy's apparatus and these ion currents could not be measured. The cost of producing these unmeasured ions appears in the data as an increase in the apparent cost of producing the ions that are measured, but in Brophy's tests the area of the cathode and anode surfaces to which these unmeasured ion losses could occur was considered to be small compared to the area of surfaces to which ion currents could be measured. In some of the tests to be described the exposed anode area fraction is probably similar to that in Brophy's apparatus, but a hollow cathode was used in place of a filament cathode. This causes two changes that are important. First, power required to operate the cathode (i.e. ion production occurs upstream of the cathode orifice) and second, substantial ion production probably occurs in the high neutral density environment immediately downstream of the orifice plate and many of these ions are probably drawn back into the cathode. Theoretically, these losses could be accounted for by modeling the primary electron production and acceleration process in two steps and then using only

the power associated with acceleration to compute plasma ion energy costs. Unfortunately, in the present experiments the potential difference associated with the production process cannot be defined reliably so it is not possible to separate these primary electron production and acceleration processes. Because the ion losses to the hollow cathode are typically significant and cannot be separated out they cause a general increase in the baseline plasma ion energy cost associated with the currents of ions that are measured. Changes in ion losses to the hollow cathode can therefore cause the value of (ϵ_p^*) to increase. When a discharge chamber is being operated at a constant discharge voltage on one propellant and the effective anode area on which ions are collected is small as it should be in the tests being described here, changes in (ϵ_p^*) should reflect losses associated with the hollow cathode.

APPARATUS AND PROCEDURE

Upstream Filament Cathode Thruster Configuration

The ring cusp ion source being used to study the effects of changes in the axial position and size of a refractory metal filament cathode located in the upstream end of the discharge chamber is shown schematically in Fig. 1. It has a nominal interior diameter of 8 cm so this represents the maximum diameter of the beam that can be extracted from it. It is designed, however, to be a flexible research tool, so the lengths and diameters labeled in Fig. 1 can all be varied from one test to the next and the cathode can be moved axially during the conduct of a test by turning the lead screw shown. It should be noted that the ring cusp magnet and discharge chamber backplate are located relative to the screen grid (using ℓ_r and ℓ_d) while the

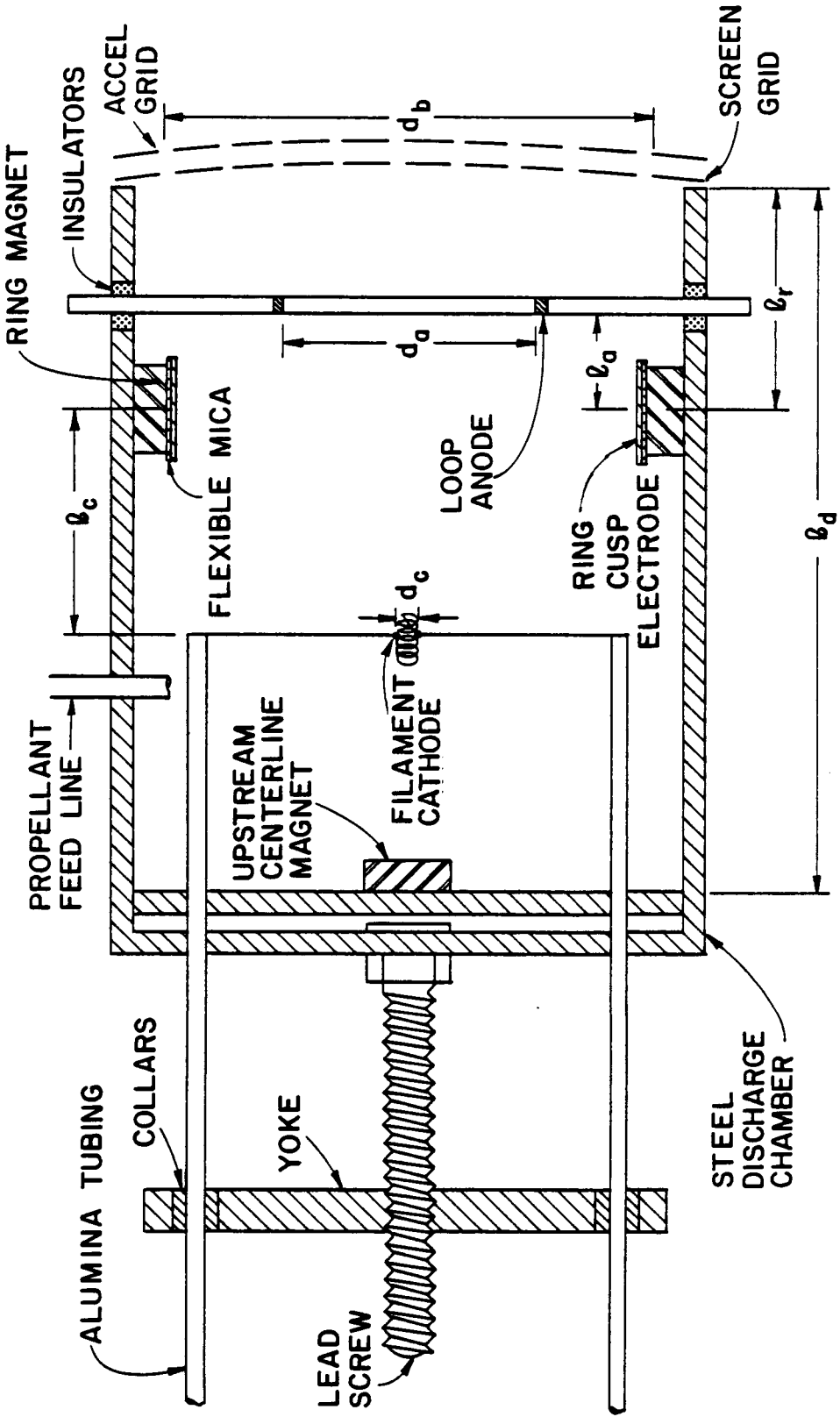

Fig. 1. Ring Cusp Discharge Chamber with Upstream Filament Cathode

cathode and loop anode are located relative to the ring cusp (using ℓ_c and ℓ_a). The magnetic field in the ring cusp discharge chamber is created by placing a single 1.9 cm by 1.3 cm by 0.5 cm samarium cobalt magnet at the upstream end of the discharge chamber and by placing a row of similar magnets end-to-end around the inner circumference of the chamber wall. The magnets have a flux density of 0.27 Tesla at their surface, and they are arranged so that the outward facing surface of the ring magnet is opposite in polarity to that of the single upstream magnet.

The filament cathode shown schematically in Fig. 1 has the configuration of a constant pitch helix having its axis coincident with the thruster centerline. It is made of 0.025 cm dia. tungsten wire and it has a major diameter d_c. The total length of wire used to make this helix was kept constant so a large diameter coil might have only a single turn of wire while a small diameter coil would have many turns. The filament cathodes were heated to thermionic emission temperatures by passing currents of the order of 10 A a.c. through them. Under the action of the lead screw and yoke, the filament cathode could be moved through axial positions from that of the ring cusp to one a few centimeters downstream of the backplate. Two anodes were used in conducting the tests; one (the loop anode) is a torroid with its axis coincident with that of the thruster, and the other anode (called the ring cusp electrode in Fig. 1 because it was biased at other than anode potential on some occasions) is located on the ring magnet surface. The ring cusp electrode was made of 0.025 cm thick stainless steel placed directly over the ring magnets but insulated electrically from them with a layer of flexible mica. It was held in place magnetically by small (~2 mm by 1 cm by 0.12 mm

thick) pieces of mild steel spot welded to the surface of the stainless steel strip and located between the surfaces of the electrode and magnet. The loop anode, which was made of copper, was fixed at an axial location 1.7 cm downstream of the ring magnet cusp and its diameter (d_a) was changed between 4.1 cm and 4.9 cm in the course of conducting the tests. The ring cusp and loop anodes were wired so either or both of these surface could be switched to anode potential while the ion source was operating.

The dished high perveance grid set used in the study had a cold spacing of 0.85 mm; the accel and screen grid holes were 1.5 mm and 1.9 mm in diameter, respectively, and the hole-to-hole spacing was 2.2 mm. Constant screen and accel grid voltages of 750 V and -250 V, respectively, were maintained for all tests. A 46 cm dia. bell jar diffusion pumped to a baseline pressure in the low 10^{-6} Torr range provided the testing environment. Typical background operating pressures corrected for the ionization pressure gauge sensitivity to the argon propellant being used were in the mid to low 10^{-4} Torr range. All discharge chamber neutral density data and mass flowrate measurements were corrected for propellant back flow through the grids at the prevailing background pressure. This back flowrate was computed as the free-molecular flowrate of argon through a sharp-edged orifice having an area equal to the open area of the accel grid driven by the prevailing vacuum bell jar argon pressure. The thermal velocity assigned to the argon atoms in the vacuum bell jar was based on the assumption that they had come into equilibrium with bell jar surfaces at an assumed temperature of 300 K.

Figure 2 is an electrical schematic diagram that shows where voltage and current measurements were made and how power supplies were

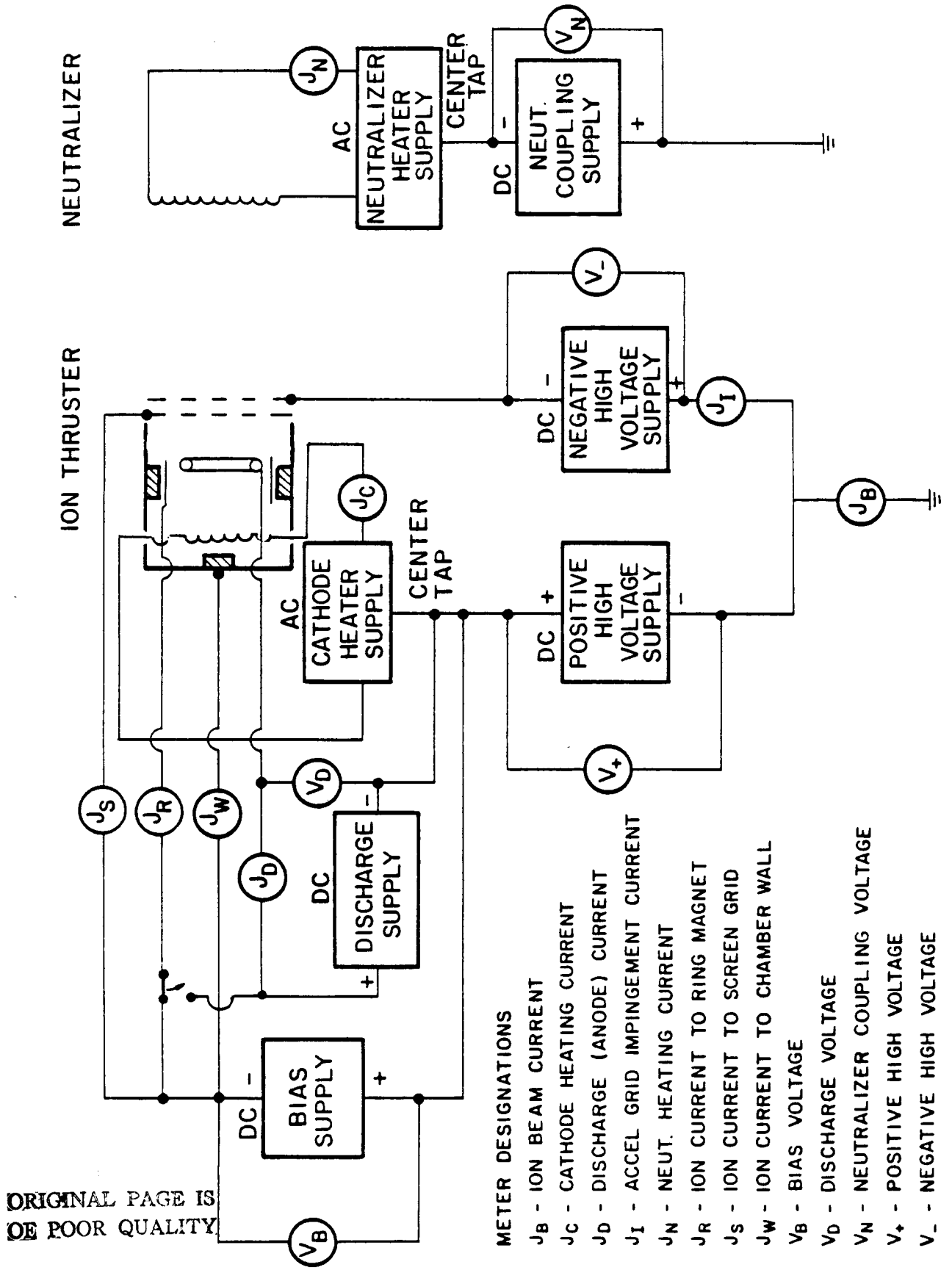

ORIGINAL PAGE IS
OE POOR QUALITY

connected for all of the tests conducted using the filament cathode. As the figure suggests, a refractory metal filament neutralizer placed directly across the ion beam was used to accomplish ion beam neutralization. The bias power supply shown in Fig. 2 was used to bias the discharge chamber walls and screen grid negative of the cathode so electrons would be repelled from these surfaces and the ion currents to them (J_W and J_S) could be measured. The thruster shown in Fig. 2 was also wired so the electrode on the surface of the ring magnet could be connected to the bias supply when it was not being used as an anode so the ion current being drawn to it (J_R) could be measured. When this electrode was to be used as an anode the wire connected to it was switched to the positive terminal of the discharge power supply. The sum of all of the ion currents drawn to the bias power supply plus the beam current is the measured total ion production rate (J_P) and it differs from the true ion production rate only to the extent that ions produced in the chamber escape measurement by going to anode and cathode surfaces.

The basic procedure for tests conducted using the upstream filament cathode began by establishing an argon flowrate of 500 mA eq, starting and then stabilizing the discharge at a discharge voltage (V_D) of 50 V. When operation was stable, the discharge current (J_D) was varied in increments over a range from 0.2 to 1.5 A. At each discharge current condition, the beam current (J_B) and ion currents going to the walls, screen grid and if appropriate the ring cusp surface were measured by biasing the surface of interest 30 V below cathode potential to repel all electrons approaching it so the true ion current to it would be measured. After the data had been recorded at a given argon flowrate and anode configuration (loop, ring cusp or

both) another flowrate and/or anode configuration was set and the data collection process was repeated. When the flow conditions of interest had all been investigated the filament position was changed; similar data were collected at each filament cathode position. After the entire range of positions had been investigated (i.e. ℓ_c had been varied through the range 0 cm to 2.5 cm), the source was removed from the chamber, a cathode filament having a different major diameter was installed and data collection at the axial cathode positions and argon flowrates of interest were repeated. Tests were conducted using helical cathodes with major diameters (d_c) of 0.2, 0.5, 1.4, 2.3, and 3.2 cm. It is noted that early tests showed that the discharge could not be sustained with a 50 V anode voltage when the loop anode was used alone so essentially no data were collected using this anode configuration with the upstream filament cathode. The effects of changing between the anode configurations at which operation could be sustained were investigated using a filament cathode with a diameter (d_a) of 0.2 cm located 2.5 cm upstream of the ring cusp (ℓ_c = 2.5 cm).

Hollow Cathode Thruster Configuration

Although several ring cusp magnetic field configurations were investigated in the course of studying the effect of the hollow cathode on the performance of the 8 cm dia. ring cusp ion source only the one shown in Fig. 3 produced data that are considered of interest. For example, some tests were conducted using a magnet located around the hollow cathode on the backplate, but this magnet induced such high magnetic fields at the hollow cathode (~500 gauss) that keeper voltages of about 50 V were required to sustain significant keeper currents. The ring magnet, formed using samarium cobalt magnets

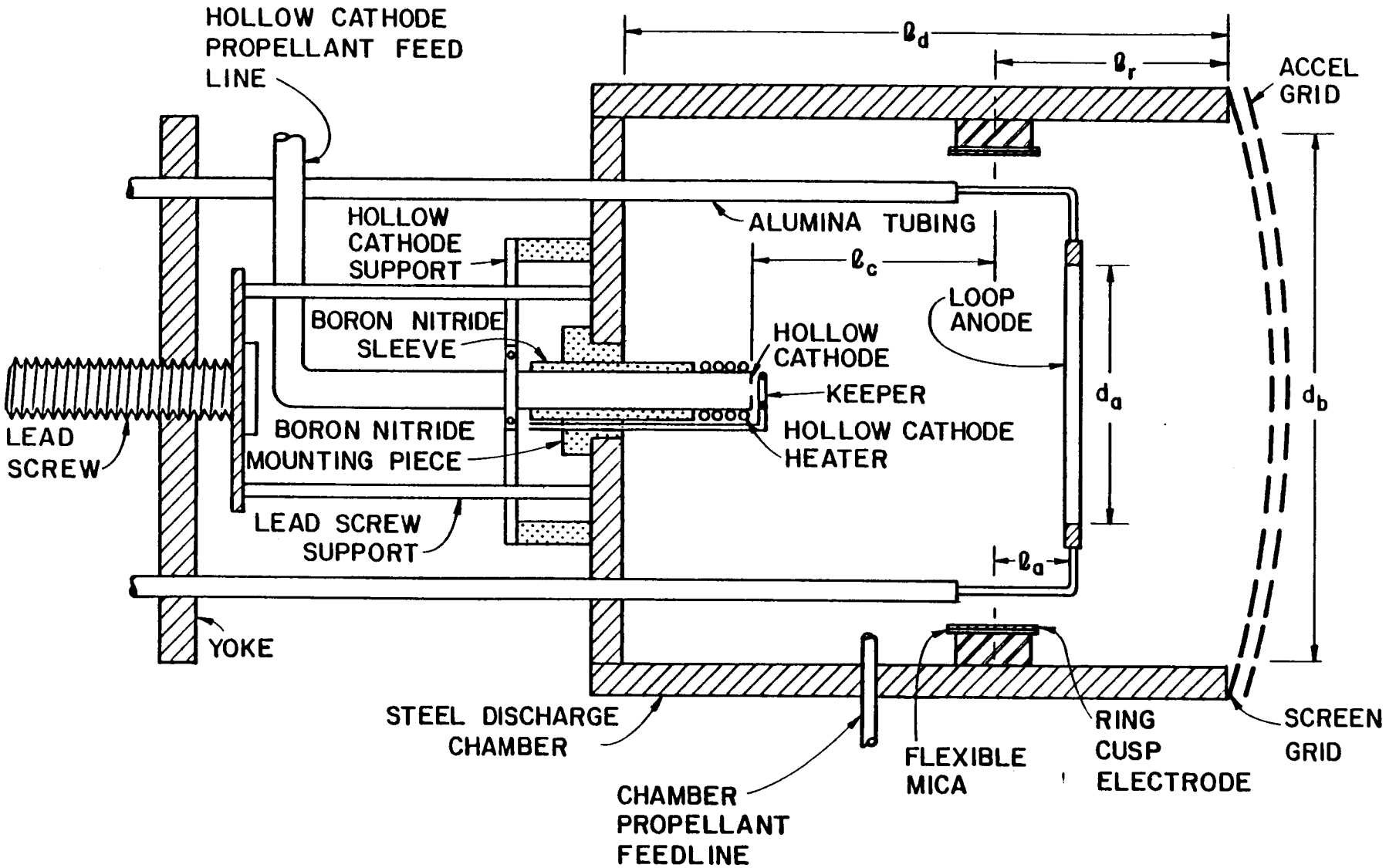

Fig. 3. Ring Cusp Discharge Chamber with Hollow Cathode

arranged end-to-end in the same way as the one used in the filament cathode test, was located a distance ℓ_r (generally about 7.5 cm) upstream of the screen grid. For the hollow cathode tests the lead screw apparatus was modified so it could be used to move the 5.2 cm dia. copper loop anode shown in Fig. 3 from positions just upstream of the ring cusp to ones approximately 1.5 cm downstream of it. As in the case of the filament cathode described previously the ring cusp electrode was designed so it could serve either as an anode or a surface to which an ion loss current could be measured.

The 0.64 cm dia. hollow cathode used in the tests (a tantalum tube welded to a thoriated tungsten orifice plate with a 0.7 mm dia. orifice in it) is shown in Fig. 4. The cathode was mounted in the boron nitride sleeve/plate assembly, shown in this figure, so it could be moved axially from test to test and yet be insulated from the discharge chamber walls, which were biased relative to the cathode to facilitate ion current measurement. This boron nitride assembly was sufficiently leak tight so propellant leakage past it and into the vacuum chamber was negligible. The hollow cathode utilized a rolled tantalum foil insert treated with Chemical R 500* and it was heated to thermionic emission temperatures by the swaged heater shown in Fig. 4. Measured propellant flows were fed into the discharge chamber through both the hollow cathode and chamber wall port shown in Fig. 3. A torroidal keeper electrode, which was needed in some tests to sustain the discharge, was supported from the boron nitride mounting plate in such a way that it was insulated from both the hollow cathode and the discharge chamber walls. The keeper had a 0.32 cm inner diameter and

*Chemical R-500 is a double carbonate ($BaCO_3$, $SrCO_3$) mixture that has been manufactured by the J. R. Baker Chemical Co., Phillipsburg, NJ, but is no longer made.

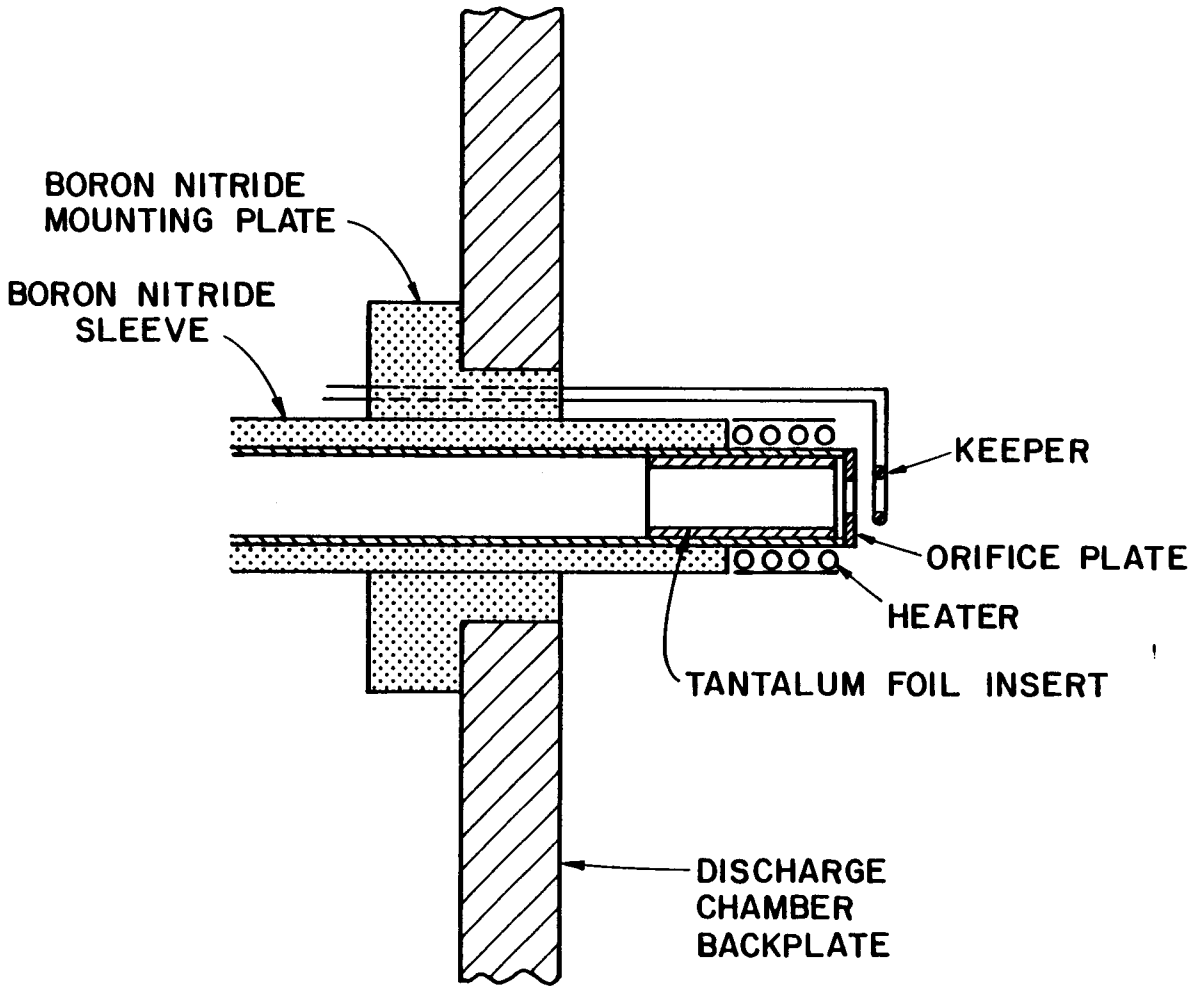

Fig. 4. Hollow Cathode Schematic

was positioned 1 mm downstream of the hollow cathode orifice plate. The grid system and vacuum facility used to conduct tests with the hollow cathode were the same as those used to conduct tests with the upstream filament cathode.

Figure 5 is an electrical schematic showing where voltage and current measurements are made and how power supplies were connected to the discharge chamber and the hollow cathode for these tests. This schematic is similar to the one used for the filament cathode study except for the inclusion of the keeper power supply. For some tests this power supply was turned off and the keeper was allowed to float so the effect of the keeper discharge on discharge chamber performance could be studied.

This study also included an investigation of the performance-related effects induced by changing the relative locations of the ring cusp magnet and cathode and by changing the magnetic flux density level in the chamber. Generally, the ring magnet (composed of 1.9 by 1.3 by 0.5 cm elements) was moved to change relative positions of the cathode and ring magnet although the cathode was moved in some tests. The magnetic flux density was changed for one test only by substituting a ring composed of small magnet elements (1.2 by 0.6 by 0.5 cm) for the standard ring of larger ones. The small magnet elements produced the same flux density (0.27 Tesla) at their surfaces as the large one did, but because they were smaller in size they induced lower flux density levels throughout the discharge chamber.

The basic procedure used to test the hollow cathode thruster was to establish a 500 mA eq (Ar) total flowrate (i.e. the sum of the flowrates associated with the hollow cathode, discharge chamber body and grid backflow) and start the discharge by applying a voltage to

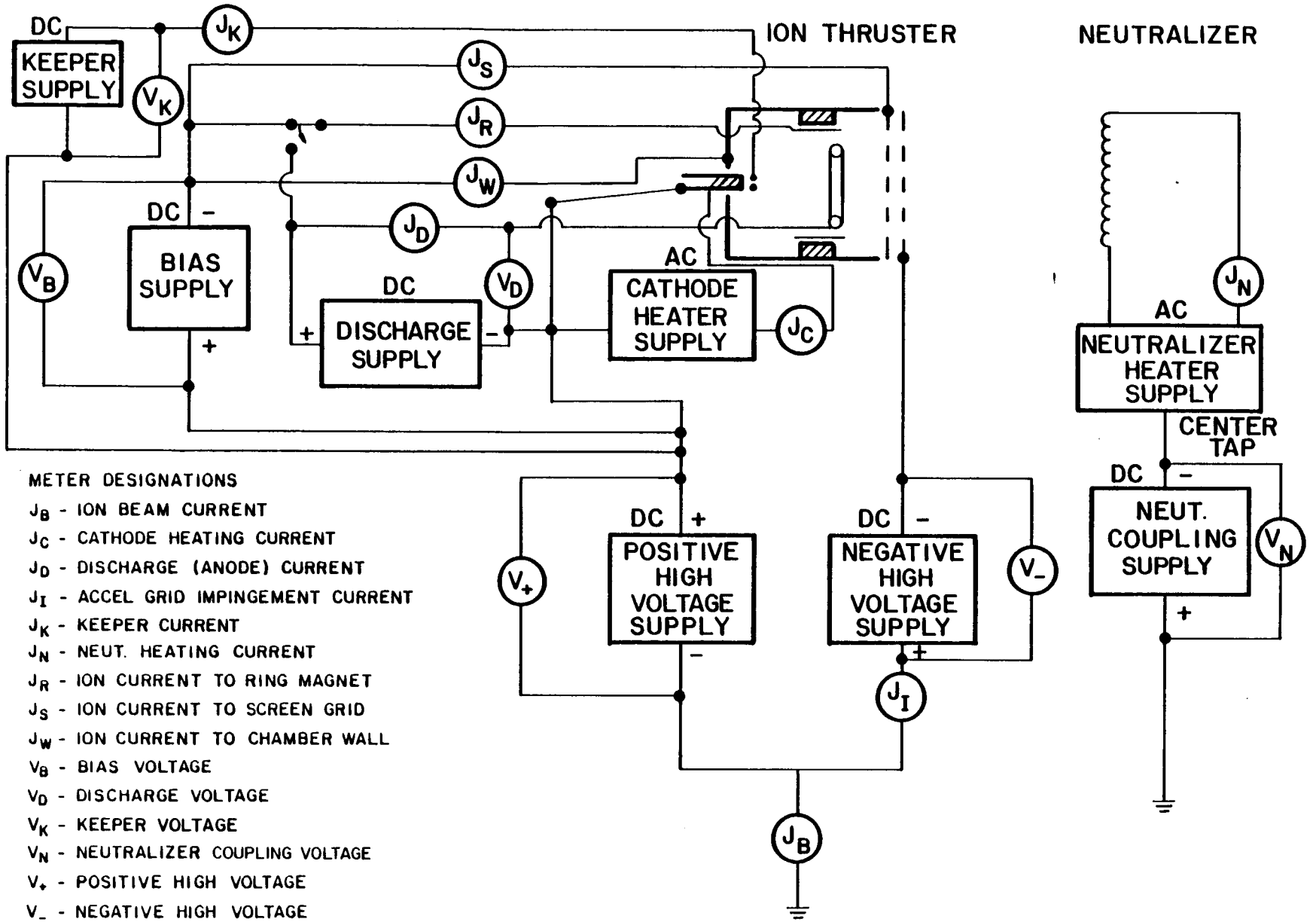

Fig. 5. Electrical Schematic - Hollow Cathode Thruster Configurations

the keeper and loop anode. Frequently, electrons were backstreamed from the neutralizer by applying a high voltage to the discharge chamber to facilitate discharge ignition. The discharge was then allowed to stabilize at the desired discharge voltage (V_D) which was generally 50 V.

It is noted at this point that the hollow cathode thruster operated differently than the filament cathode thrusters. In the downstream filament cathode thruster,[1] movement of the loop anode onto field lines located successively further from the thruster centerline caused the performance of a discharge chamber, operating at a fixed discharge voltage and relatively constant discharge current, to improve until the point was reached where the discharge went out. With the upstream filament, thruster operation could not be sustained when the loop anode was being used alone so the effect of loop anode position on discharge chamber operation in this case is unknown. In the hollow cathode thruster operating at a fixed discharge current and cathode flowrate condition, the discharge voltage would increase as the loop anode was moved onto field lines located successively further from the thruster centerline, but the discharge would not go out as it did with the downstream filament cathode. When the thruster was operating using a downstream filament cathode the discharge voltage remained constant as discharge current and propellant flowrate were changed but this was not the case with the hollow cathode thruster. In this case the discharge voltage could be changed by adjusting the discharge current, the cathode flowrate or the axial position of the loop anode (ℓ_a). Hence, operation at fixed discharge voltage and cathode flowrate conditions could be achieved by adjusting the loop anode position to control discharge voltage as discharge current was changed.

When the keeper was used in the hollow cathode discharge chamber tests the current to it was generally set at 0.3 A. Discharge currents (J_D) were varied through the range from 0.1 to 1.5 A, and at each discharge current condition the discharge voltage (V_D), keeper current (J_k), keeper voltage (V_k), beam current (J_B) and ion current to various surfaces (screen (J_S), chamber walls (J_W) and ring cusp (J_R)) were measured using procedures like those described for the upstream filament cathode tests. The measured ion production current (J_P) was determined by summing the ion current to these surfaces with the beam current. After the data of interest had been collected a new argon flowrate through the hollow cathode could be established and the data collection process could be repeated although all data presented here were collected at one cathode flowrate (95 mA eq). The data were generally collected at a discharge voltage of ~50 V so they could be compared to data collected using the upstream filament cathode and to data collected by Hiatt using the downstream filament cathode.

Data collected using either the filament or hollow cathode discharge chambers were converted into plasma ion energy costs (ϵ_P) and extracted ion fractions (f_B) using the following equations.

$$\epsilon_P = \frac{(J_D - J_P)\ V_D + J_k\ V_k}{J_P} \tag{3}$$

$$f_B = \frac{J_B}{J_P} \tag{4}$$

If the keeper was either floating or not present during a test, as in the cases where a filament cathode was used, the keeper power term in Eq. 3 was obviously zero and the equation reduced to the same equation

as the one used by Hiatt[1] and Brophy.[2] The neutral density parameter $[\dot{m}(1-\eta_u)]$, which is proportional to discharge chamber neutral atom density, is also used in presenting the data that describe discharge chamber performance. This parameter is determined by subtracting the beam current (J_B) from the total propellant flowrate ($\dot{m}$).

RESULTS

The standard of comparison for data obtained using the 8 cm dia. ring cusp discharge chamber equipped with filament and hollow cathodes located upstream of the ring cusp are the data obtained by Hiatt.[1] He optimized the performance of the same basic thruster used in these tests using a downstream filament cathode and loop anode by moving the loop anode toward the grids until the discharge was on the verge of going out. This resulted in the plasma ion energy cost vs. neutral density parameter data represented by the circular symbols and the solid line in Fig. 6. These data were collected while the discharge chamber was operating at a 50 V discharge voltage on argon with the chamber configured as indicated by the dimensions listed in the legend. Also shown in this figure are data (represented by the square symbols and the dashed line) collected when the ring cusp anode was used in place of the loop anode. The values of the parameters listed by each curve have been obtained using Eqs. 3 and 4 and by performing a least squares curve fit of the data points shown to Eq. 1. It should be noted that the major difference in the performance associated with these two anode configurations is reflected in the difference in their associated primary electron utilization factors (C_0). The fact that the value of this parameter is substantially lower for the ring cusp anode thruster indicates that its anode is

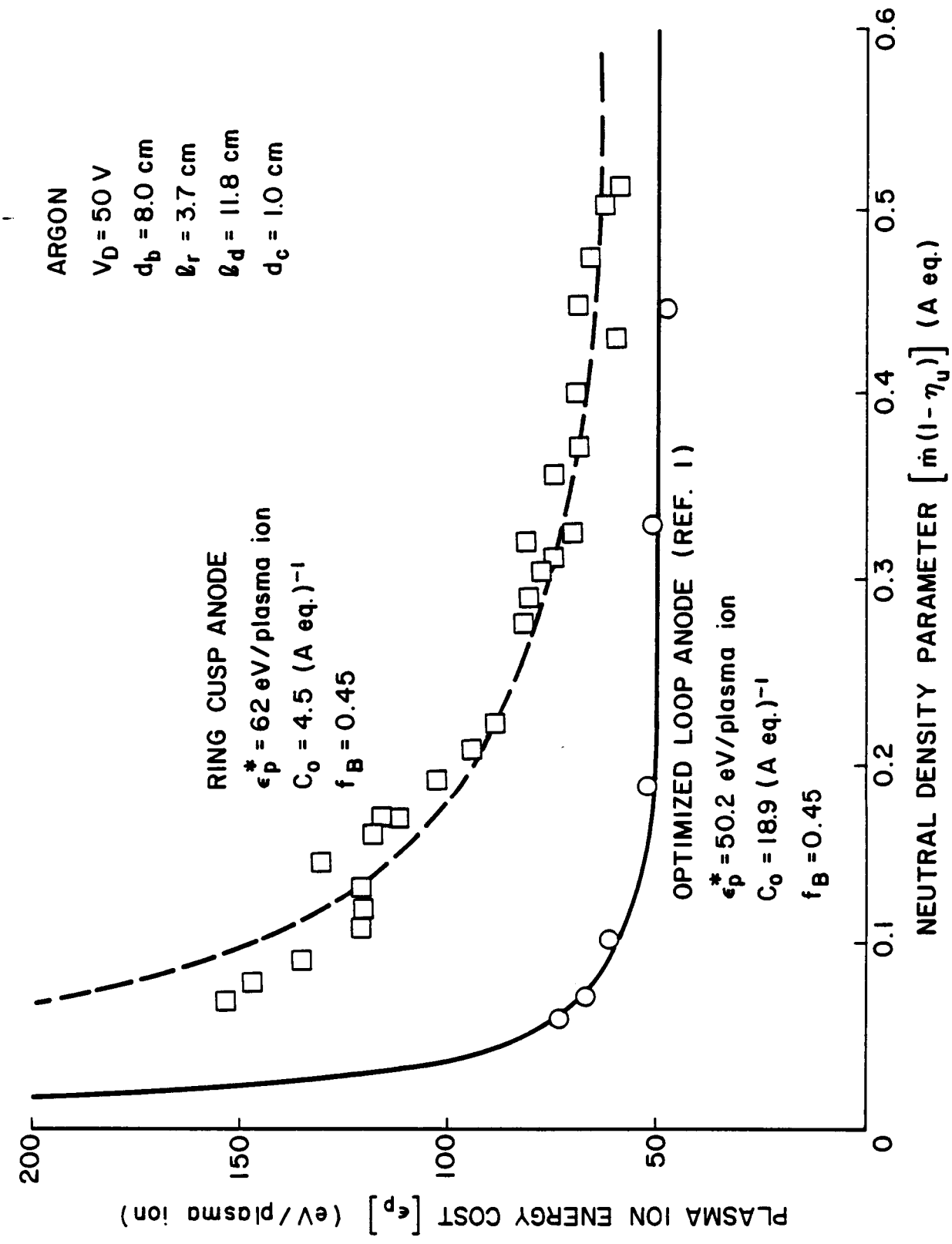

Fig. 6. Performance with Downstream Filament Cathode

collecting a larger fraction of the primary electrons that could be producing ions than is the anode of the optimized loop anode thruster.

Filament Cathode Located Upstream of the Ring Cusp

When the filament cathode was moved from the locations downstream of the ring cusp used by Hiatt to ones upstream of it, the discharge could generally not be sustained using only the loop anode configured as shown in Fig. 1. This is unfortunate because it indicates operation using the ring cusp anode is required and the data of Fig. 6 suggest that a substantial degradation in performance can be expected when the ring cusp anode is used in place of the loop anode. Figure 7 compares plasma ion energy cost/neutral density parameter data obtained with the upstream and downstream filaments operating with the ring cusp anode and they are seen to be almost identical. Because the curve fit parameters C_0 and ϵ_p^* for these two cases agree quite well it can be said that moving the filament cathode upstream did not cause the characteristics associated with primary electron utilization or ion losses to anode and cathode surfaces to change significantly. The fact that f_B, the extracted ion fraction, is substantially higher when the filament is downstream (0.45 compared to 0.20 for the upstream filament) does indicate, however, that ions are extracted into the beam much more readily when the filament cathode is downstream close to the grids.

The magnetic field environment in which the effects illustrated in Figs. 6 and 7 were observed is shown in Fig. 8. With the filament cathode located 2 cm downstream of the cusp, the iron filings map (Fig. 8a) and the centerline flux density profile (Fig. 8b) both suggest it would be in a region where the flux density drops off

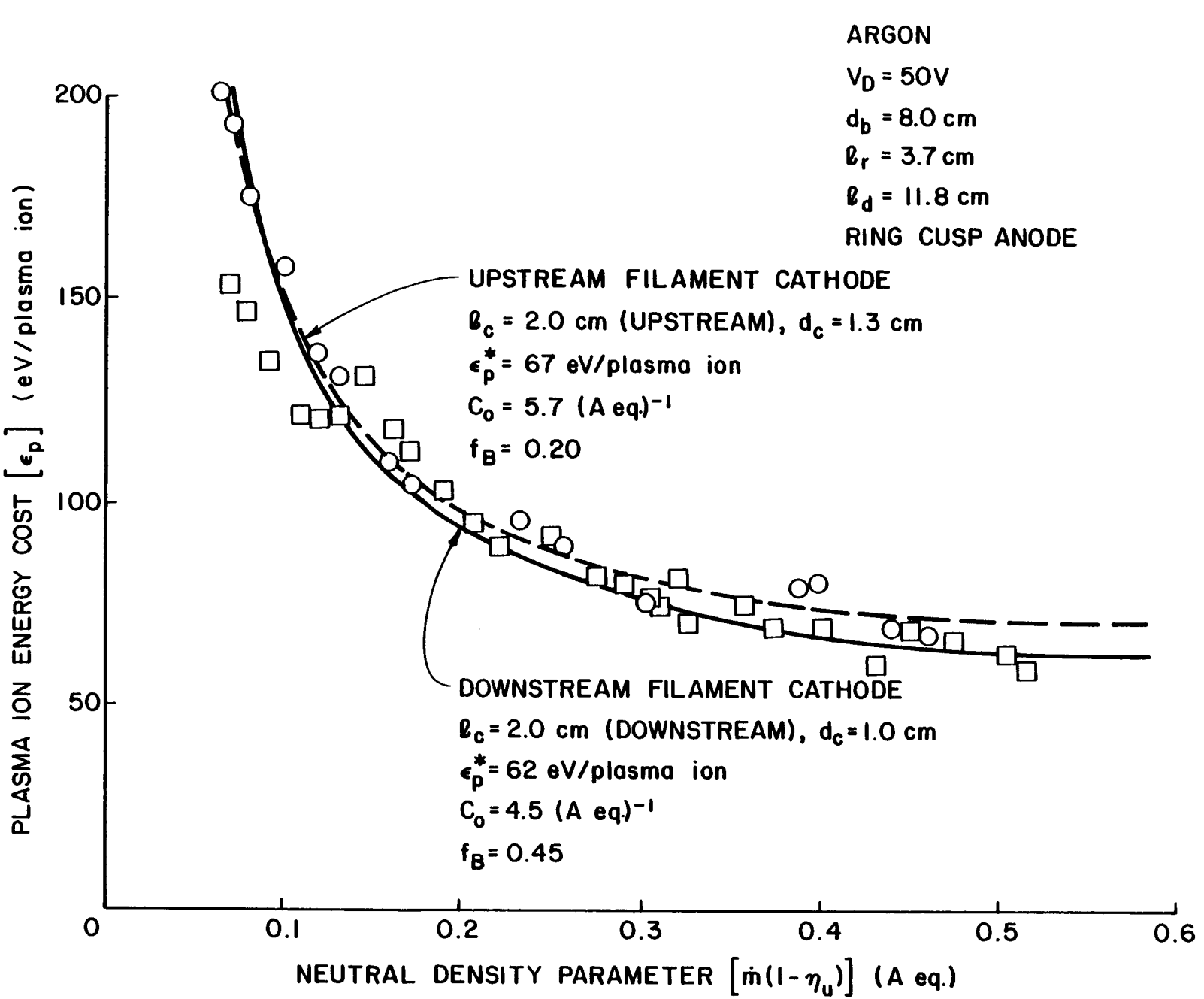

Fig. 7. Effect of Changing Cathode Location Relative to Ring Cusp

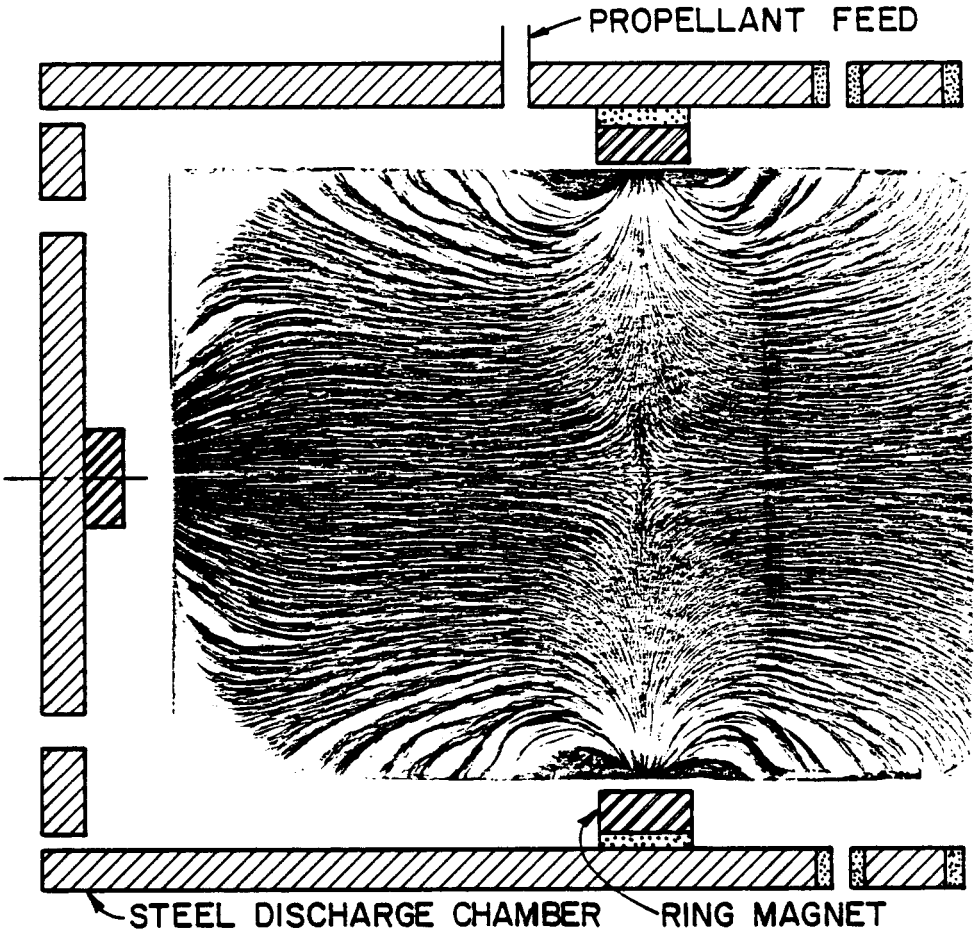

a) IRON FILINGS MAP

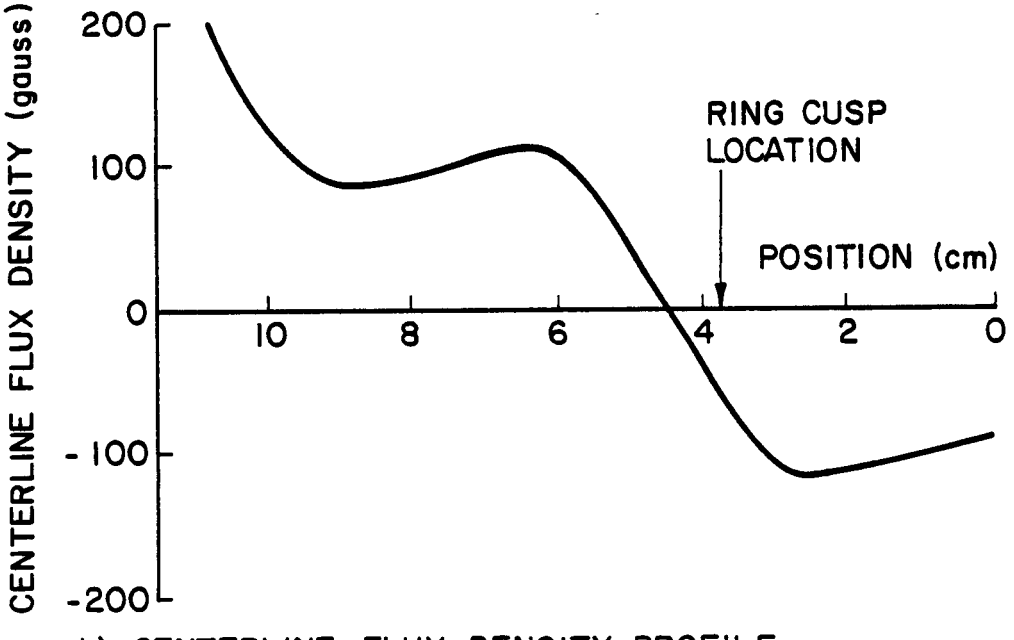

b) CENTERLINE FLUX DENSITY PROFILE

Fig. 8. Magnetic Field Environment

continuously toward the grids. This suggests primary electrons would diffuse readily toward and have direct access to the region adjacent to the grids where they should produce ions that would have a high probability of being extracted through the grids. With the filament cathode located upstream of the cusp, on the other hand, electrons from the cathode would have to pass through at least one region in which the magnitude of the magnetic flux density peaked in order to reach the region adjacent to the grids. As a result these electrons might be expected to produce ions further from the grids and this could explain in part at least why the extracted ion fraction is so much lower for the upstream filament (0.20 compared to 0.45 for the downstream filament).

The fact that the discharge could not be sustained by the downstream loop anode when the filament was upstream is also considered significant. This result suggests that electrons were generally not scattered onto field lines that enabled significant numbers of them to reach the loop anode as they diffused through the cusp region. On the other hand, significant numbers could apparently reach an anode on the cusp surface as they expanded past the axial location of the cusp toward the grids. It should also be noted that three, small, anode potential wires supporting the loop anode extended through the cusp region when the downstream filament was being used, but these wires were not present when the upstream filament was used (see Fig. 1). It may be that these wires served a keeper-like function and helped sustain the discharge to the loop anode when the downstream cathode was being used.

The fact that the values of ϵ_p^* and C_0 given in Fig. 7 are essentially unchanged within the limits of accuracy of the experiment

when the filament cathode is moved between the downstream to the upstream locations suggests that primary electron and ion losses to the ring cusp anode are probably the same whether the filament cathode is located upstream or downstream of the ring cusp.

Effects of Filament Cathode Diameter and Upstream Axial Position

While the results of Fig. 7 suggest movement of the filament cathode upstream of the cusp location is undesirable, these results are not conclusive. It may be possible to induce improvements in thruster performance with the upstream cathode by optimizing its diameter and axial location. In order to determine the optimal diameter and axial location of an upstream filament cathode a systematic study of the effects induced by changing these parameters was undertaken.

The effects of reducing the filament cathode diameter from 3.2 to 0.2 cm on plasma ion energy costs when it is located 2.0 cm upstream of the ring cusp are illustrated by the data of Fig. 9. The actual diameters tested are listed in the legend along with their corresponding symbols. These data show that reducing the major diameter of an upstream, torroidal filament cathode induces no significant changes in either the baseline plasma ion energy cost ϵ_p^* or the primary electron utilization factor C_0. This result is significant because changing the cathode diameter changes the magnetic field line surface of revolution onto which primary electrons are released into the discharge. The fact that C_0 did not change with filament cathode major diameter indicates that changing the magnetic field line onto which primary electrons are released from the filament

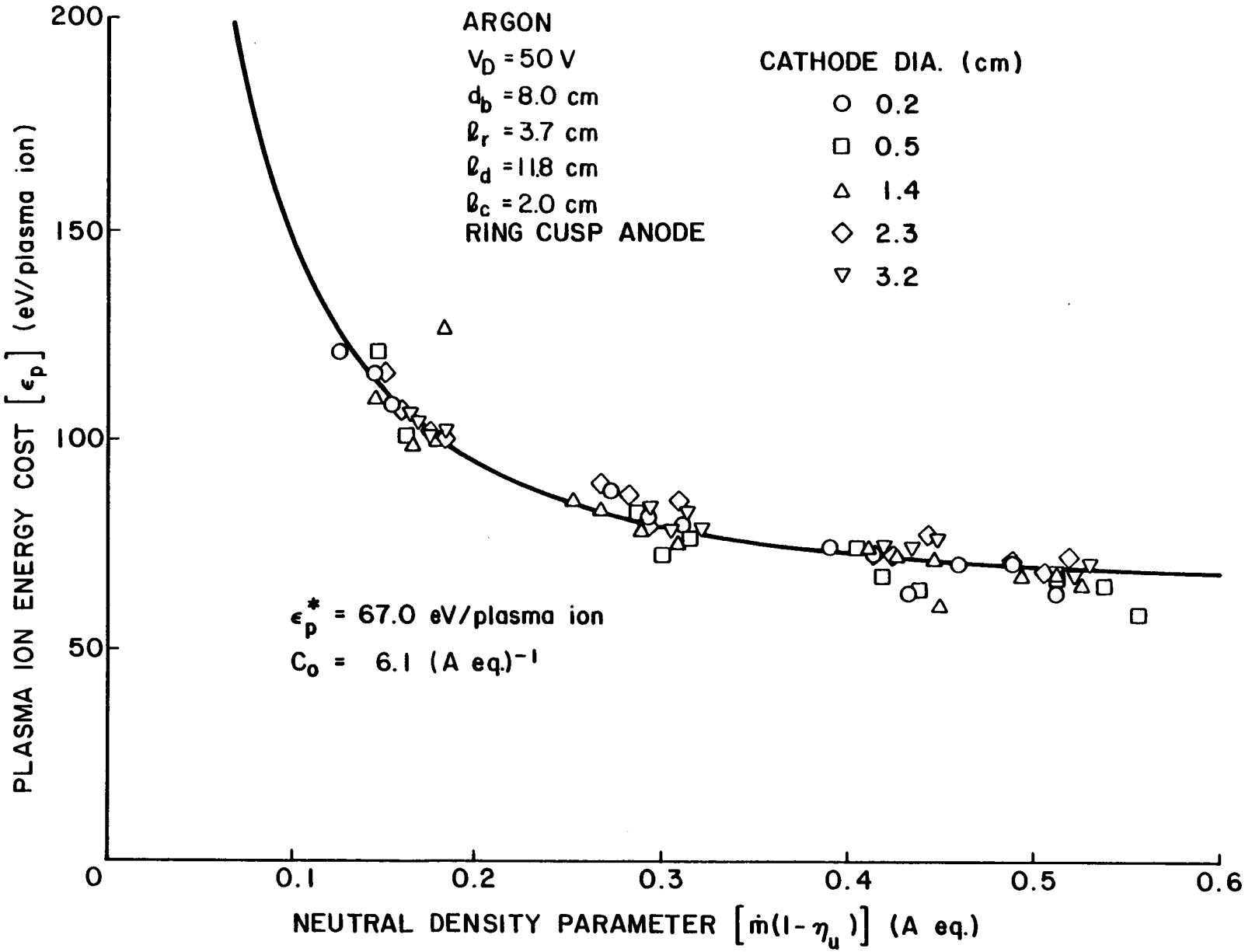

Fig. 9. Effect of Upstream Filament Cathode Diameter on Plasma Ion Energy Cost Curve

does not affect the rate at which they are collected at an anode on the ring cusp surface.

When the filament cathode was moved to a different axial location (ℓ_c = 0.7 cm) and the experiment was repeated the plasma ion energy cost data again fell along a curve characterized by common values of ϵ_P^* and C_0. The two curves generated using filament cathodes located 0.7 and 2.0 cm upstream of the ring cusp along with their associated values of ϵ_P^* and C_0 are shown in Fig. 10. The slightly lower value of C_0 associated with the ℓ_c = 0.7 cm suggests slightly poorer primary electron utilization in this case, but it is probably not significant because the change in C_0 falls within the limits of accuracy for the test.

The final parameter needed to describe the performance of a discharge chamber is the extracted ion fraction (f_B). The changes induced in this parameter by changes in the filament cathode diameter and axial location are shown in Fig. 11. These data, which were collected at the same time as those in Figs. 9 and 10, show a very dramatic effect that induces substantial changes in beam ion energy costs, namely that reducing the cathode major diameter from 3.2 to 0.2 cm causes the fraction of ions produced that are extracted into the beam to increase by about a factor of three. An additional, more modest improvement in f_B is also generally induced by moving the cathode closer to the axial location of the ring cusp but this improvement disappears when the cathode diameter is small. It is noted that each data point in Fig. 11 actually represents an extracted ion fraction averaged over the range of neutral densities investigated with a particular cathode diameter and axial location, but the standard deviation associated with each data point was small.

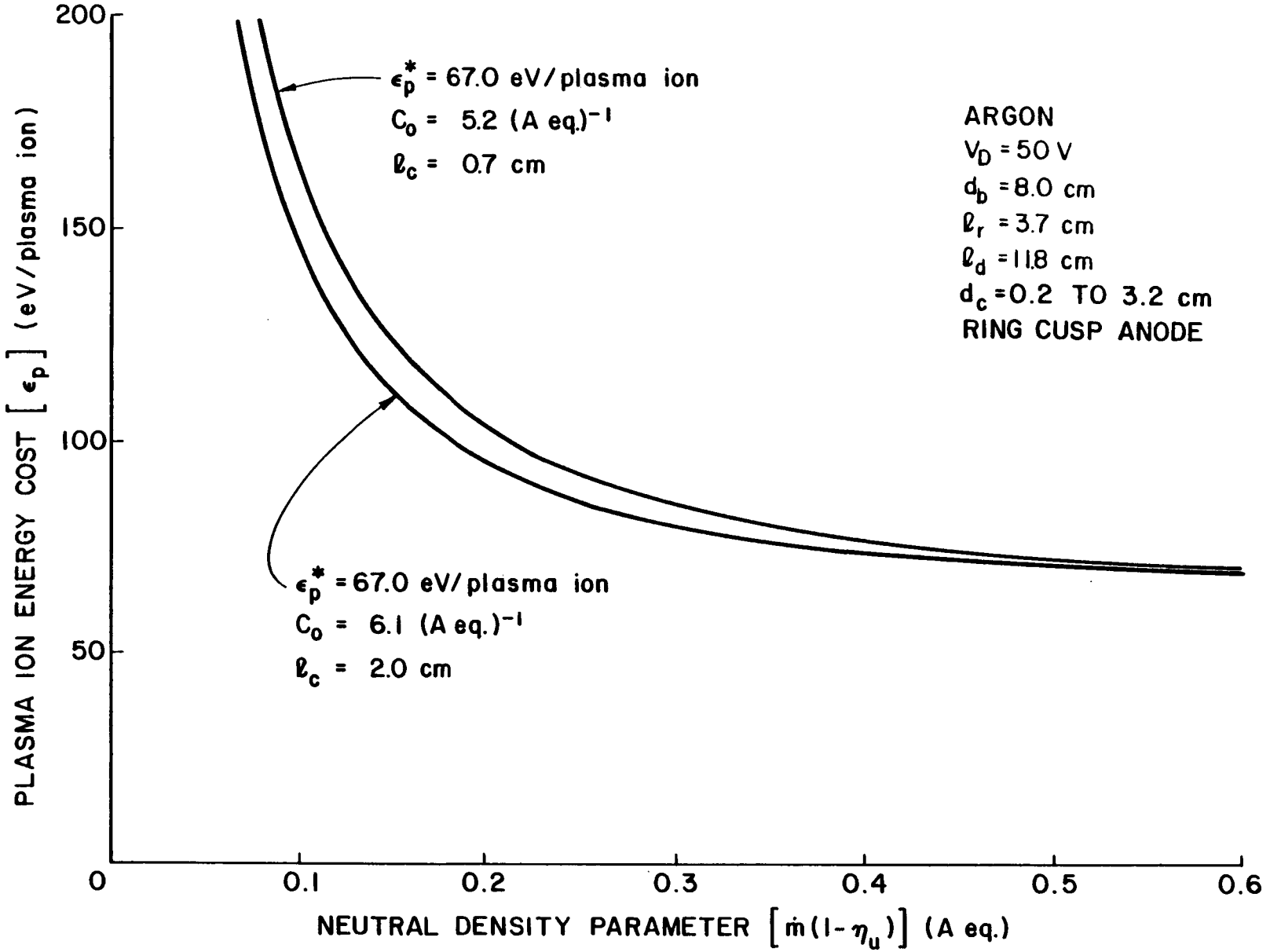

Fig. 10. Effect of Upstream Filament Cathode Axial Position on Plasma Ion Energy Cost Curve

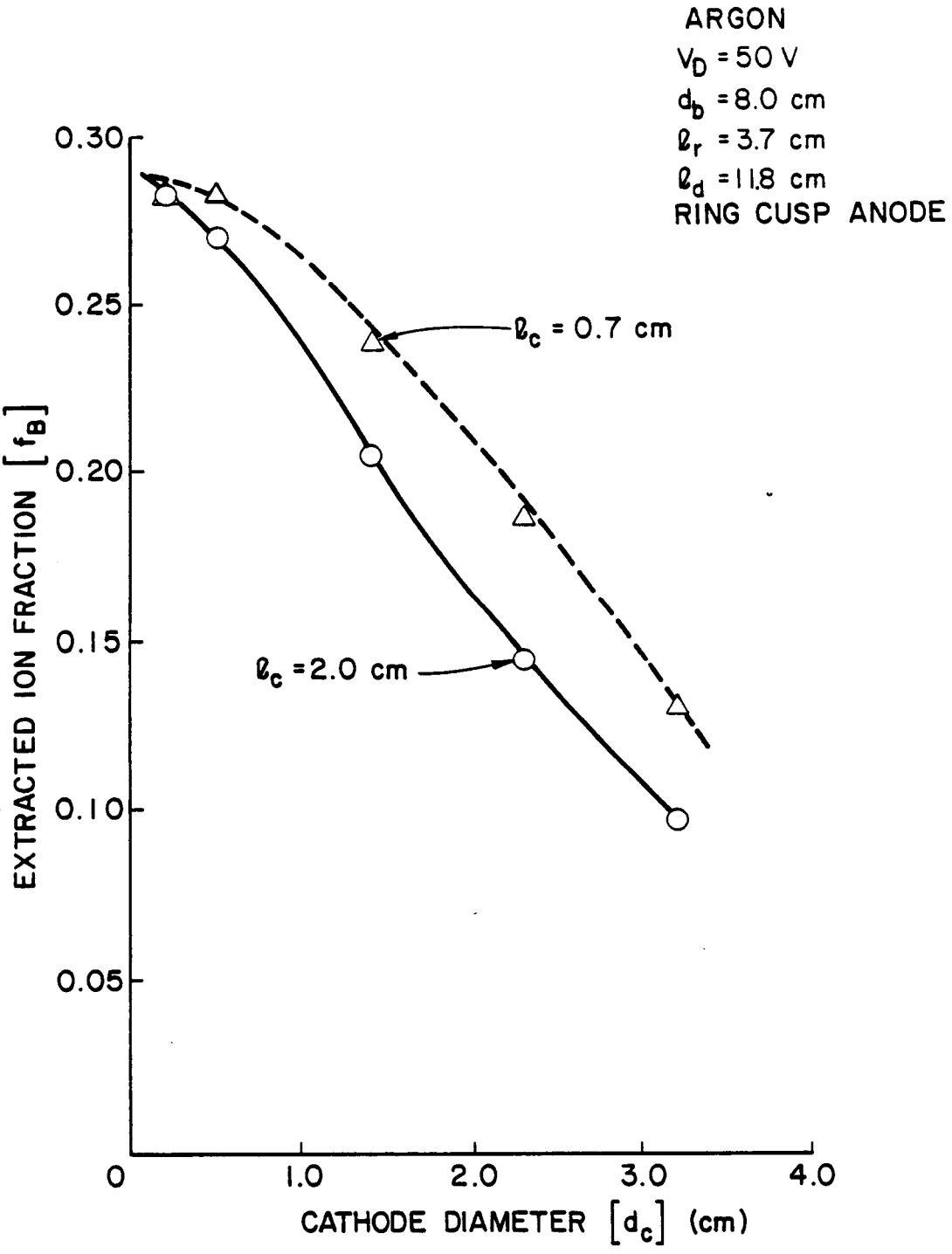

Fig. 11. Effects of Upstream Filament Cathode Diameter and Position on Extracted Ion Fraction

Because ion extraction is probably enhanced when the ions are produced closer to the grids, it is suggested that the improved ion extraction induced by reducing the filament cathode diameter and locating it closer to the cusp location probably occurs because electrons released as far downstream and as close to the thruster centerline as possible are better able to induce ionization close to the grids.

The best performance data measured using the upstream filament cathode are compared to data collected using the downstream filament cathode in Fig. 12 for the case where the ring cusp anode was being used. It is considered particularly noteworthy that the primary electron utilization and baseline plasma ion energy cost parameters associated with the small diameter filament located upstream of the ring cusp anode are essentially identical to those measured with the downstream filament cathode. Because of this agreement it can be argued that it is the use of the ring cusp anode rather than any change in cathode position that causes degradation of the primary electron utilization factor from the optimum value ($C_0 = 18.9[\text{A eq}]^{-1}$) measured using the optimized loop anode and reported in Fig. 6. When the filament was located upstream of the ring cusp it was not possible to sustain a discharge using the loop anode, so it can be stated that use of the upstream filament forced operation under poor electron utilization conditions. It could be, however, that small, anode potential wires extending through the cusp region would facilitate operation with the loop anode alone and presumably this would induce more efficient operation.

Although the size and location of the filament cathode can be adjusted to maximize the extracted ion fraction the data of Fig. 12

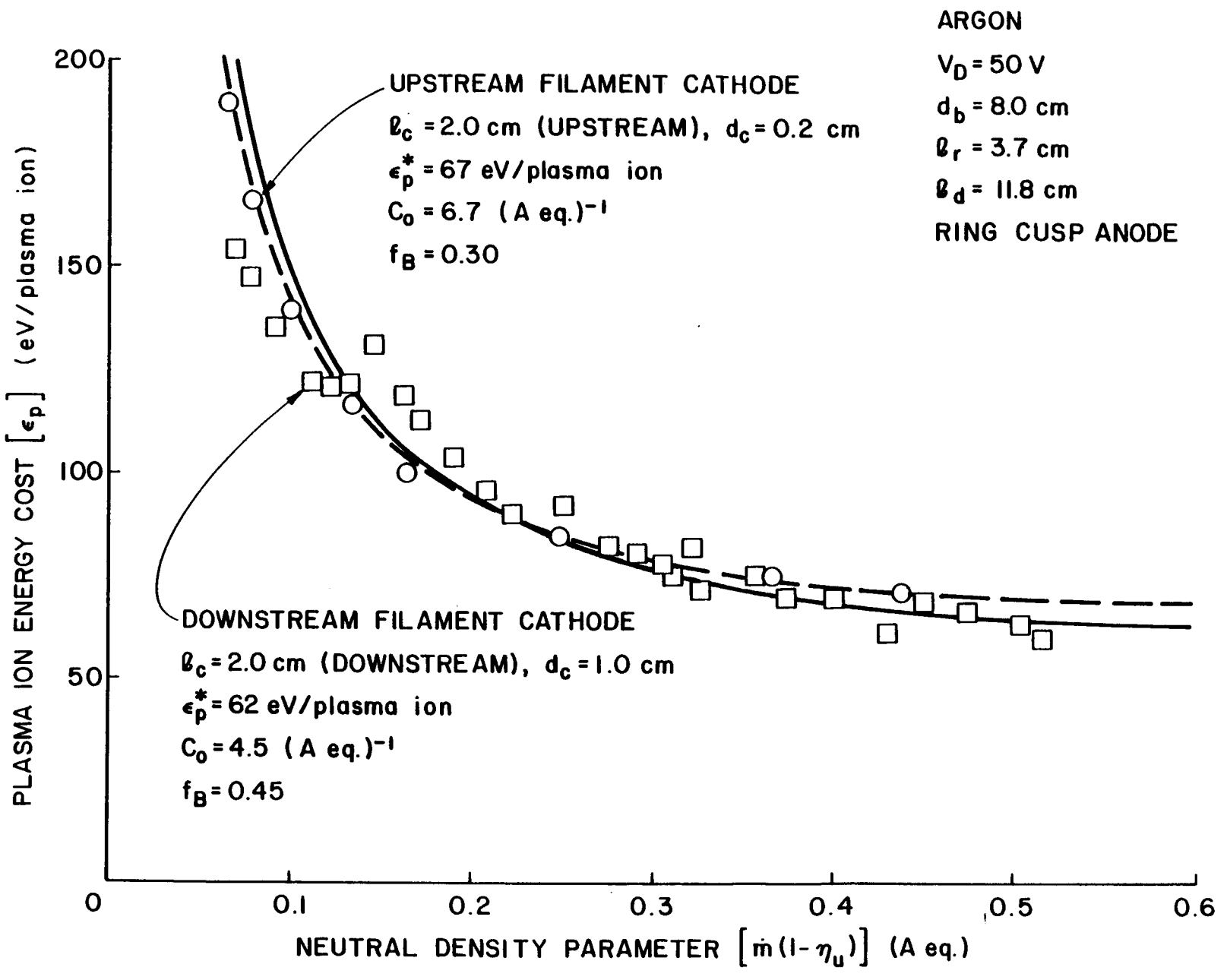

Fig. 12. Performance Comparison - Optimized Upstream and Downstream Filament Cathodes

show that even when this is done the maximum extracted ion fraction is still considerably smaller (f_B = 0.30) than the value realized with the filament downstream of the ring cusp (f_B = 0.45). Finally it is noted that the optimized upstream filament cathode is the one having the smallest diameter. Since the hollow cathode is also simply a small diameter electron source one might expect it to yield the same primary electron utilization and extracted ion fraction parameters as those associated with the upstream filament cathode (i.e. for the circular symbol/dashed line case in Fig. 12).

Although the parameters ϵ_P^*, C_0 and f_B generally describe the performance of discharge chambers adequately, they are not as familiar as the traditional beam ion energy cost/propellant utilization efficiency plot. Figure 13 shows typical examples of these more familiar performance plots measured using upstream filament cathodes having different diameters and axial locations and operating with the ring cusp anode. These curves, obtained at a flowrate of 200 mA eq (Ar) show how the performance of the discharge chamber improves as the diameter of the upstream filament cathode decreases thereby showing that a small diameter source (like a hollow cathode) should give the best performance of any upstream cathode. The fact that high propellant utilizations were not achieved in the data of Fig. 13 reflects the fact that discharge currents were limited in these tests because the ring cusp anode would overheat and short to the ring magnet surface if too much current was drawn to it.

Anode Configuration Effects

Early tests had shown that the discharge could not be sustained using the loop anode alone when the filament cathode was located

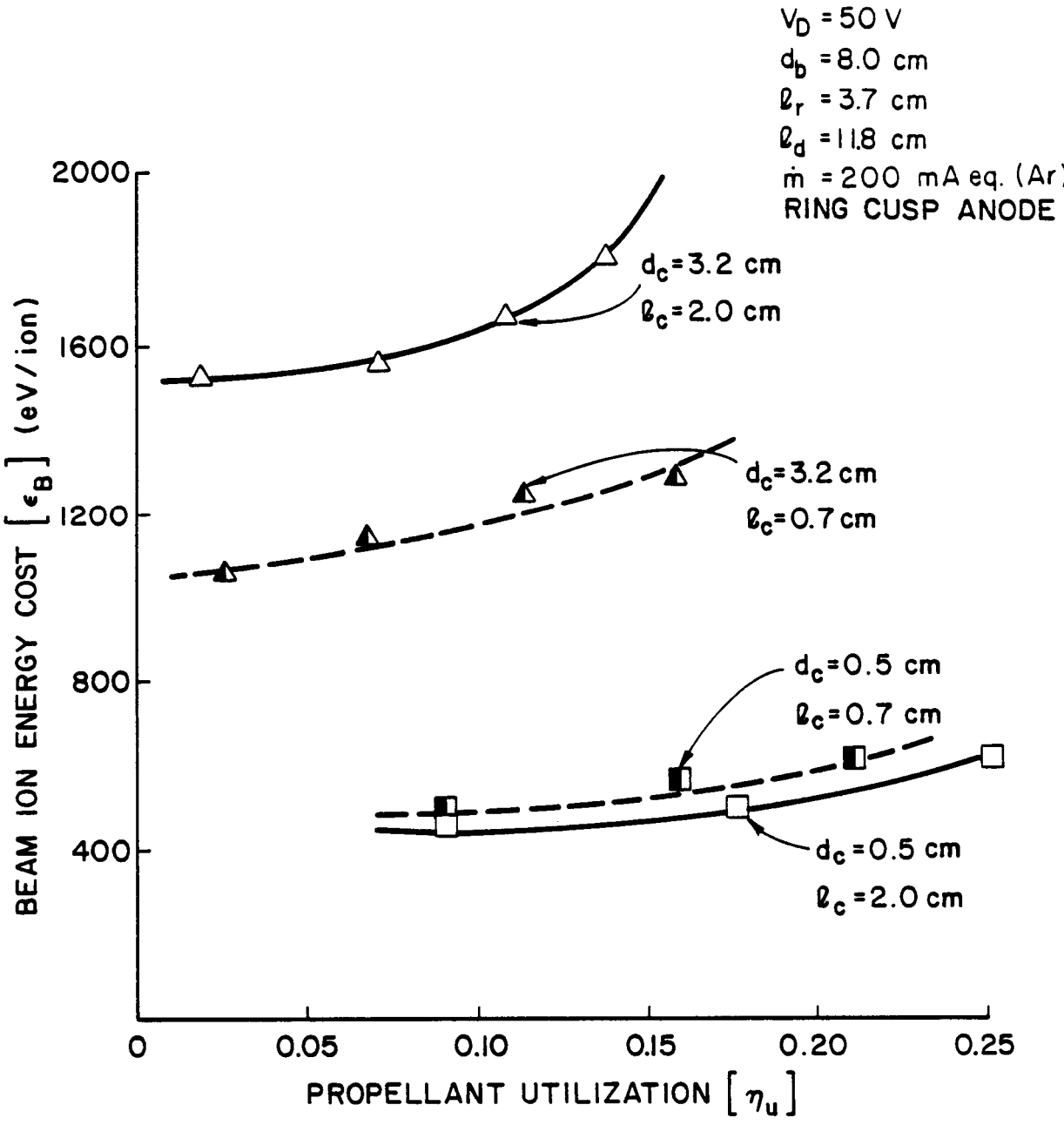

Fig. 13. Effect of Cathode Diameter and Position on Discharge Chamber Performance

upstream of the cusp plane. It was considered possible, however, that the use of both ring and downstream loop anodes might induce an improvement in discharge chamber performance. A typical comparison of discharge chamber performance parameters measured with the upstream filament cathode and various combinations of loop and ring cusp anodes are shown in Fig. 14. The curves presented in this figure are based on data collected using a 0.2 cm dia. cathode positioned 2.5 cm upstream of the ring cusp. The dimensions listed in the legend correspond to variables defined in Fig. 1. Only the least square curve fits of the data collected are shown because the data tended to lie on top of each other. The curves and associated parameters presented in Fig. 14 suggest that adding a loop anode probably does not affect discharge chamber performance substantially. All of the parameters cited by each curve agree within the limits of experimental error. This suggests that the ring cusp anode controls discharge chamber performance when it is present; this observation is consistent with results obtained by Hiatt.[1]

Hollow Cathode Located Upstream of the Ring Cusp

When the upstream filament cathode was replaced by a hollow cathode it was found that the discharge could be sustained using the downstream loop anode alone (i.e. it was no longer necessary to keep the surface of the ring cusp at anode potential in order to keep the discharge going). Plots comparing the performance changes induced in the discharge chamber equipped with an upstream hollow cathode by changing from a ring cusp anode to a downstream loop anode are shown in Fig. 15. These data were obtained at the conditions listed in the legend, but the trends they reveal were observed at other conditions

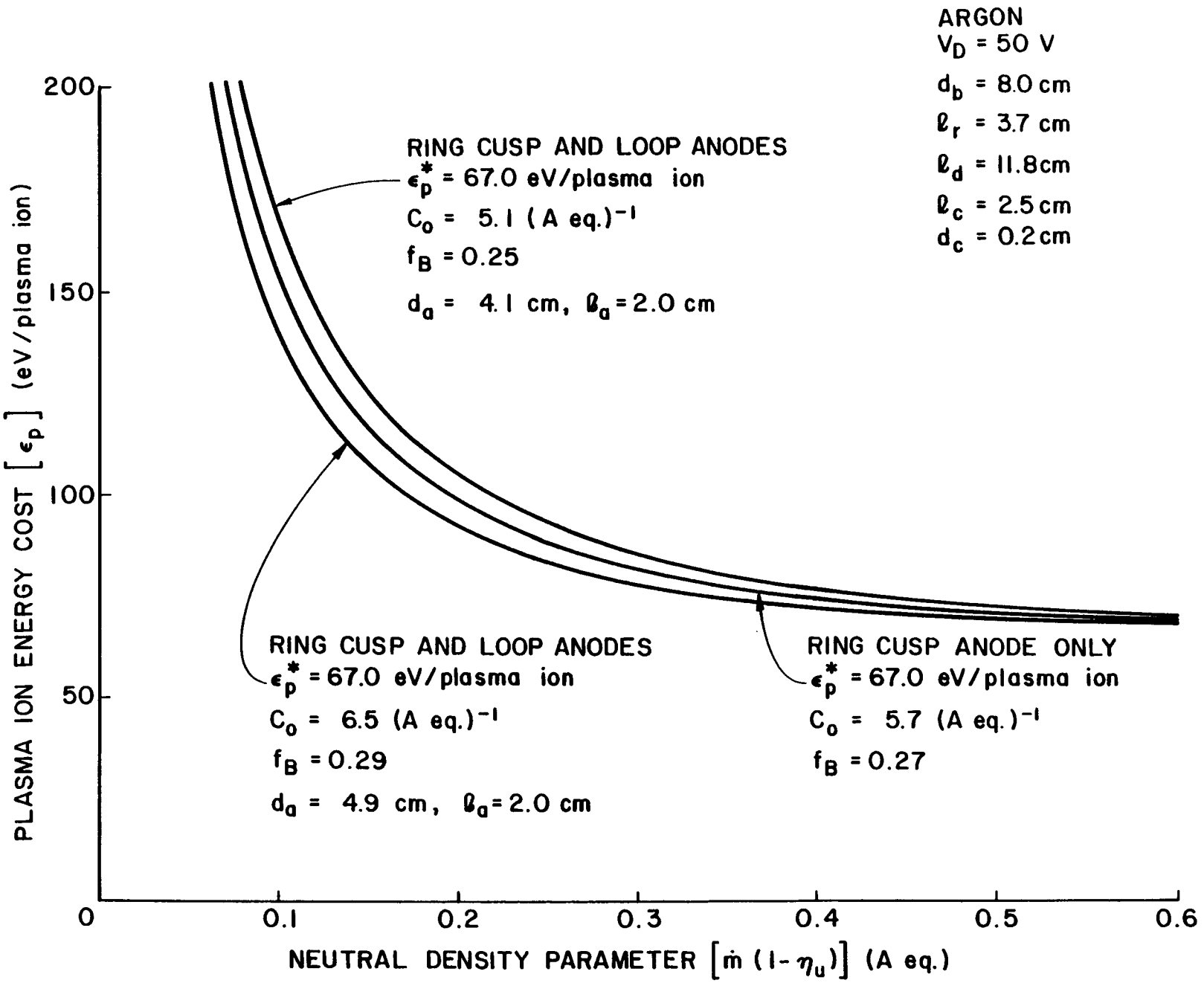

Fig. 14. Effect of Anode Configuration on Plasma Ion Energy Cost Curve-Upstream Filament Cathode

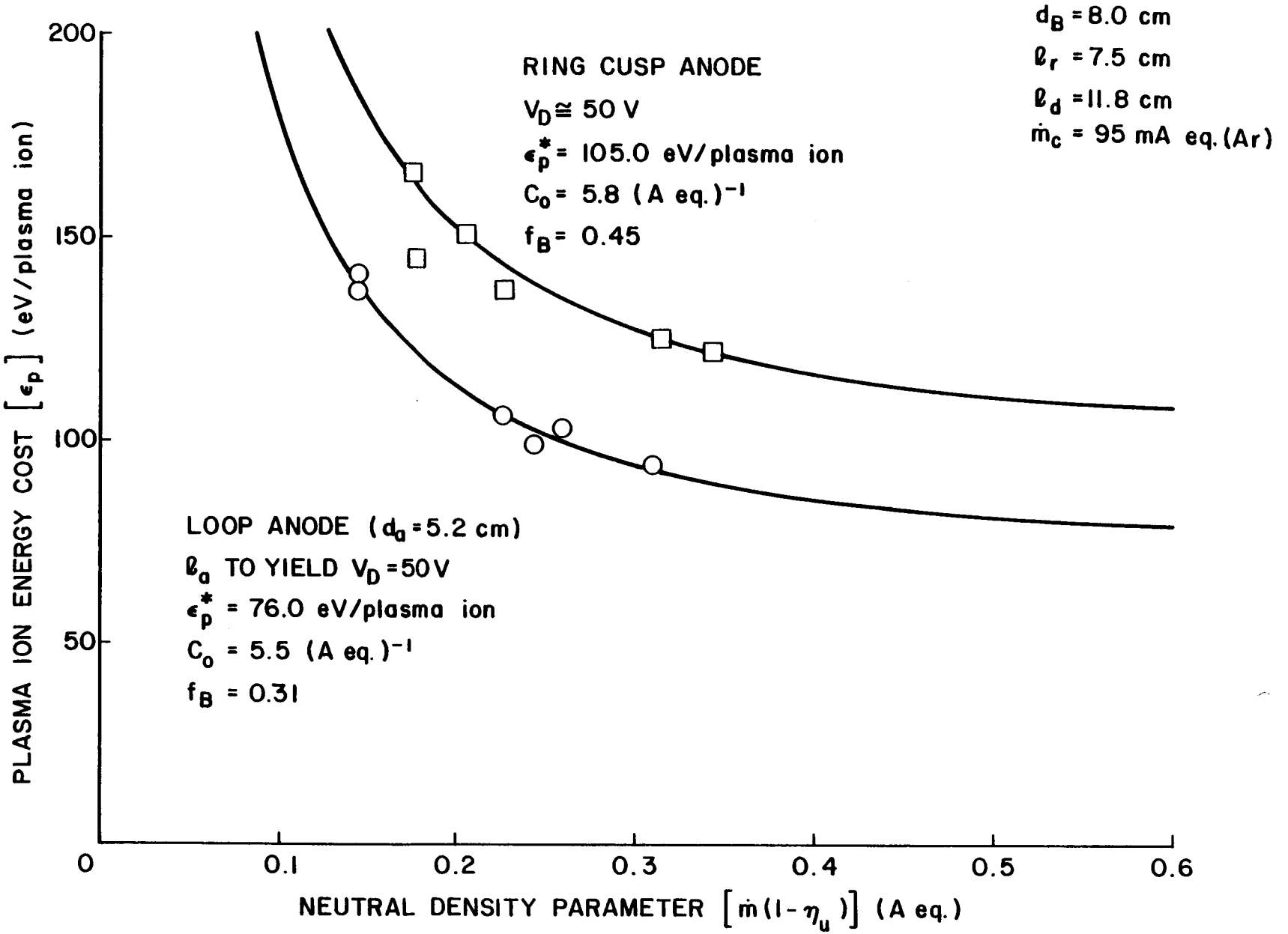

Fig. 15. Discharge Chamber Performance with upstream Hollow Cathode

and are considered typical. It should be noted that the discharge voltage could not be held constant as discharge current was varied when the cathode flowrate ($\dot{m}_c$) was fixed and the ring cusp anode was being used, but it did remain within a few volts of the desired 50 V value in these tests. On the other hand, the discharge voltage could be held constant by adjusting the axial position of the loop anode when it was being used.

The data of Fig. 15 show primary electron confinement is similar for the two anode configurations (similar values of C_0). A comparison of baseline plasma ion energy costs shows this parameter is ~50% higher for the ring cusp anode configuration. This indicates ions are being lost to either the ring cusp anode or the hollow cathode at a much higher rate when the ring cusp anode is being used. Notice, however, that the extracted ion fraction (f_B) is also ~50% higher when the ring cusp anode is being used. Taken together these results suggest a fact that was confirmed by a detailed balance of ion currents going to the discharge chamber surfaces; that the fraction of the total ion production current going to the surface of the ring cusp was the same in both cases. When the ring cusp anode was being used this loss was reflected as an increase in the baseline plasma ion energy cost because this ion current could not be measured. When the loop anode was being used it was measured, however, and it was therefore reflected as a decrease in the extracted ion fraction. This result was also reflected in the fact that the energy cost of a beam ion at a given beam current was the same for both anode configurations.

Once it had been determined that a discharge could be sustained between a hollow cathode and the downstream loop anode all tests were

conducted using this anode rather than the ring cusp one. This was done for two reasons: 1) precise discharge voltage control could be maintained at any propellant flow condition while the thruster was operating by adjusting the axial position of the loop anode, and 2) the likelihood of achieving good discharge chamber performance was, based on Hiatt's observations, considered to be greater when the loop anode was being used.

It is interesting to speculate about why operation could be sustained between a loop anode and an upstream hollow cathode when it could not be sustained between an upstream filament cathode, having an electron emission zone similar to that of the hollow cathode orifice. Why do these two electron sources behave differently? The answer is probably related to the fact that there were three anode potential wires that extended through the cusp region when the hollow cathode was being tested (Fig. 3) that were not present during the upstream filament tests (Fig. 1). It is also possible that more ions are produced adjacent to the hollow cathode orifice than are produced adjacent to the filament surface. It seems reasonable to suggest that higher ion (and therefore plasma) and neutral atom densities would facilitate electron diffusion across magnetic field lines thereby increasing the effective size of the primary electron source beyond that of the cathode orifice. Tests conducted using filament cathodes of various diameters did not, however, suggest that larger diameter filament cathodes could sustain a discharge to the loop anode.

Effects of Magnetic Field Changes

The fact that baseline plasma ion energy costs increased when the hollow cathode was substituted for the small diameter filament cathode

located upstream of the ring cusp can be seen by comparing typical data like those in Figs. 12 and 15. This result was expected because it was recognized that some discharge power would be required to sustain the hollow cathode discharge and that ion losses from the discharge plasma to the hollow cathode surface would probably be greater than those to the filament cathode. This latter point was also postulated on the basis that ions produced adjacent to the hollow cathode should cause a high density plasma plume, extending from the cathode orifice, to form. It is suggested that the surface of this plume could be relatively large and that substantial numbers of ions could be drawn across it from the discharge plasma to an eventual fate of recombination on the hollow cathode surface.

It was also postulated that the strength of the magnetic field environment at the hollow cathode and in the region between it and the prime ion production region adjacent to the grids would influence where ions were being produced and the difficulty they would encounter in reaching the grids. With this in mind, a study of the effects of changes in the magnetic flux density in the region along the thruster centerline from the hollow cathode to the grids was conducted. Specifically, the effects of changing the position of the maximum centerline magnetic flux density relative to the position of the hollow cathode orifice and changing the magnitudes of the magnetic flux densities in the discharge chamber were investigated.

Tests conducted with filament cathodes generally utilized a ring magnet located 3.7 to 4.5 cm upstream of the screen grid and a backplate magnet to produce the desired magnetic field. Attempts to use a hollow cathode in this magnetic field environment, however, resulted in high keeper voltages (as great as 50 V) and high

accelerator grid impingement currents at modest beam currents (< 100 mA). This high impingement current is taken as an indication that the discharge plasma was confined to a region that had a small diameter at the grids and that this caused the perveance limit of the the grids to be reached near their centerline at modest beam current levels. The high keeper voltage problem was relieved by removing the backplate magnet and the high impingement current problem was relieved by moving the ring magnet upstream of the locations used in conducting the filament cathode tests. Figure 16a shows axial magnetic flux density profiles measured along the thruster centerline when the ring magnet was positioned at the locations where most hollow cathode tests were conducted (6.5 and 7.5 cm upstream of the grids). Also shown in Fig. 16a is the cathode orifice plate which was located slightly upstream of the peak flux density point when the magnet ring was 6.5 cm upstream of the grids and downstream of this peak when the magnet was at the 7.5 cm position. Figure 16b shows how changing from the generally used large ring cusp magnet elements (1.9 x 1.3 x 0.5 cm) to small ones (1.2 x 0.6 x 0.5 cm) reduced the centerline magnetic flux density profiles.

When the ring magnet was moved from 6.5 to 7.5 cm upstream of the grids the changes in discharge chamber performance shown by the data in Fig. 17 were measured. For these tests a keeper was used at a current (J_k) of 0.3 A and this produced a keeper voltage (V_k) of about 25 V and the plasma ion energy cost data given in Fig. 17 reflect the inclusion of this power. Although the performance parameters are not changed substantially by this change in ring magnet position, the baseline plasma ion energy cost does decrease somewhat as the magnet is moved so the cathode orifice is downstream of the maximum flux

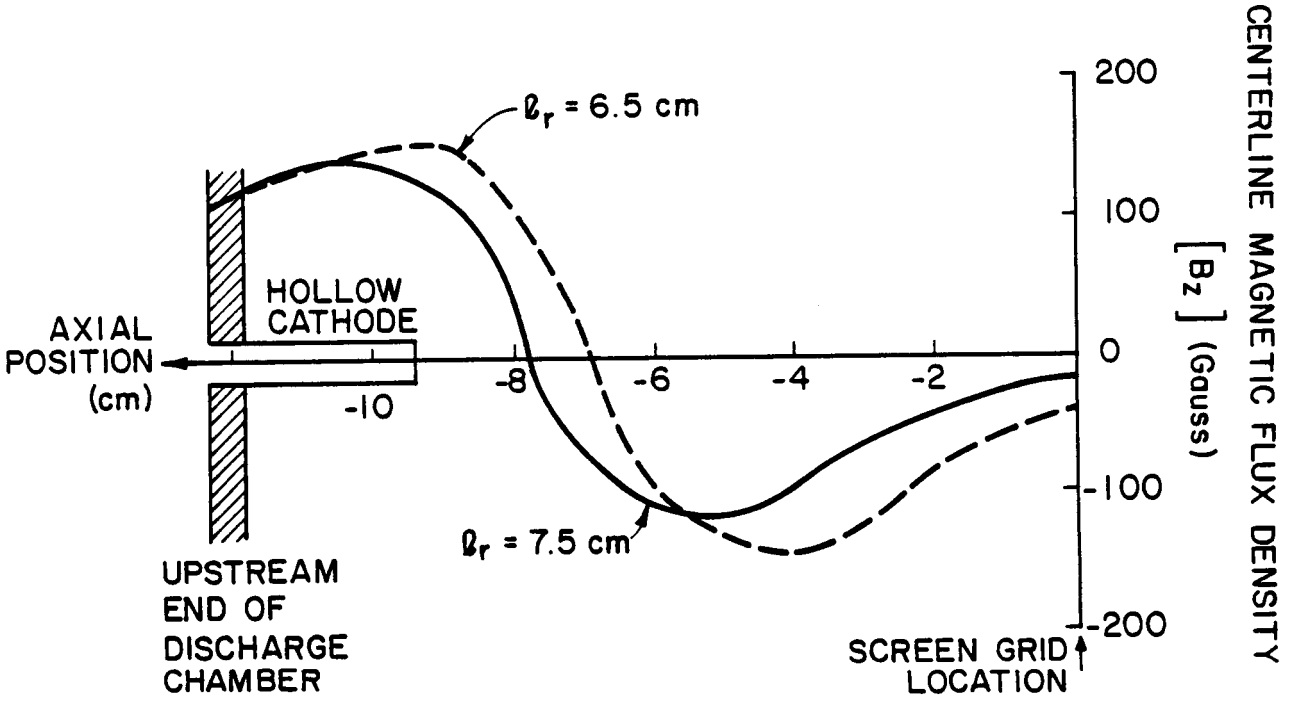

a) EFFECT OF RING CUSP LOCATION

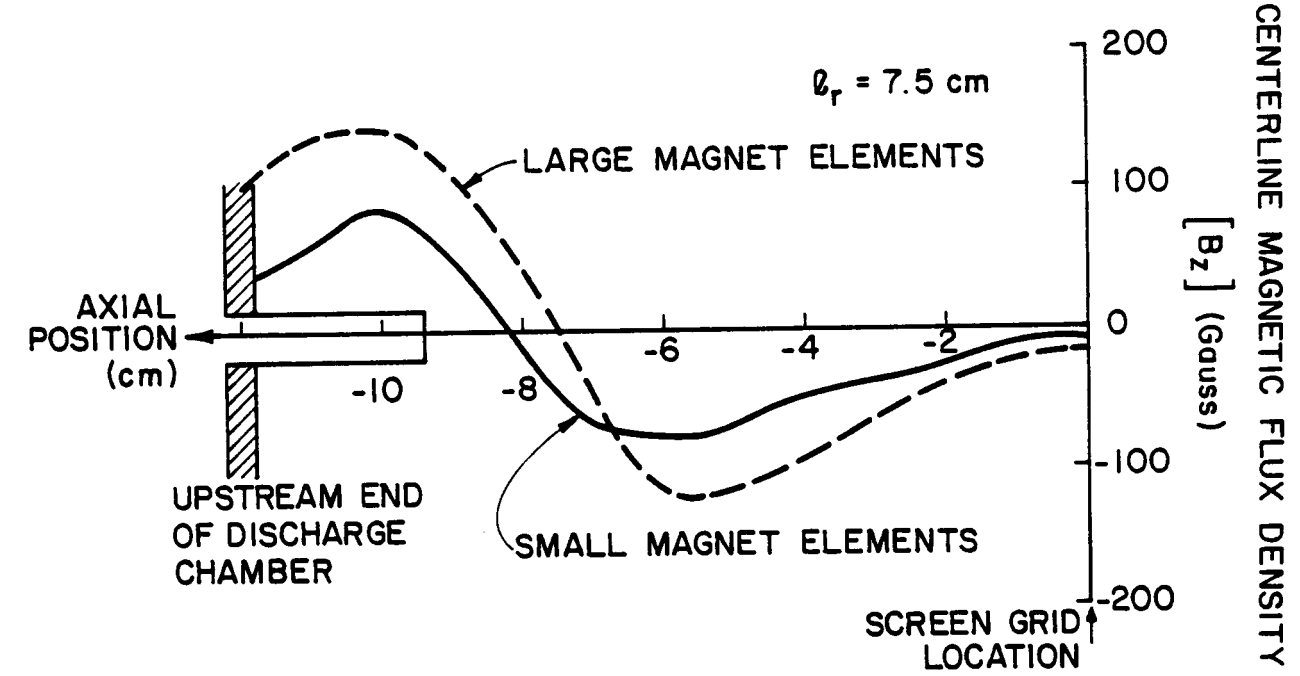

b) EFFECT OF MAGNET ELEMENT SIZE

Fig. 16. Magnetic Flux Density Profiles

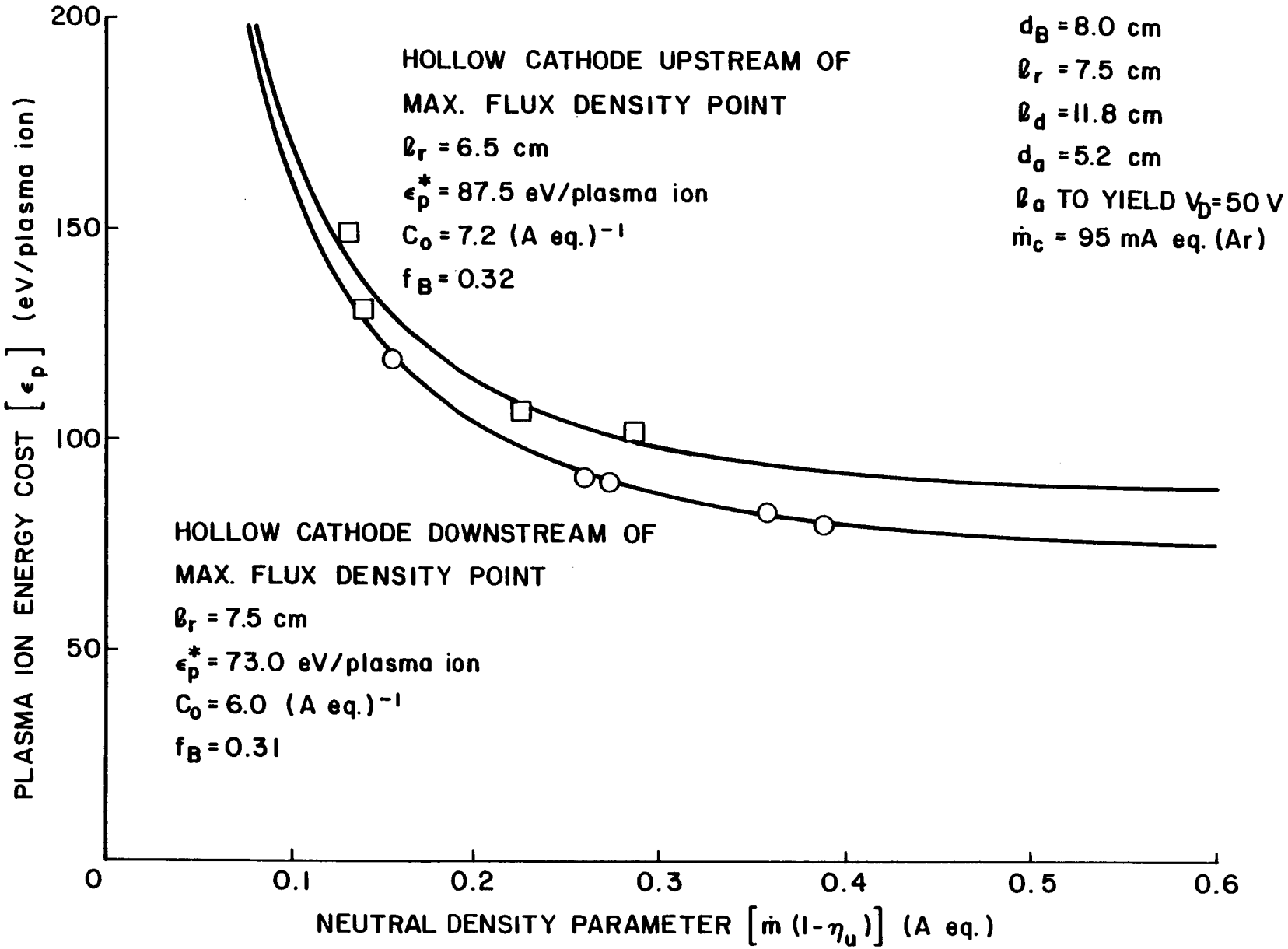

Fig. 17. Effect of Position of Hollow Cathode Relative to Maximum Magnetic Flux Density Point

density point. This suggests that ions produced near the cathode may find it increasingly difficult to escape recombination on the cathode surface as the number of regions of high flux density (i.e. regions of converging flux lines) they must pass through to reach the grids increases. One would also expect these ions would find it increasingly difficult to reach the grids as the magnitudes of the magnetic flux density peaks increased.

When the small magnets were used in place of the large ones and the peak magnetic flux densities dropped to the levels indicated by the solid line in Fig. 16b the performance changes shown in Fig. 18 were observed. Again this change did not cause dramatic changes in the discharge chamber performance parameters but both the decrease in baseline plasma ion energy cost and the increase in extracted ion fraction that seem to occur when the small magnets are used suggest ions may be able to escape from the region near the hollow cathode more readily when flux densities are lowered. The smaller value of the primary electron utilization factor associated with the small magnets suggests these electrons are also able to migrate to the loop anode more easily in the lower magnetic flux density environment.

Effects of Cathode Flowrate

It has already been suggested that a hollow cathode electron source behaves differently than a filament source even when both sources are essentially the same size because of the availability of larger numbers of ions adjacent to the hollow cathode. It could also be that a high neutral density adjacent to an electron source (as in the hollow cathode) would result in inordinate numbers of electron collisions during the acceleration process that resulted in excitation

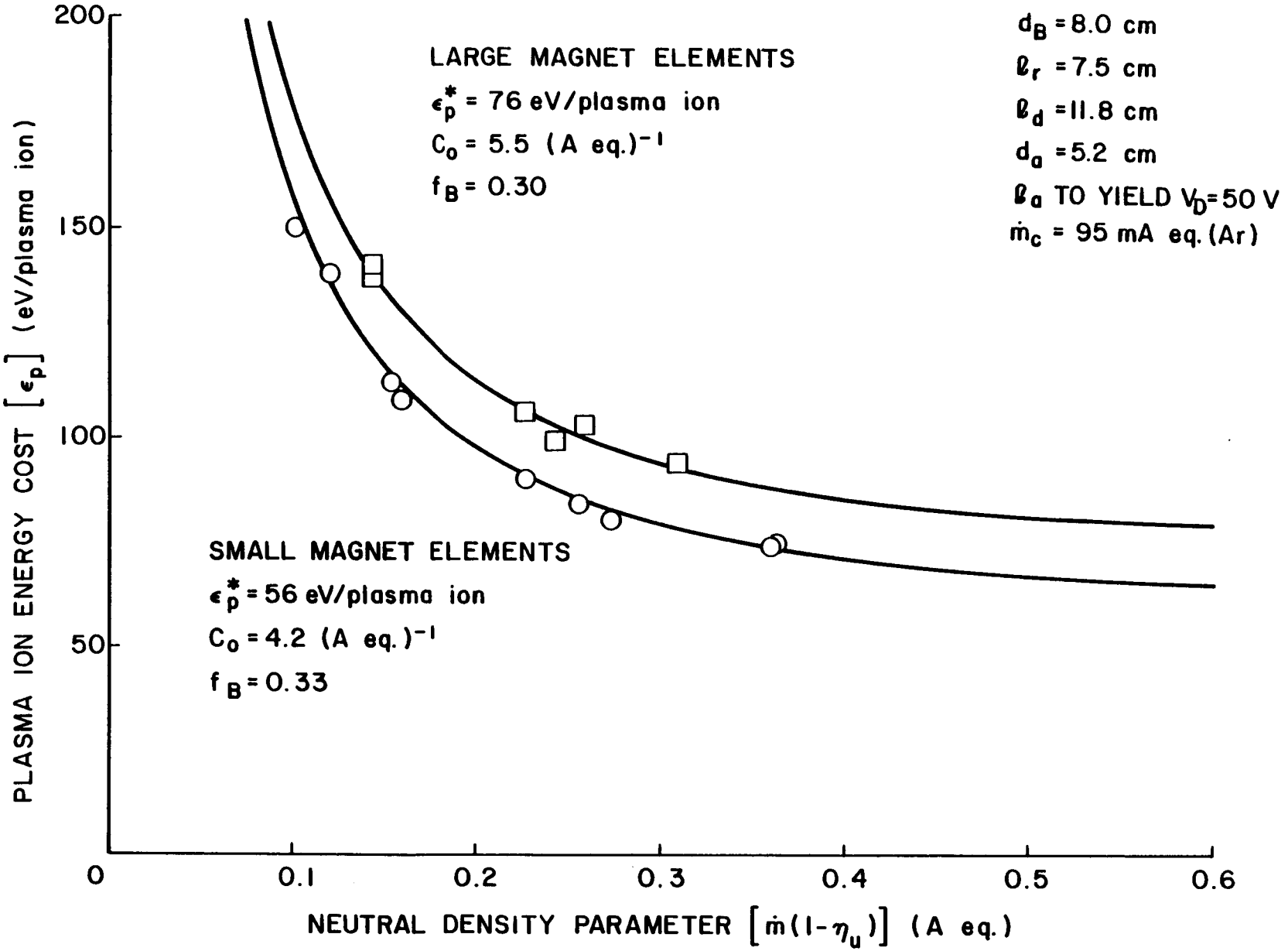

Fig. 18. Effect of Magnetic Flux Density on Plasma Ion Energy Cost Curve

rather than ionization and that this would reduce the ionization efficiency of the electrons. One could argue based on these postulated effects that an increase in hollow cathode flowrate could alter discharge chamber performance because it would increase the ion production rate near the cathode or reduce ion production throughout the rest of the discharge chamber. This effect was studied and typical results showing what occurred when the hollow cathode flowrate was reduced from 143 mA eq to 95 mA eq are shown in Fig. 19. The small reduction in baseline plasma ion energy cost and the more substantial increase in extracted ion fraction are consistent with the model of ion production adjacent to hollow cathodes that has been postulated. The changes in these parameters are, however, within the limits of experimental error so it was necessary to change the cathode flowrates over a larger range in order to determine if the trend was significant. It would be desirable to reduce cathode flowrates below 95 mA eq. to conduct the study because this would be expected to change the discharge parameters favorably. Unfortunately, the cathode flowrate could not be reduced below this value or the cathode would go out. The effects of increasing cathode flowrate on the extracted ion fraction and the baseline plasma ion energy cost are shown in Fig. 20. These curves show that the trends toward decreased baseline plasma ion energy costs and increased extracted ion fractions with decreases in cathode flowrate suggested by the data of Fig. 19 are observed over a wide flowrate range. These results seem to support the postulate that increases in cathode flowrate result in increased ion production near the hollow cathode and that ions created adjacent to the cathode tend to be lost to the cathode (increasing ϵ_p^*) and to other discharge

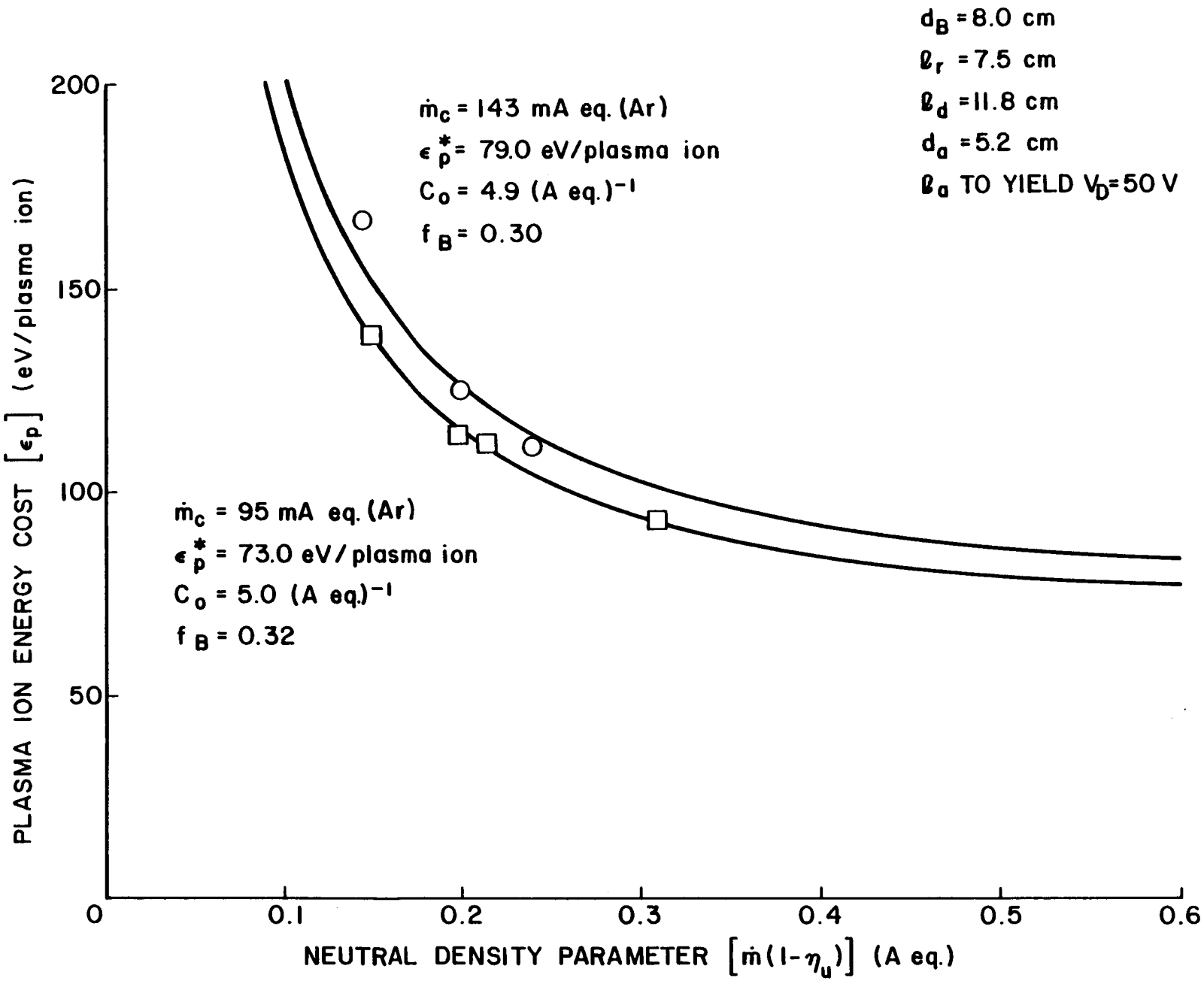

Fig. 19. Effect of Cathode Flowrate on Plasma Ion Energy Cost Curve

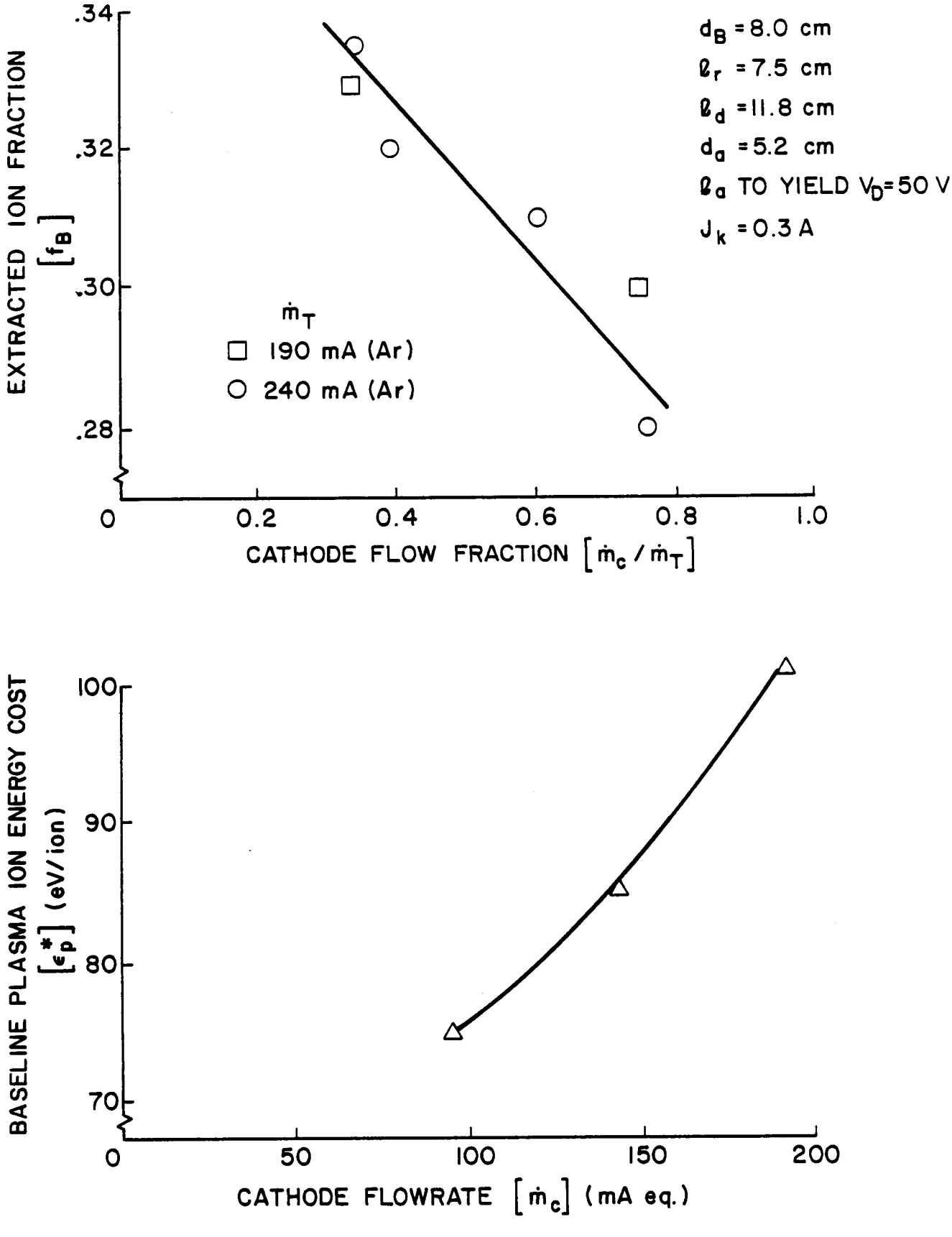

Fig. 20. Effect of Cathode Flowrate on Discharge Chamber Performance Parameters

chamber surfaces (decreasing f_B) rather than being extracted into the beam.

The Influence of the Keeper on Discharge Chamber Performance

In typical space applications of ion thrusters it is undesirable to use a keeper because it adds to system complexity. In order to determine the effect a keeper typically has on discharge chamber performance a test was conducted in which a discharge chamber was operated first with the keeper collecting a current (J_k = 0.3 A) and then with it floating (J_k = 0). The results of this test are shown in Fig. 21 and they indicate the only discharge chamber performance parameter affected significantly by changes in keeper power is the baseline plasma ion energy cost. For the particular operating conditions investigated here use of the keeper caused this parameter to increase by about 17 eV/plasma ion.

CONCLUSIONS

The best discharge chamber performance is realized in the 8 cm ring cusp discharge chamber being used in these tests when a filament cathode located downstream of the magnetic ring cusp is used in conjunction with a loop anode. Test results obtained confirm results obtained by Hiatt which showed that peak performance was achieved when the anode contacted the surface of revolution of the magnetic field line that intersected the outermost ring of holes in the screen grid. Results also confirmed Hiatt's postulate that the cathode should be emitting primary electrons onto the surface of revolution of a magnetic field line that was separated sufficiently from the virtual anode surface so the discharge was on the verge of going out.

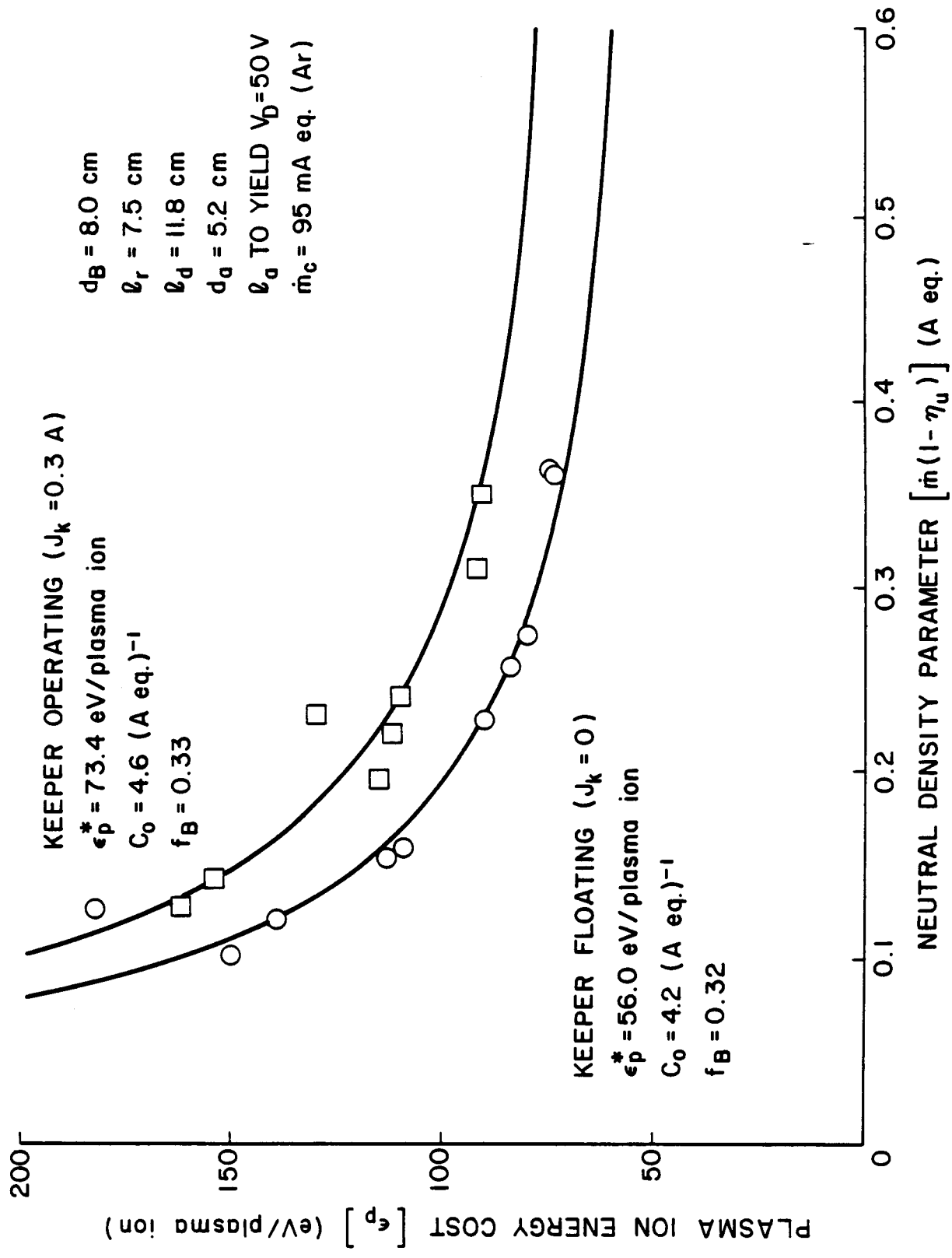

Fig. 21. Effect of Keeper Operation on Plasma Ion Energy Cost Curve

When a filament cathode is moved upstream of the ring cusp magnet test results indicated a discharge to a loop anode could not be sustained so an anode located on the ring cusp surface is required with an upstream filament. Use of this anode causes discharge chamber losses to increase because primary electrons are lost to this anode too readily. The rate of primary electron loss to this anode is the same whether the filament cathode is located upstream or downstream of the ring cusp. When a hollow cathode is used in place of the upstream filament cathode a discharge can be sustained to a downstream loop anode but the rate at which primary electrons are lost to this anode are comparable to those that occur when the ring cusp anode is used with either upstream filament or hollow cathodes. When either filament or hollow cathodes are used as electron sources upstream of the ring cusp magnet the discharge chamber performance is also degraded. It is suggested that this may occur because a substantial fraction of the ions produced upstream of the cusp are lost to the cusp surface as they attempt to diffuse past it toward the grids. The filament cathode performs best when it has a small diameter and is located close to the axial location of the ring cusp because ion losses to the cusp are minimized. The best performance achieved with an upstream hollow cathode is essentially identical to that achieved with the best upstream filament cathode configuration. Hollow cathode discharge chamber performance is degraded by increasing either cathode flow or keeper power because these changes cause the baseline plasma ion energy costs to increase. Increases in cathode flowrate also cause detrimental decreases in the extracted ion fraction. Alterations in the magnetic field strength and configuration in the discharge chamber equipped with an upstream hollow cathode appear to

influence all of the discharge chamber performance parameters. It is therefore probable that hollow cathode discharge chamber performance can be enhanced through proper magnetic field design but that design has not been identified at this point in the study.

MODIFIED SERT II ION THRUSTER OPERATION ON XENON

INTRODUCTION

A scientific exploration mission to the moon, which would employ two Space Electric Rocket Test II (SERT II) type ion thrusters that would be deployed into Earth orbit in a Get-Away Special (GAS) canister, has been proposed.[3] In order to accomplish this mission, however, it is necessary that the thrusters be modified so they can be operated on xenon propellant and so they can use the high perveance, dished grids that have been developed since the original SERT II design[4,5] was frozen in the late 1960's. In addition, a throttling scheme has been proposed that would allow the power to the thrusters to be reduced as the solar array output degrades during the mission without introducing any more control system complexity and hardware than is absolutely necessary into the system design.

The control scheme that has been proposed is illustrated by the beam current and grid voltage profiles shown in Fig. 22. As these plots suggest, it is anticipated that the thruster input power will decay from 1850 watts, which will be produced by the solar array at Beginning of Life (BOL), to a value that could be as low as ~600 watts at the end of the mission. The scheme illustrated in Fig. 22 involves reducing the screen grid (beam) voltage to reduce beam power (and specific impulse and thrust) while holding the ion beam current as constant as possible. This would be accomplished by increasing the accelerator grid voltage as the screen grid voltage was decreased in the manner shown in the figure to keep the total accelerating voltage constant. This process would be continued until the net-to-total accelerating voltage ratio (R) decreased to the point where it could

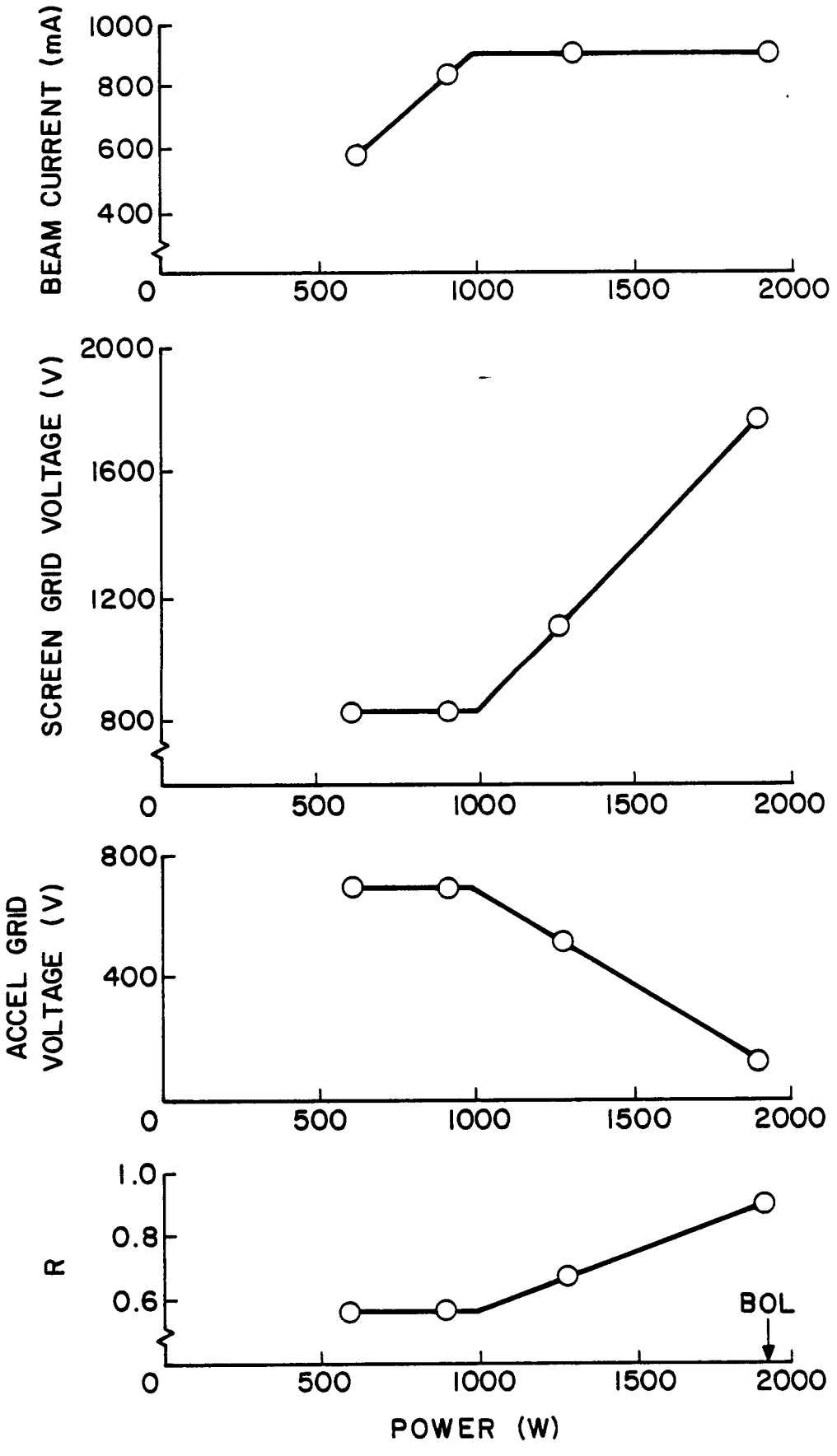

Fig. 22. Modified SERT II Throttling Strategy

begin to induce excessive ion beamlet divergence. As the lowest plot of Fig. 22 indicates, a value of 0.55 is the value of this limit being used at the present time. At thruster powers below about 1000 w, where this limit is encountered, it would be necessary to reduce the beam current by reducing discharge chamber power to accommodate further reductions in solar array output power. In this operating regime (R = 0.55) the grid voltages would be held constant at the values indicated in the figure. The propellant flowrate and distribution within the discharge chamber would, however, be held constant over the entire range of thruster powers identified in Fig. 22.

In order to determine whether the SERT II thruster could be first modified and then operated efficiently at the beam current and voltage conditions suggested in Fig. 22, a SERT II thruster was modified and a test was conducted to measure its performance on xenon propellant over the proposed operating range.

APPARATUS AND PROCEDURES

These tests, which must be considered preliminary demonstrations of thruster capability, were conducted in a 1.2 m dia. by 5 m long vacuum chamber, which was being held at a pressure in the high 10^{-6} Torr range. They were carried out using a conventional SERT II thruster[4,5] that had been modified in the following ways:

1. The standard 0.32 cm dia. discharge chamber hollow cathode was replaced with a 0.64 cm dia. hollow cathode. The orifice plate of this cathode had a 0.74 mm dia. orifice in it and the cathode body contained a 2.5 cm long by 0.38 cm inside diameter, hollow, sintered tungsten, barium aluminate-impregnated insert. Care was taken to mount the cathode so propellant leakage from the discharge chamber

through seams between the cathode and the chamber body would be negligible compared to typical neutral propellant losses through the grids.

2. Two separate propellant feed systems were installed so xenon could be supplied through the hollow cathode and the main flow plenum and so these flows could be controlled and measured independently.

3. The hollow cathode neutralizer was replaced by a temporary, refractory metal wire neutralizer that passed through the beam along a diameter about 3 cm downstream of the grids. This change was made because a suitable hollow cathode neutralizer and associated flow system were not available for the test.

4. The low perveance, flat SERT II ion extraction grids were replaced with high perveance, downstream-dished grids that had 1.9 mm dia. screen holes and 1.3 mm dia. accel holes on 2.2 mm centers (68% open area screen and 30% open area accel). The grid separation, which was 0.6 mm when the grids were cold, was maintained by isomica spacers that were clamped between the grids using paper clips. The grid set was made from 30 cm dia. grids that had been cut down and then masked so the diameter of the zone through which the beam could be extracted was 15 cm. This is larger than the 14 cm dia. used on the original SERT II screen grid. It is noted that this larger active beam diameter could have contributed to the baseline accelerator grid impingement currents which were typically of the order of 1% of the beam currents during the tests. This expectation is based on the observation that the outermost screen grid holes in this grid with the larger active extraction area should have been exposed to the low density plasma that is located adjacent to the anode pole piece of this thruster.

The tests were conducted by establishing stable thruster operation at a moderate beam current, a keeper current of 0.3 A, the desired flow distribution between the cathode and the main flow plenum (5%, 9% or 17% of the total 1000 mA eq xenon total flowrate through the cathode) and the desired screen grid and accelerator grid voltages (V_S and V_A respectively). The screen and accelerator voltages investigated are the ones identified by the data points on Fig. 22. Once thruster operation was stable the procedure involved increasing the discharge current in steps at fixed main and cathode flow conditions and recording discharge current and voltage, beam current, impingement current and keeper voltage at each step.

The process of increasing the discharge current and as a consequence the beam current was continued until high voltage power supply cycling began to occur (i.e. one or both of the screen and accel grid high voltage power supplies would repeatedly trip on high current and then reset). The onset of this cycling was very sudden and it is considered to have been brought on by phenomena related to either electron backstreaming or grid deformation coupled with high voltage power supply inadequacy. The occurrence of these phenomena is considered likely because the impingement currents would typically be on the order 10 mA and the beam currents would be stable in the range between 800 and 900 mA just prior to the onset of the cycling. After a fraction of a minute had elapsed at beam current operating conditions which were near the maximum values measured, a sudden, large increase in both the beam and impingement current would occur. The exact beam current level at which this cycling occurred seemed to depend on the discharge power level and for this reason it is suggested that it may have been induced by thermally driven grid

warpage. It is believed that high direct ion impingement currents would not have been observed until the beam currents were substantially higher and that the onset of these currents would have occurred more gradually if a properly designed, compliant grid mounting system had been used in place of the paper clip system. Electron backstreaming is suggested as a contributing factor in the tests conducted at the high R-value (0.9) where operating conditions were close to the electron backstreaming limit. In addition it is noted that both the positive high voltage power supply, which was being operated near its design current limit of 1000 mA in these tests, and the negative high voltage power supply were not well regulated. Any increase in either beam current (due to either increased ion current or electron backstreaming) or impingement current would cause the voltage output of the corresponding (positive or negative) high voltage power supply to drop. In either case the result was a drop in the total accelerating voltage and a decrease in the ion current extraction capability of the grids. This would be expected to lead to increased beamlet defocusing and higher impingement currents which would cause the voltage outputs of both high voltage power supplies to drop further. This process of defocusing leading to voltage drops leading to further defocusing continued to feed on itself until ultimately the observed power supply cycling problems occurred. Finally, it is suggested that the high voltage power supply cycling problem may have been made more severe because a single filament neutralizer was being used in place of a hollow cathode neutralizer.

After data had been collected over the range of beam currents from about 400 to 900 mA at a given propellant flow distribution, the

cathode and main flowrates were reset to produce the next flow distribution of interest. After data had been collected at each flow distribution condition, the high voltage operating conditions were changed and the procedure was repeated.

RESULTS

The data collected in this experiment are presented in Figs. 23 through 25. At each discharge current and high voltage operating condition identified on these figure the accelerator grid impingement current remained in the range between 10 and 15 mA until the high voltage power supply cycling mentioned in the previous paragraphs began to occur. It was the onset of this cycling that determined the maximum propellant utilization (or maximum beam current) operating condition that could be realized at each cathode flow fraction. In this regard it should be noted that all tests were conducted at a xenon flowrate of 1000 mA eq so the beam current (in mA) at any operating point is equal to the associated propellant utilization times 1000.

Figures 23 through 25 show that the highest beam currents were achieved when the cathode flow fraction was the lowest value investigated (5% of the total flow through the cathode). The data also show, however, that reducing the cathode flow fraction caused the discharge voltage to increase, and this would be expected to increase the sputter erosion rate of discharge chamber surfaces thereby shortening the thruster lifetime. If the lifetime associated with thruster operation at the lowest cathode flow fraction is sufficient for the lunar GAS mission then the data suggest this flow fraction is best. The data of Figs. 23, 24 and 25 also indicate that discharge

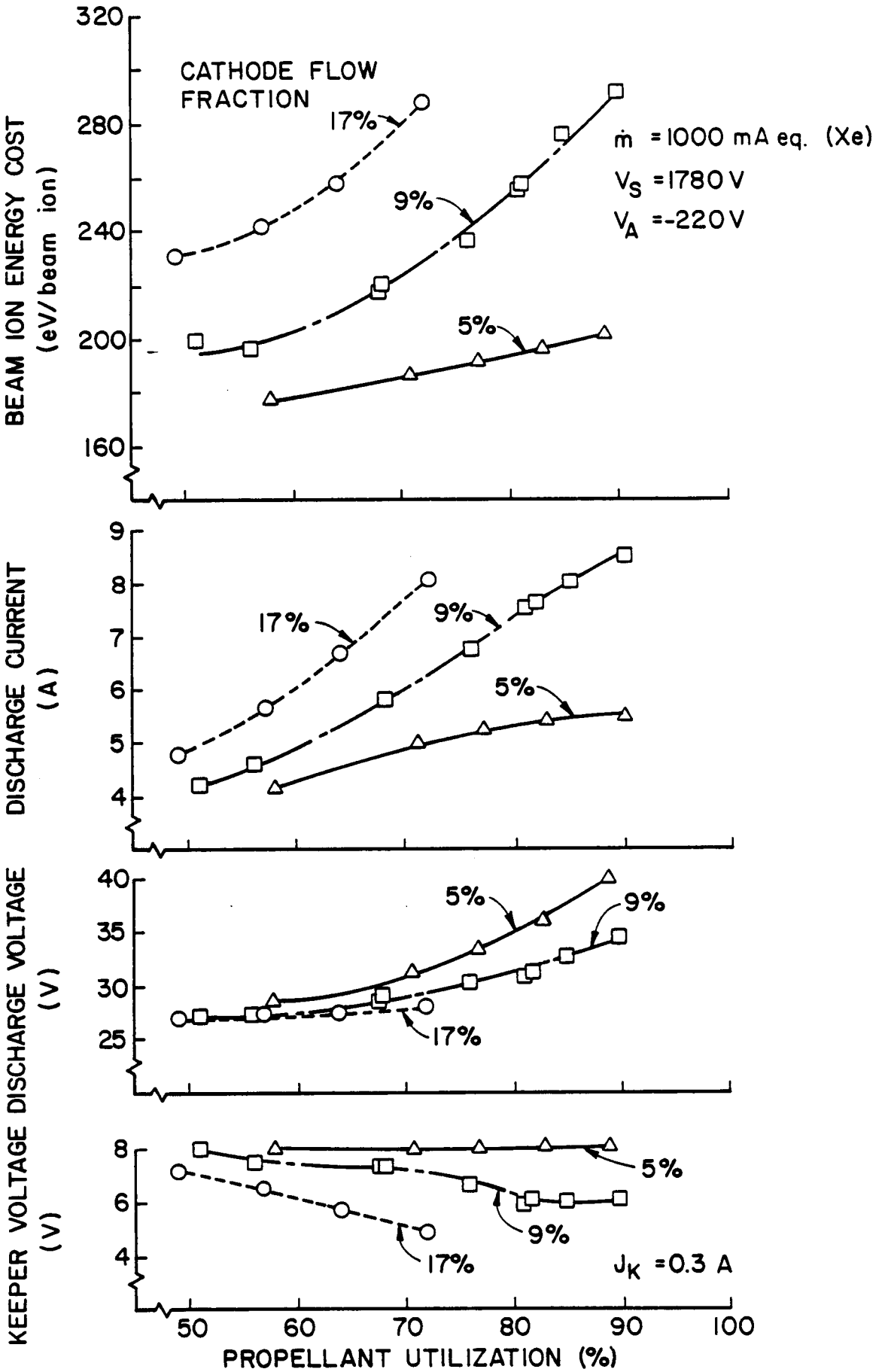

Fig. 23. Modified SERT II Thruster Performance at R = 0.91

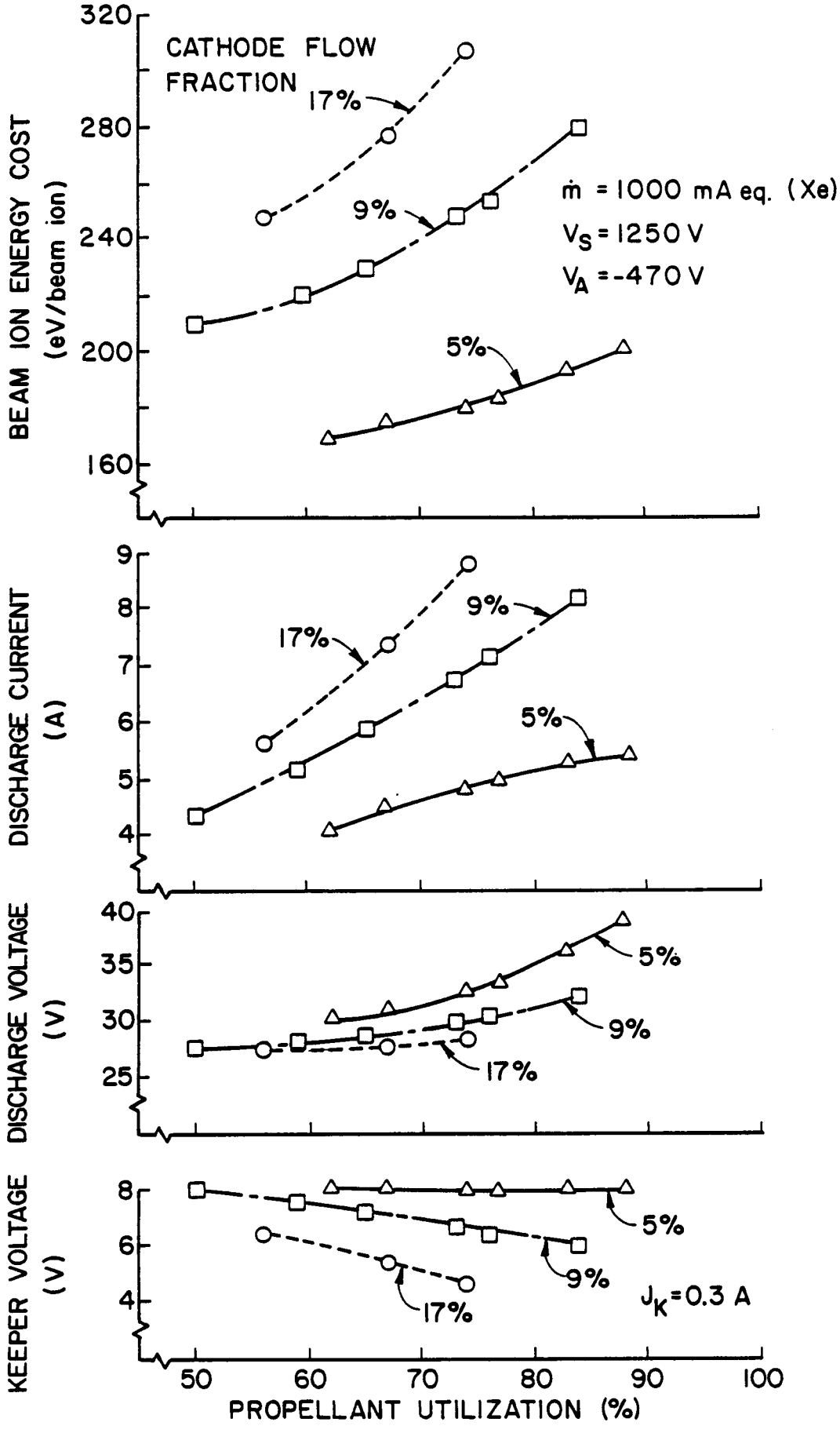

Fig. 24. Modified SERT II Thruster Performance at R = 0.73

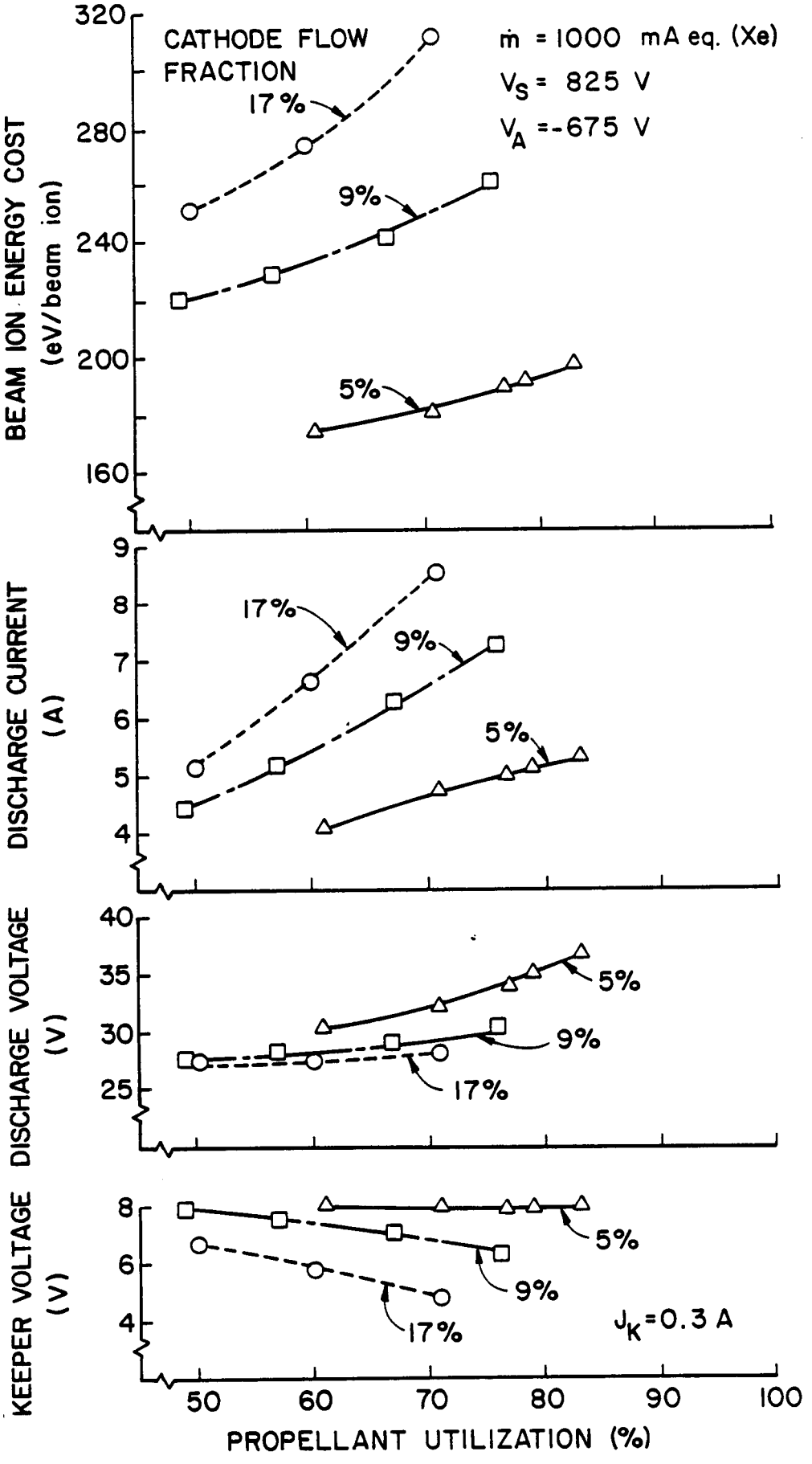

Fig. 25. Modified SERT II Thruster Performance at R = 0.55

currents approaching 9 A can be expected at low discharge voltages, that baseline beam ion energy costs are comparable to those measured when the discharge chamber was operated on mercury with similar high perveance grids[6] (~180 eV/ion) and that keeper voltages are acceptably low (< 8 V).

CONCLUSIONS

The modified SERT II ion thruster operates efficiently on xenon and it can produce the desired beam current levels at the net and total accelerating voltages prescribed for the lunar Get-Away Special mission. This thruster equipped with high perveance grids exhibits performance on xenon that is comparable to that measured operating the original SERT II thruster with high perveance grids on mercury. The grid system used in this study needs to be improved by making its mounting system more compliant and possibly by reducing the grid hole sizes (so the screen hole diameter-to-grid spacing ratio is closer to unity) to improve their beamlet divergence characteristics at high beam current levels. It appears that a cathode flow fraction near 5% should be used to achieve good discharge chamber performance, but additional work is needed to ensure component (e.g. grid system, baffle and hollow cathode) lifetimes will be sufficiently long so the thruster will be able to meet mission lifetime objectives.

HOLLOW CATHODE RESEARCH

Verlin J. Friedly

INTRODUCTION

An experimental study of the physical principles of hollow cathode operations was initiated during the grant period. Presently this research effort is focused on operation of orificed hollow cathodes operating at high discharge currents (10 to 70 A) and it is therefore intended that it will extend and compliment a similar study conducted by Siegfried.[7] Assuming these tests proceed as planned, the work will be extended to still higher discharge current levels. The principal effort on this project thus far has involved setting up the experimental equipment and demonstrating that the hollow cathodes, Langmuir probes, probe biasing and measuring equipment, and probe trace analysis routines that will be needed to conduct this research work properly at low discharge current levels (1 to 10 A). Preliminary experiments have been conducted in this low current range and data have been collected and analyzed to demonstrate this.

APPARATUS AND PROCEDURE

The schematic diagram in Fig. 26 shows the test apparatus being used for this study. This apparatus has been installed in a 30 cm dia. by 45 cm high vacuum chamber and for the tests that will be described here it included a 6.4 mm outside diameter hollow cathode with a thoriated tungsten orifice plate that contained a 1 mm dia. orifice. A 25 mm long, hollow, sintered tungsten insert treated with barium aluminate was installed as the emitting surface inside the cathode tube. The insert was electrically and mechanically connected

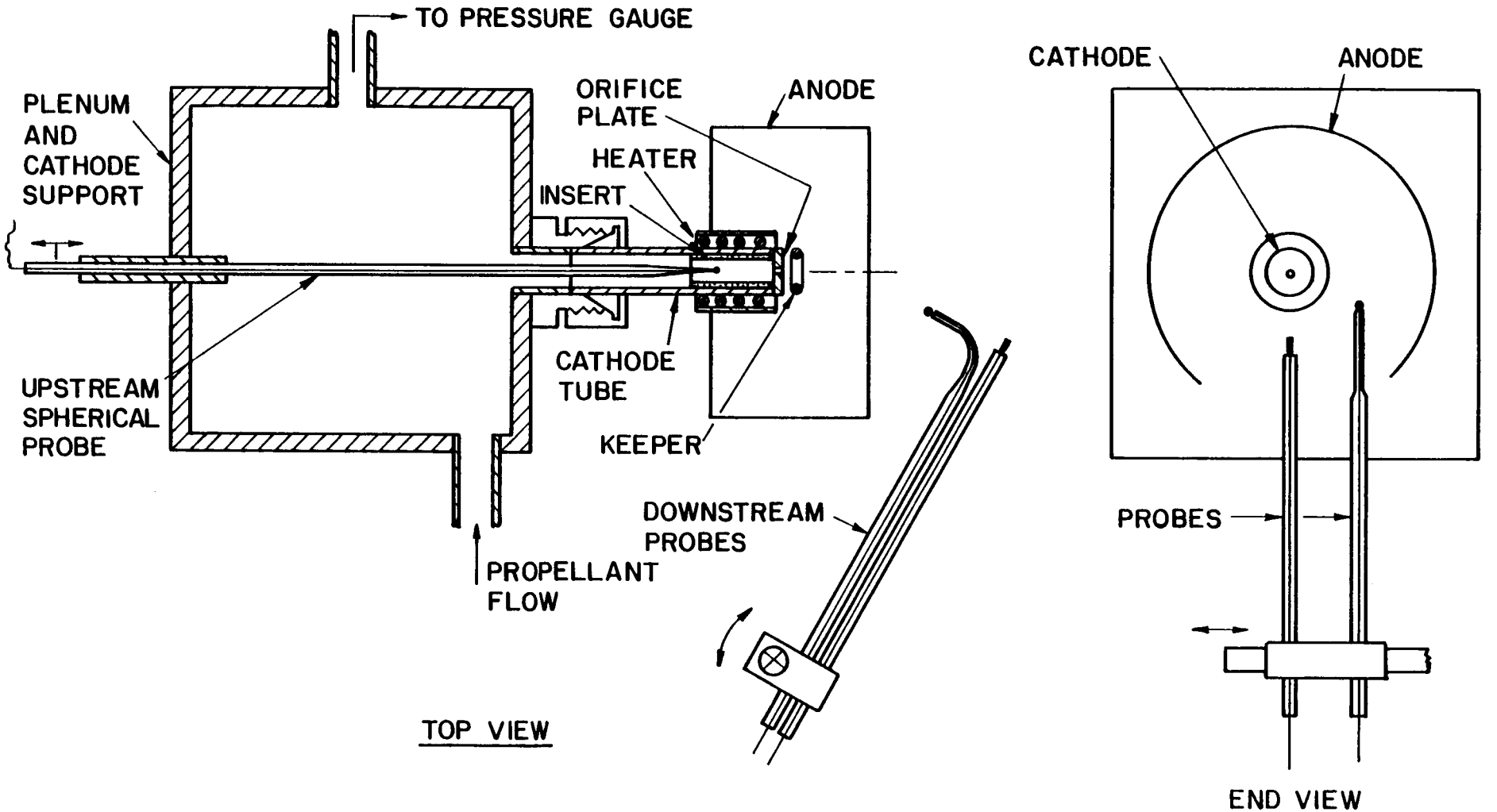

Fig. 26. Hollow Cathode System Schematic

to the cathode tube by three wires that were spot welded securely to the inside surface of the cathode tube. The cylindrical anode used in these preliminary tests, which was 57 mm in dia. and 76 mm long, was made of 0.7 mm thick perforated stainless steel. The keeper shown in Fig. 26 was a tantalum torus with a minor diameter of 1.5 mm and major diameter of 5 mm and it was located 1 mm downstream of the cathode orifice plate. The axes of the cathode, keeper and anode were all concentric. The cathode internal pressure was measured in the flow plenum shown in Fig. 26 using a capacitance gauge accurate to within ± 1 Torr.

Three Langmuir probes are used to collect plasma property data from inside (the upstream spherical probe) and outside (the downstream probes) of the cathode and Fig. 26 shows how these probes were positioned relative to the other elements of the system. The spherical probe located inside the cathode consists of a 0.8 mm dia. tungsten sphere welded to a 0.25 mm dia. tungsten wire enclosed within a 2.3 mm outside dia. quartz tube insulator. The diameter of this quartz tube has been reduced to ~1.2 mm at the end near the spherical sensor in an attempt to minimize the extent to which it interferes with the hollow cathode plasma. The entire probe assembly is designed so it can be moved axially along the cathode centerline while the cathode is operating so the spatial variations in the plasma properties within the cathode (i.e. within the upstream region) can be measured.

The other two probes, located outside of the cathode, are referred to as the downstream probes. One of these probes, a 0.8 mm dia. by 0.5 mm long tungsten cylinder protruding from a 2.3 mm dia. quartz tube insulator, is used in the region downstream of the orifice

plate where the plasma density is low (in the range of 10^{10} to 10^{12} cm^{-3}). The second downstream probe is a 0.8 mm dia. tungsten sphere located at the end of a 2.3 mm dia. quartz tube insulator which has been reduced in diameter in the region near the spherical probe sensor to minimize interference between the sensor and the plasma. This insulator is curved so the spherical probe can be swept through the high plasma density region that extends into the region between the keeper and the cathode in the manner suggested in Fig. 26. Both downstream probes can be rotated and translated as the figure suggests so plasma property data can be collected along a curved path extending downstream from the cathode orifice.

A simple electrical schematic of the circuit used to bias, measure and record the output of any of the three Langmuir probes is shown in Fig. 27. In this figure switch S_{E1} is used to connect either the upstream or downstream probes into the circuitry and then switch S_D is positioned to select which of the two downstream probes will be active. The sweep circuit, which is shown as a block in the figure, has been described by Siegfried.[7] It is used with the upstream probe where a relatively rapid sweep through the output voltages is required so contamination of the probe by low work function material from the insert within the cathode will be minimized. The lower limit on the upstream probe sweep period is limited to ~2 sec by the frequency response of the X-Y plotter used to record the data.

The downstream probes are biased using the slower but more reliable 3 kΩ potentiometer shown in the figure. In order to ensure a reliable and steady output voltage, battery packs are used as the power supply for both the sweep circuit and the potentiometer. Switch S_C is used to connect the upstream probe, first to the negative

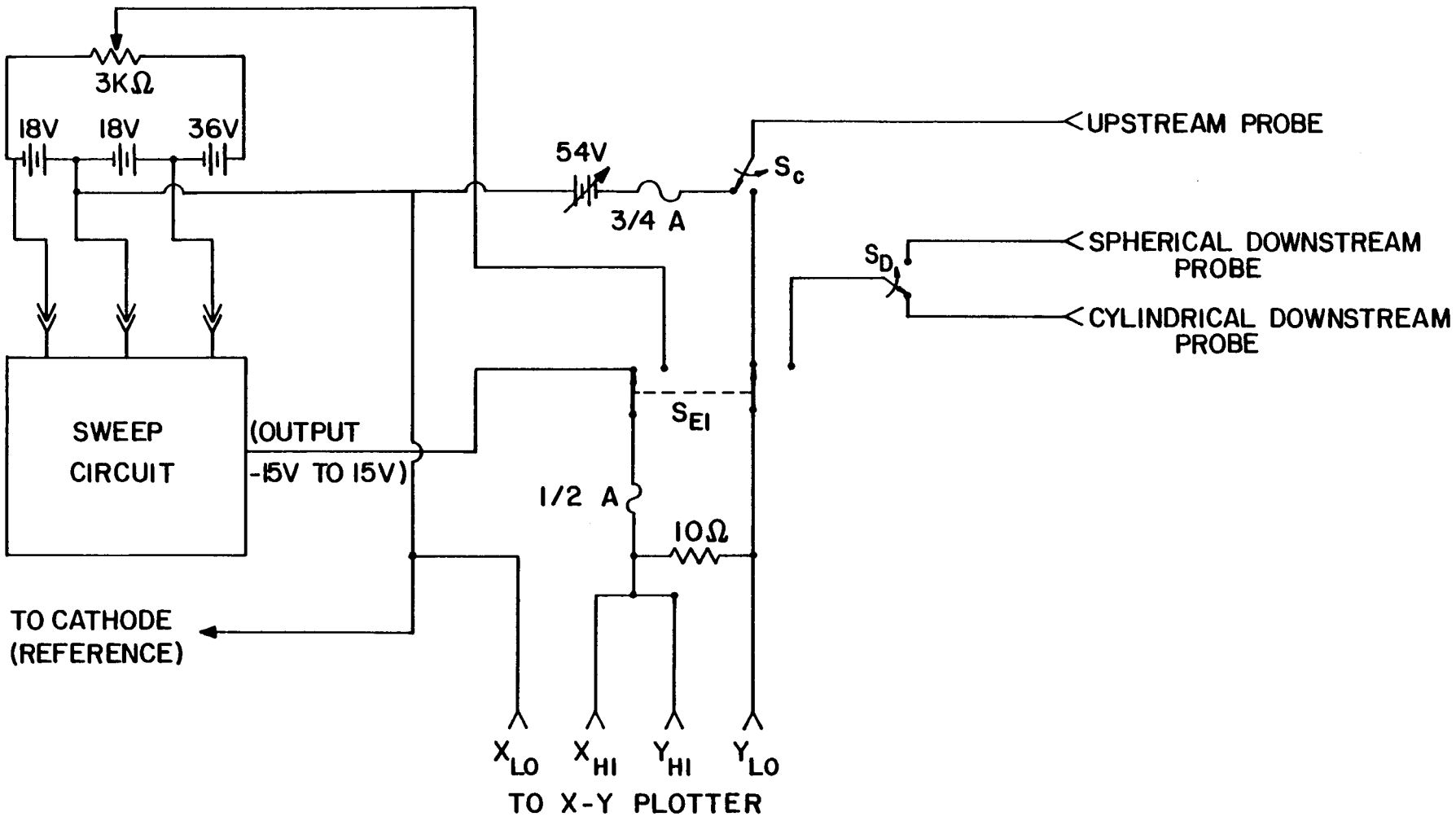

Fig. 27. Langmuir Probe System Circuitry

terminal of a 54 V power supply used to clean the probe just prior to its use and then to the sweep circuit. For all measurements the probe current is recorded as a function of probe potential using an X-Y plotter and probe potentials are measured with respect to cathode potential.

To analyze the Langmuir probe traces two methods are used, one for the spherical probe traces obtained when plasma densities are high and only the ion saturation portion of a probe trace can be collected (partial traces) and one for the cylindrical probe traces which are collected at lower plasma densities and are complete. Partial traces are collected when plasma densities are high and collection of a complete trace could melt the probe and/or change plasma conditions. To analyze data from the ion saturation regions of probe traces (i.e. from the spherical probes) a method that is basically the same as the one developed by Siegfried,[7] which has been reprogrammed for use on an IBM compatible computer, is used. Complete traces generated using the cylindrical Langmuir probe are analyzed using a modification of the basic method developed by Beattie[8] which was also reprogrammed so it could be used on an IBM compatible computer.

The electrical system used to operate the hollow cathode was simple. It consisted of two DC power supplies; one (the anode supply rated at 10 A and 40 V) was connected with its positive terminal to the anode and its negative terminal to the hollow cathode and the other (the keeper supply rated at 5 A and 150 V) was connected with its positive terminal to the keeper and its negative terminal to the cathode. Meters were provided so the anode and keeper voltages and currents could be read.

Preparation for test involved evacuating the test chamber to ~25 mTorr and allowing the cathode assembly to stand under vacuum at room temperature overnight. After this period of time it was assumed undesirable gases and vapors that could have entered the cathode as a result of being vented to the atmosphere would be pumped out through the cathode orifice. Typically, tests were initiated by heating the cathode, establishing keeper and anode potentials of 150 V and 25 V respectively and then increasing the xenon flowrate through the cathode until the discharge ignited. Once a discharge began the flowrate was reduced to ~180 mA eq (Xe), the anode (or discharge) and keeper currents were set at ~2 A and 0.4 A, respectively, and conditions were allowed to stabilize over a several minute operating period. Once the discharge stabilized the desired flowrate and the lowest discharge current of interest were set and the discharge was allowed to stabilize over a period of a few more hours. Typically the discharge was judged to be stable when the discharge and keeper voltages remained constant for ~10 minutes. After the operating conditions were recorded and Langmuir probe traces had been taken at various locations relative to the cathode orifice, the next discharge current was then set and the discharge was allowed to stabilize once again before data were collected. This procedure was repeated until the range of currents of interest had been covered. The next flowrate and the lowest discharge current of interest were then established and the process was repeated.

RESULTS

Typical plasma property profiles measured at discharge currents of 2 A (open symbols) and 6 A (solid symbols), with their respective

keeper conditions and a xenon flowrate of 247 mA eq are shown in Fig. 28. At these respective current conditions the pressures within the hollow cathode measured by the pressure gauge were 5 and 6 Torr. The diagram at the top of Fig. 28a shows where the cathode orifice plate and keeper are located and the crosshatched band at zero on each figure represents the orifice plate with the region to the left being the cathode interior (upstream) one and the one to the right being the exterior (downstream) region.

At a 2 A discharge current Fig. 28a indicates the Maxwellian electron density in the upstream region is ~4.5 x 10^{13} cm^{-3} near the orifice and it declines rapidly with upstream distance. Downstream of the orifice this density seems to be substantially lower and the density also drops off rapidly with axial distance from the orifice. It should be noted that the scaling for both density and axial distance are different for the upstream and downstream regions. When the discharge current is increased from 2 A to 6 A the data of Fig. 28a indicate the downstream Maxwellian density also undergoes a threefold increase. Data were not obtained in the region upstream of the orifice at the higher current because of a failure that developed in the probe system circuitry that has since been corrected.

The Maxwellian electron temperatures measured at the same operating conditions are shown in Fig. 28b. These data suggest a relatively constant upstream value near 1 eV and a downstream value that drops from a value near 4 eV at the keeper to a value that seems to level off near 1 eV further downstream. The data also suggest that the electron temperature is insensitive to discharge current. The plasma potential, shown in Fig. 28c, appears to increase slightly from a value close to anode potential (20 V in the 2 A case and 15 V in the

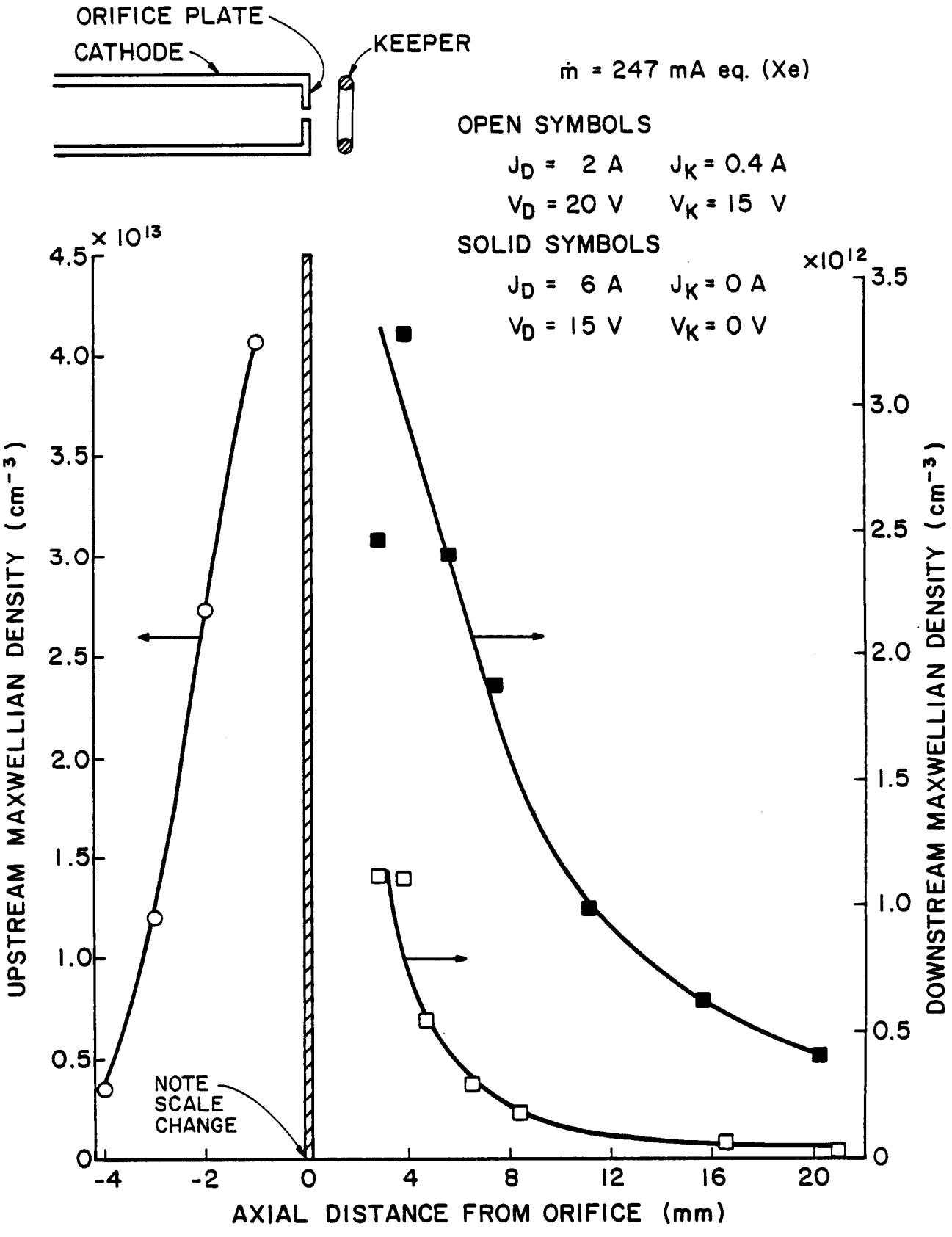

a. MAXWELLIAN ELECTRON DENSITY

Fig. 28. Hollow Cathode Plasma Properties

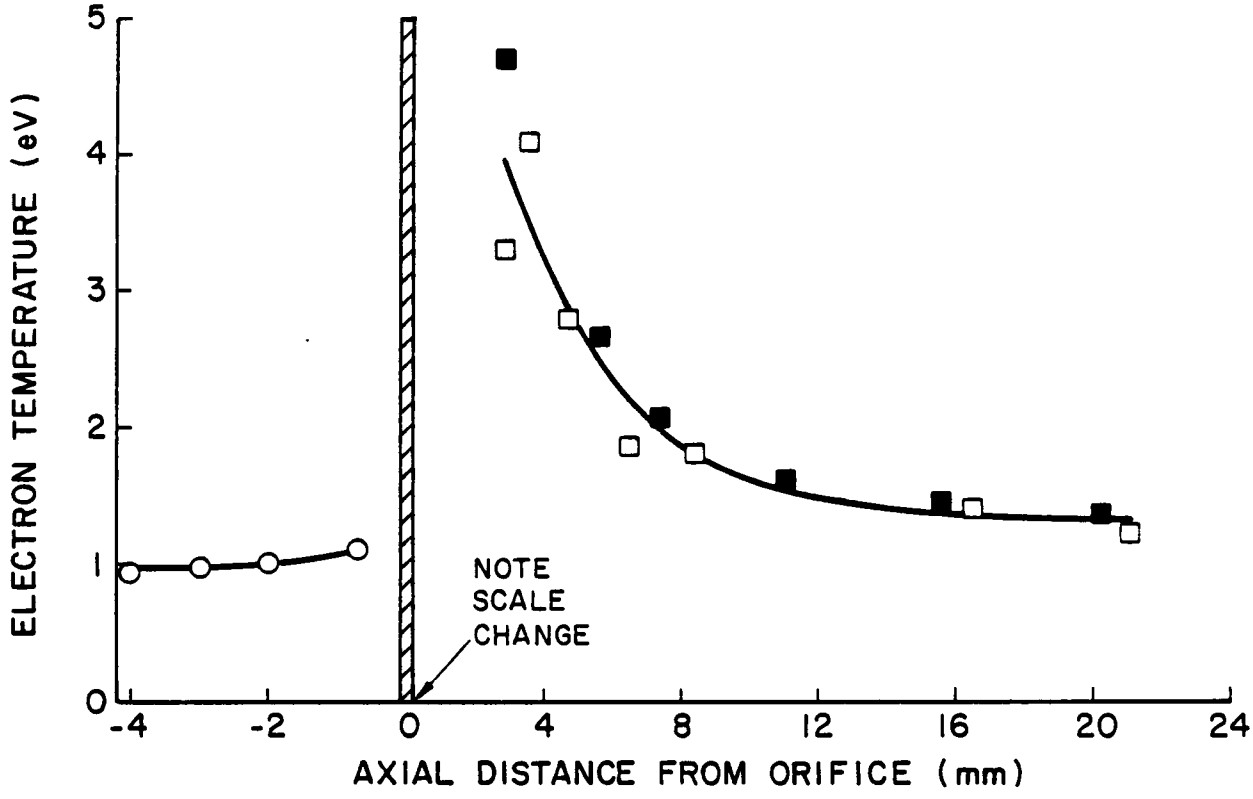

b. MAXWELLIAN ELECTRON TEMPERATURE

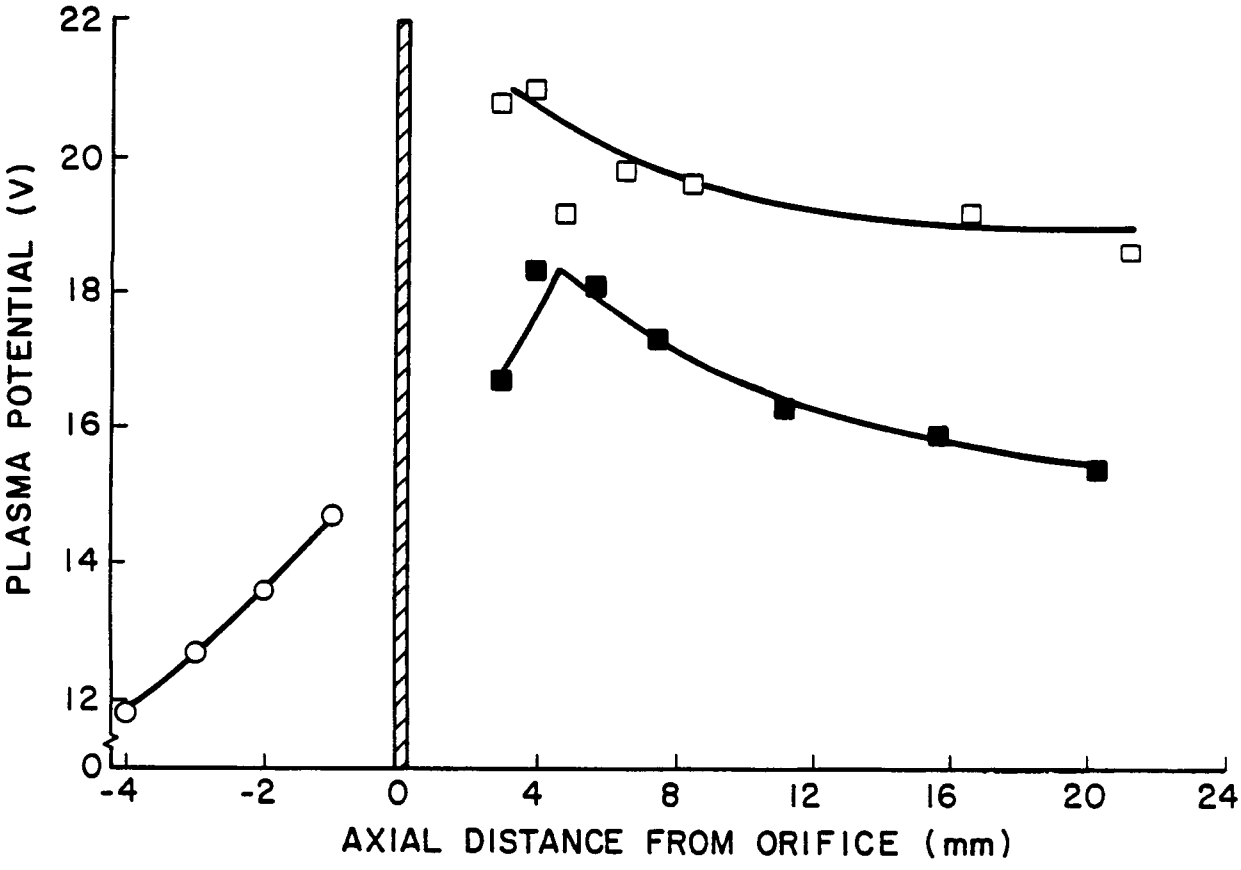

c. PLASMA POTENTIAL

Fig. 28. Hollow Cathode Plasma Properties (Cont.)

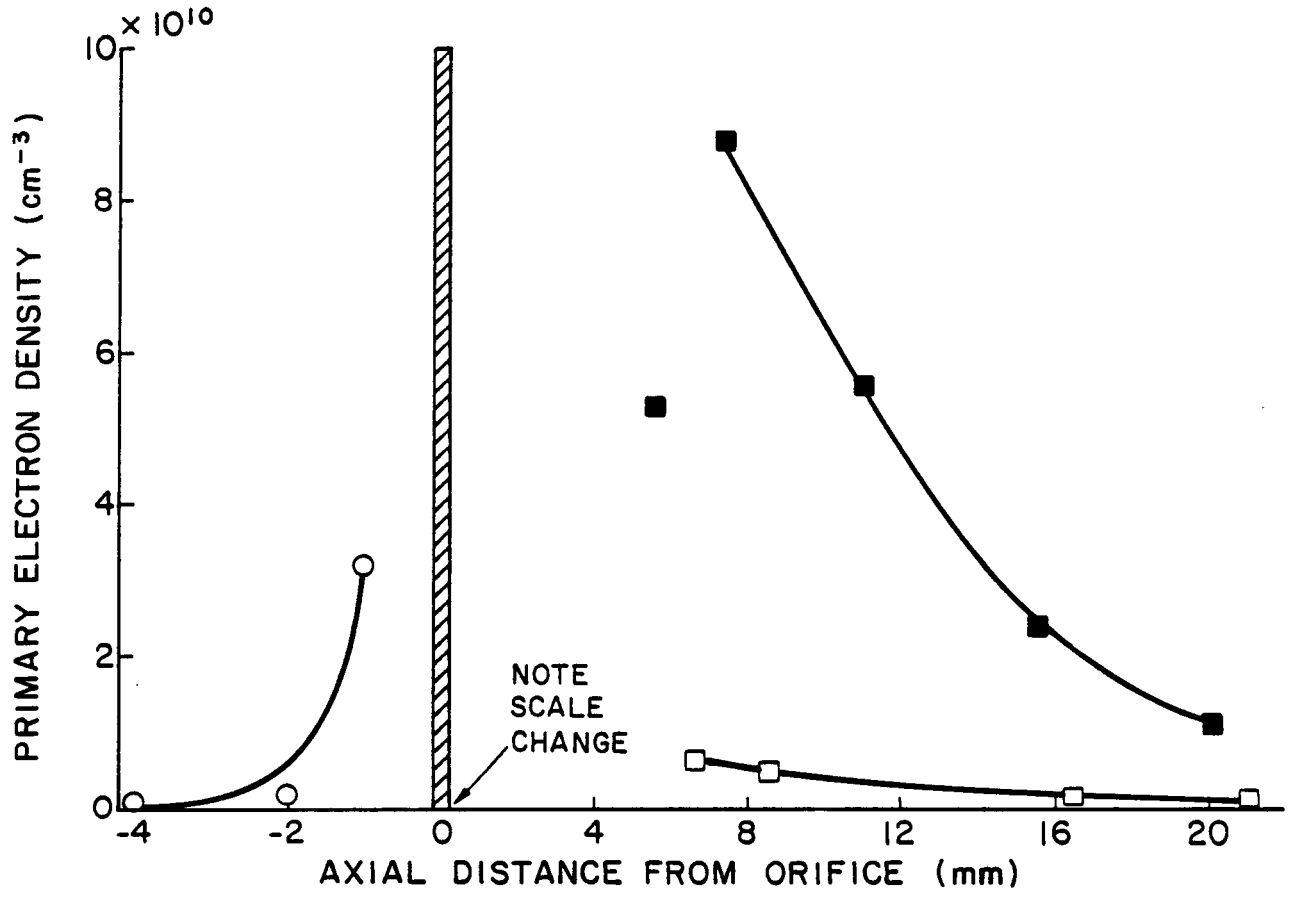

d. PRIMARY ELECTRON DENSITY

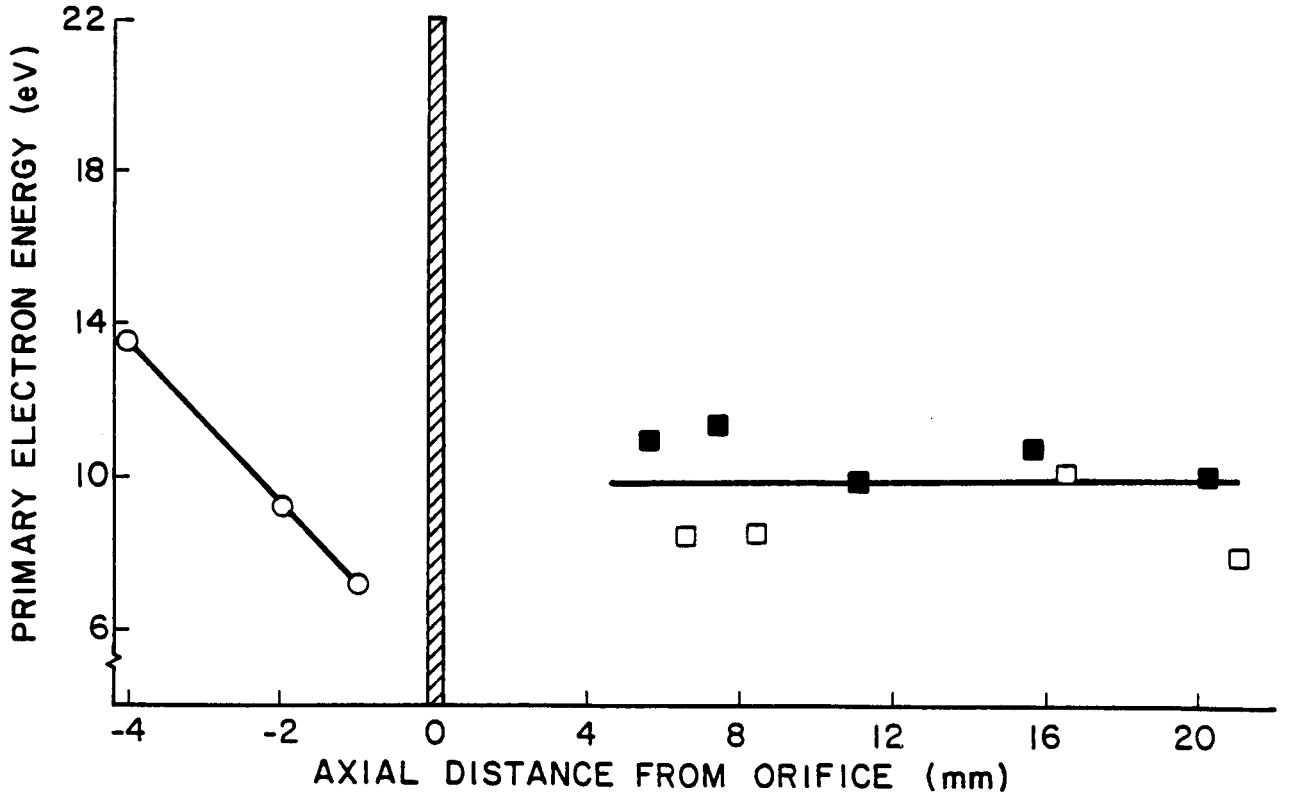

e. PRIMARY ELECTRON ENERGY

Fig. 28. Hollow Cathode Plasma Properties (Cont.)

6 A case) as the orifice plate is approached from the downstream region. These data also show a substantial potential drop across the orifice and an additional, gradual decrease in potential with upstream distance from the orifice. The fact that a voltage drop can be sustained across the orifice plate suggests that the plasma inside the cathode is coupled to that downstream of the orifice through a double sheath. A second indication of the sheath is the large change in plasma density across the orifice plate. More work is required to first demonstrate if a sheath is present and then to determine where it is located.

The density profiles for the primary (monoenergetic) electrons (Fig. 28d) follow the same pattern as that exhibited by the Maxwellian electrons, i.e. the density is highest near the orifice plate and it drops off in both directions from it and the magnitudes of the density scale with discharge current. These densities are, however, two orders of magnitude lower than the Maxwellian densities so they are probably both relatively unimportant and inaccurate. The primary electron energy profile shown in Fig. 28e shows energies that are of the proper order (the plasma potential upstream of the orifice and the orifice voltage drop downstream) and appear to be independent of discharge current but they must also be considered quite inaccurate.

CONCLUSIONS

The results that have been obtained thus far in the study agree reasonably well both quantitatively and qualitatively with those obtained previously by Siegfried.[7] This suggests that the test apparatus, test procedures and Langmuir probe analytical procedures are working properly. On the basis of this agreement, plans are

proceeding to pursue testing at higher discharge current conditions where Siegfried did not make measurements.

The large increase in Maxwellian and primary electron density observed with discharge current in this study suggests that densities an order of magnitude higher will be observed when the discharge current is increased to about 70 A. Because of this it is anticipated that the downstream spherical probe, which can be operated at high plasma densities without overheating, will have to be used over a wider range of axial positions.

REFERENCES

1. Hiatt, J.M. and P.J. Wilbur, "Ring Cusp Discharge Chamber Performance," AIAA Paper 85-2007, Oct. 1985.

2. Brophy, J.R., "Ion Thruster Performance Model," NASA CR-174810, December, 1984.

3. Nock, K.T. et. al., "Lunar Get Away Special (GAS) Spacecraft," AIAA Paper 87-1051, May 1987.

4. Kerslake, W.R., Goldman, R.G. and Nieberding, W.C., "SERT II: Mission, Thruster Performance and In-Flight Thrust Measurements," J. Spacecr. Roc., v. 8, No. 3, Mar. 1971, pp. 213-224.

5. Byers, D.C. and John F. Staggs, " SERT II Flight-Type Thruster System Performance," AIAA Paper 69-235, March 1969.

6. Wilbur, P.J., "15 cm Mercury Ion Thruster Research," NASA CR-135116, Dec. 1976.

7. Siegfried, Daniel E., "A Phenomenological Model for Orificed Hollow Cathodes," appears in NASA CR-168026, P.J. Wilbur, ed., Dec. 1982, pp 141-148.

8. Beattie, J.R., "Numerical Procedure for Analyzing Langmuir Probe Data," AIAA Journal, v. 13, No. 7, pp 950-952, 1975.

APPENDICES

Appendix A - Hollow Cathodes for Arcjet Thrusters

Appendix B - Constrained-Sheath Optics for High Thrust-Density, Low Specific-Impulse Ion Thrusters

AIAA'87

AIAA-87-1088

Hollow Cathodes for Arcjet Thrusters

C. R. Luebben and P. J. Wilbur,
Colorado State Univ., Fort Collins, CO

19th AIAA/DGLR/JSASS International Electric Propulsion Conference

May 11-13, 1987/Colorado Springs, Colorado

HOLLOW CATHODES FOR ARCJET THRUSTERS*

Craig R. Luebben+ and Paul J. Wilbur++
Colorado State University
Fort Collins, Colorado

Abstract

Ammonia hollow cathodes were tested at interelectrode pressures near atmospheric to determine if they may be suitable for arcjet thruster applications. At high interelectrode pressures, standard tantalum hollow cathodes were found to emit the electrons from a small spot on the cathode body or orifice plate. This concentrated spot emission may cause melting, and shorten the cathode lifetime. In an attempt to prevent exterior spot emission, hollow cathode bodies and orifice plates were constructed from boron nitride which is an electrical insulator, but the orifice plates melted and/or eroded at high interelectrode pressures. The most suitable hollow cathodes tested included a refractory metal orifice plate in a boron nitride body, with the insert insulated electrically from the orifice plate. In addition, the hollow cathode interior was evacuated to assure a low pressure at the insert surface, thus promoting diffuse electron emission. At high interelectrode pressures, the electrons tended to flow through the orifice plate rather than through the orifice, which could result in overheating of the orifice plate. Using a carefully aligned centerline anode, electron flow through the orifice could be sustained at interelectrode pressures up to 500 Torr - but the current flow path still occasionally jumped from the orifice to the orifice plate. Based on these tests, it appears that a hollow cathode would operate most effectively at pressures in the arcjet regime with a refractory, chemically stable, and electrically insulating cathode body and orifice plate.

Introduction

Arcjet thrusters are attractive because their specific impulse is close to optimum for many near-earth missions. The thrusters typically use a solid thoriated tungsten cathode which can overheat during operation and melt at the small spot on its tip where electron emission occurs. Thus, these cathodes may not be suitable for long-term space applications. The orificed hollow cathode used in ion thrusters, on the other hand, emits electrons from a relatively large region on its cylindrial insert,[1] so it is not as prone to overheating. The use of hollow cathodes for arcjet applications is not straightforward, however, because ion thrusters operate at interelectrode pressures of 10^{-3} Torr, whereas arcjets operate at pressures near 1000 Torr. Some difficulty has been experienced with operation of typical tantalum hollow cathodes as the interelectrode pressure is increased above about 12 Torr, because the diffuse electron emission from the insert transforms to concentrated spot emission from the exterior of the cathode tube or the orifice plate.[2,3] This spot discharge is similar to that at the tip of the thoriated tungsten cathode, and may lead to a shortened cathode lifetime.

The major ojectives of this study have been to determine if some type of a hollow cathode might be suitable for arc jet applications, and to identify the factors that facilitate high pressure operation. The approach has been to increase the operating range gradually from the low pressures where hollow cathodes operate satisfactorily, and their characteristics are understood, to the high pressures where arcjets operate. Several modifications were required to achieve satisfactory high pressure operation. The modified cathodes and their operating characteristics are described below.

Apparatus and Procedure

A schematic of the hollow cathode test apparatus is shown in Fig. 1. This apparatus is located in a vacuum bell jar where the interelectrode pressure can be controlled over a range from 10^{-2} to 10^{3} Torr. The hollow cathode body, the insert, the orifice plate, and the anode are the elements of primary interest. Most tests were conducted with a 6 mm diameter R-500 treated tantalum foil insert isolated electrically from the orifice plate by a boron nitride hollow cathode body. Quartz and tantalum hollow cathode bodies were also tested. The quartz bodies allowed the discharge to be observed visually. Tantalum cathode bodies, which are generally used in ion thruster hollow cathodes were tested with four types of inserts - lanthanum hexaboride, impregnated tungsten, bare tantalum foil, and R-500 treated tantalum foil.

The discharge was operated with ammonia propellant using two different flow arrangements. In the normal flow mode, the valves shown in Fig. 1 were adjusted to feed the ammonia through the cathode support structure to the cathode interior region and

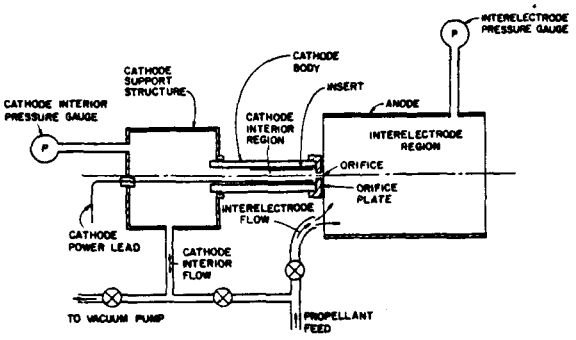

Fig. 1 Hollow Cathode Test Apparatus Schematic

*Work supported by NASA Lewis Research Grant NRG-06-002-112

+Research Assistant, Dept. of Mech. Engr.

**Professor, Dept. of Mech. Engr., Member AIAA

then through the orifice to the interelectrode region. In the reverse flow mode, the valves were arranged to feed the propellant into the interelectrode region from where it could be drawn through the orifice into an evacuated cathode interior region. Reverse flow allowed a low cathode interior pressure to be maintained while the interelectrode pressure was kept high.

The discharge was generally started during the tests using normal flow, with interelectrode and cathode interior pressures between one and five Torr. The flow was then switched to the reverse mode, and the interelectrode pressure was elevated by increasing the ammonia flowrate into this region. As the interelectrode pressure increased, the anode voltage was also increased to maintain the desired discharge current (between 2A and 14A). At various intervals of interelectrode pressure, the discharge current, anode voltage, interior cathode pressure, and sometimes orifice plate voltage were measured and recorded. Also, an emissive probe[4] was used during some tests to determine plasma potential profiles through the interelectrode region.

Two test apparatus orientations were used. With the horizontal orientation, a 5 cm diameter tantalum anode was horizontally oriented concentric with the orifice centerline, in the manner suggested in Fig. 1. In this orientation the interelectrode region was open to the bell jar to allow emissive probing and visual observation of the discharge. Unfortunately, free convective flow patterns developed in the interelectrode region at high interelectrode pressures, causing the discharge to become unstable. To alleviate the stability problem, the vertically oriented test apparatus shown in Fig. 2 was constructed. This assembly is also enclosed within an evacuated bell jar to prevent release of ammonia during high pressure tests. With the apparatus of Fig. 2, two anode configurations could be established. With the centerline anode configuration electrons are drawn to the conical tip of the 8 mm diameter tungsten rod, shown in Fig. 2. The concentric anode configuration is established by removing the tungsten rod and drawing the electrons to the 2 cm diameter copper support structure. To avoid overheating, the support structure is water-cooled. For reverse flow, ammonia is fed into the interelectrode regions through the vortex tubes, which are designed to induce swirl flow and promote stability.[4] The support structure also includes a quartz window which allows limited visual observation of the discharge. Boron nitride, graphite, and tungsten orifice plates were each tested with boron nitride cathode bodies in the vertical orientation. Several orifice diameters, ranging from 0.25 mm to 6.0 mm (open-ended) were used in these tests. The graphite and tungsten orifice plates were generally attached to the boron nitride cathode bodies in the manner suggested by Fig. 3. This figure also shows the centerline anode removed, with the copper support structure serving as a concentric anode.

Results

One important finding of this study was observed previously and studied extensively by Siegfried:[1] a rise in the cathode interior pressure causes the insert emission region to decrease in size. Siegfried found that the length of the electron emission region is of the order of one or two primary mean free paths. Hence, increasing cathode interior pressure causes the electron mean free path length and as a result the electron emission length to decrease. Tests conducted with a quartz hollow cathode body in the horizontal orientation allowed the emission region to be observed visually. At cathode interior pressures near 0.1 Torr, the electrons were being emitted diffusely from the interior surface of the insert, over a length of about 2 mm. As the pressure increased, the emission length was observed to decrease until the entire electron emission was concentrated on the edge of the insert at cathode interior pressures near 10 Torr. The concentrated electron emission causes intense heating of the insert, and resulted in melting of the quartz cathode body at cathode interior pressures around 100 Torr.

The performance of a hollow cathode and insert for arcjet applications is largely determined by the voltage drop distribution between the cathode and the anode. Data showing a typical distribution were

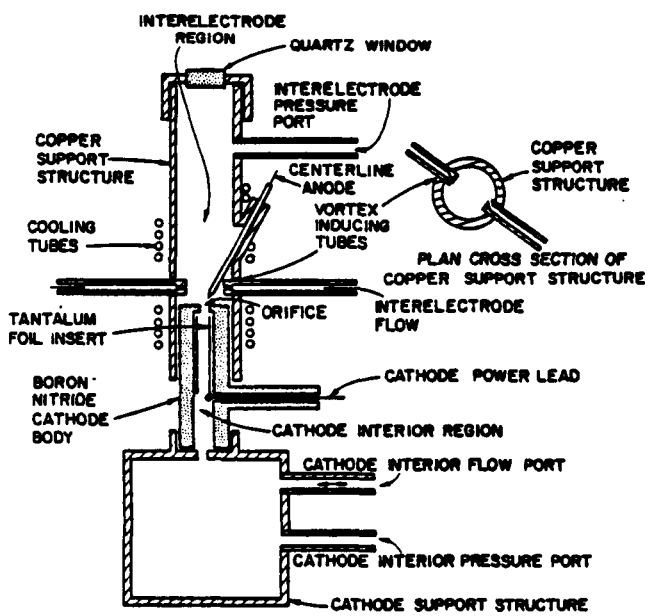

Fig. 2 Hollow Cathode Test Apparatus

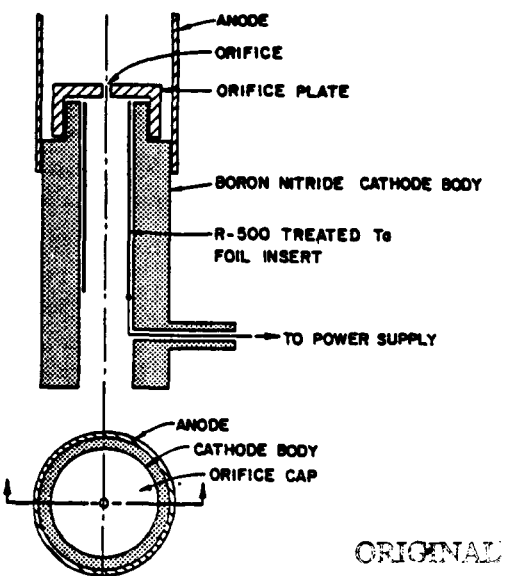

Fig. 3 Hollow Cathode Components

obtained using an emissive probe[5] with a 4A discharge from an open-ended boron nitride cathode in the horizontal orientation. The data, presented in Fig. 4, show that a substantial increase in anode voltage is required to sustain the discharge as the interelectrode pressure increases. Fig. 4 also shows that the anode fall and bulk plasma voltage drop comprise most of the cathode-to-anode voltage drop, and that both increase substantially with interelectrode pressure. The bulk plasma voltage drop occurs through the plasma in the interelectrode region, and determines the power available for heating the plasma in an arcjet. Hence, it is desirable for most of the voltage drop to occur there. The anode fall is the voltage drop through the plasma sheath at the anode, and it determines the power lost to heating the anode. The cathode fall is the voltage drop through the plasma from the insert to a point immediately adjacent to the orifice plate exterior. The cathode fall determines the power for heating the insert, sustaining the cathode interior discharge, and extracting electrons through the orifice. The cathode fall remains relatively constant as the interelectrode pressure increases to 25 Torr, so the hollow cathode itself appears to run efficiently at these pressures. Unfortunately, data could not be collected at interelectrode pressures above 30 Torr because the emissive probe repeatedly melted.

Four types of inserts were tested with a tantalum cathode body in the horizontal orientation and the anode voltage was measured at several cathode interior pressures up to 30 Torr. Typical anode fall and bulk plasma voltage drop values were subtracted from the anode voltage at each pressure interval to give an estimate of the cathode fall. Figure 5 shows the voltage drop at the cathode (cathode fall) plotted against cathode interior pressure for each insert. The bare tantalum foil insert exhibited the highest cathode fall, ranging

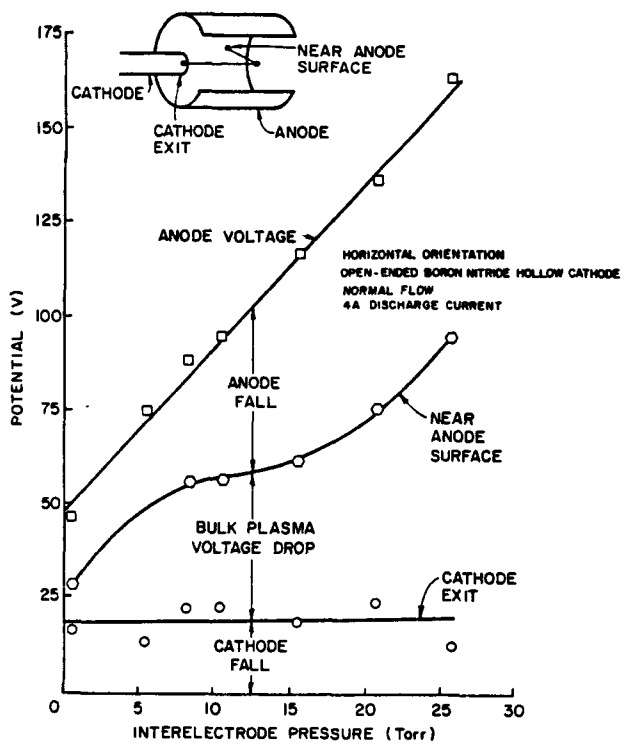

Fig. 4 Voltage Drop Distribution

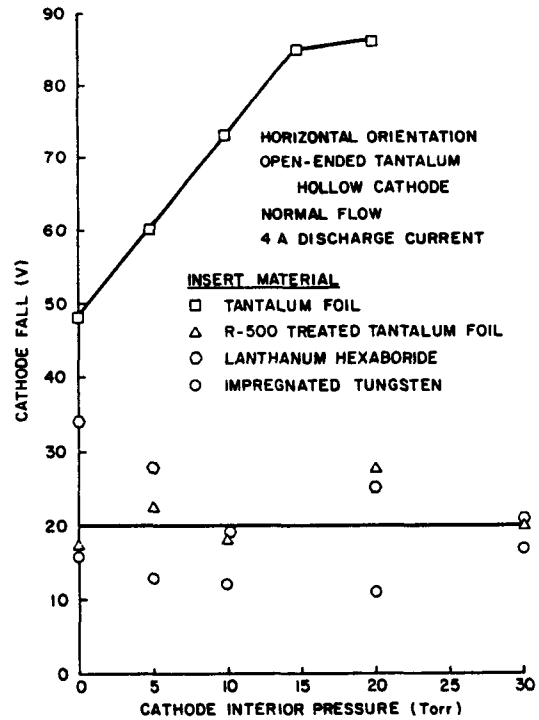

Fig. 5 Cathode Fall Versus Cathode Interior Pressure for Various Inserts

from 50 to 85 volts over the pressure range tested. The R-500 treated tantalum foil, lanthanum hexaboride, and impregnated tungsten inserts each contain a low work function agent, which decreases the voltage required for electron emission. The impregnated tungsten, R-500 treated tantalum foil, and lanthanum hexaboride inserts exhibited similar cathode falls, averaging near 20 volts. Unfortunately, as the cathode interior pressure increased above about 12 Torr, the electron emission site would jump from the insert to a spot on the tantalum cathode tube, which was connected electrically to the insert. This was similar to the spot emission from a solid tungsten cathode, and could result in overheating of the cathode at higher pressures. It was recognized that this spot emission from the cathode body or orifice plate could be prevented if these two components were constructed from an insulator that enclosed the electron emission source (the insert). Both quartz and HBC grade boron nitride insulators were used in this application, but the boron nitride was preferred because it has a higher melting temperature. Hence, all data in subsequent figures were obtained using a boron nitride cathode body. Since the R-500 insert performed as well as the other inserts tested, it was selected for use in subsequent tests. These results suggest that all of the inserts except the bare tantalum foil perform satisfactorily with ammonia at cathode interior pressures below about 12 Torr for short duration tests. For longer tests the impregnated tungsten and lanthanum hexaboride inserts would be expected to outperform the R-500 treated tantalum foil insert.

Figure 6 shows anode voltage versus interelectrode pressure data measured with a boron nitride cathode operating at a 14A discharge current with normal flow. Operation tended to be somewhat unstable in these tests, with the anode voltage

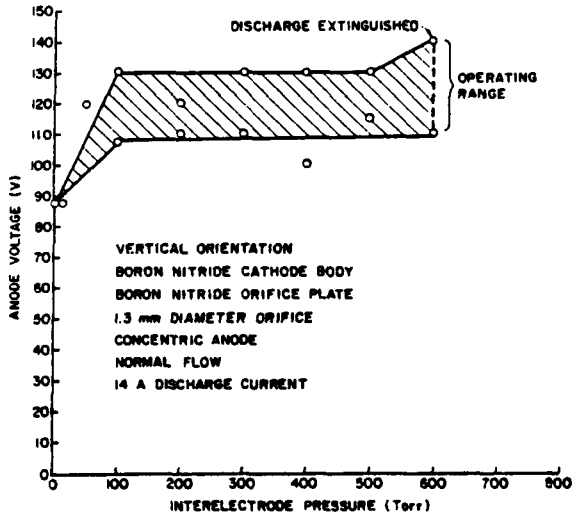

Fig. 6 Anode Voltage Versus Interelectrode Pressure with Normal Flow

fluctuating between the upper and lower limits shown in Fig. 6. The discharge could not be maintained at interelectrode pressures above 600 Torr. After the test, the cathode was disassembled and its interior surface was found to be a mixture of boron nitride and tantalum from the insert that had melted together. It is believed that this cathode and insert damage occurred near the end of the test when the highest cathode interior pressures were reached. After this damage had occurred, the electrons were apparently emitted from the molten boron nitride and tantalum mixture. The reverse flow mode was investigated to determine if it would facilitate proper cathode operation by maintaining a low cathode interior pressure while the interelectrode pressure was high. Figure 7 shows that with reverse flow and a small diameter orifice, the cathode interior pressure can be maintained well below the interelectrode pressure. In comparison, the normal flow mode results in cathode interior pressures slightly greater than the interelectrode pressure. Near the end of the tests associated with Fig. 7, with the cathode operating at high interelectrode pressures, the orifice plate overheated and the orifice enlarged. As a result the cathode interior pressure increased to the point where the electron emission

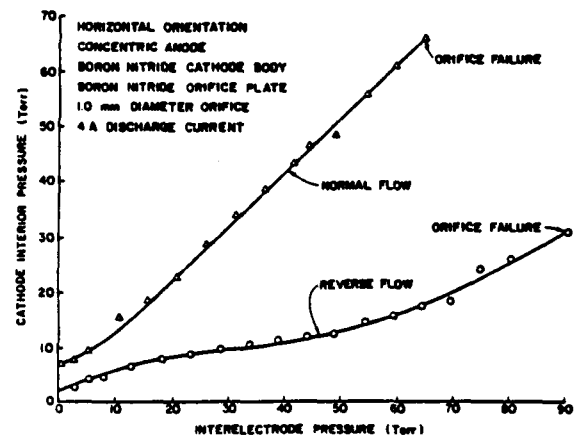

Fig. 7 Cathode Interior Pressure Versus Interelectrode Pressure with Normal and Reverse Flow

became concentrated at a small spot on the insert. This caused insert degradation which apparently caused a 10 to 20 volt rise in anode potential that was observed near the end of the test sequence at high interelectrode pressures. This effect was observed in both the normal and reverse flow modes, but reverse flow allowed higher interelectrode pressures to be achieved before the orifice failure occurred. As shown in Fig. 8, both normal and reverse flow require similar anode voltages to sustain the 4A discharge. Hence, the flow direction has little effect on the anode voltage. Another series of tests revealed that the anode voltage is also independent of the ammonia flowrate and the orifice diameter. Thus, for a given hollow cathode and anode configuration, propellant gas, and discharge current, the anode voltage appears to depend primarily on interelectrode pressure.

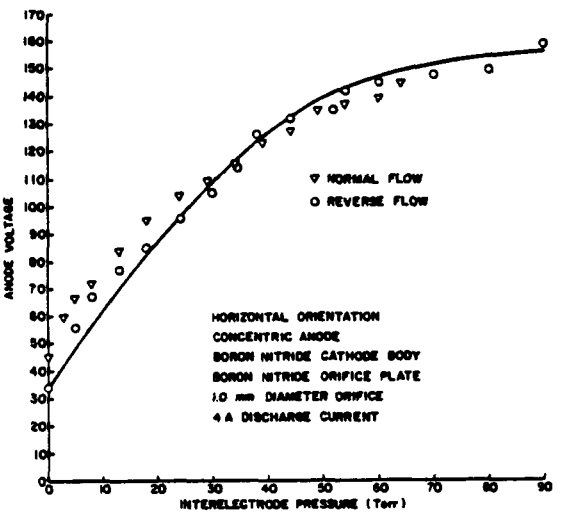

Fig. 8 Anode Voltage Versus Interelectrode Pressure with Normal and Reverse Flow

The current level also affects the anode voltage required to sustain the discharge. Figure 9 illustrates the negative resistance phenomena observed in arc discharges a higher current results in a lower anode voltage. This occurs because the plasma resistivity is proportional to the ratio of electron collision frequency to electron density;

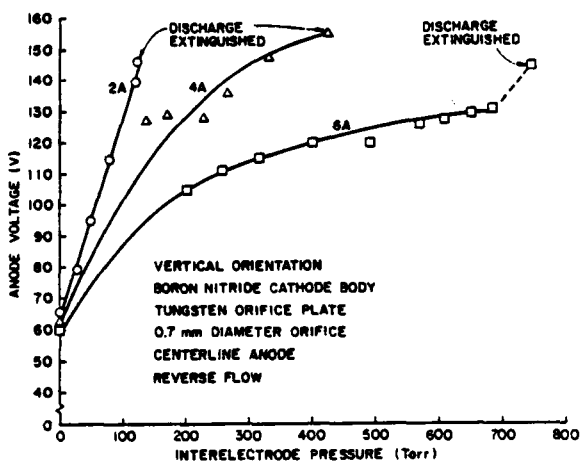

Fig. 9 Anode Voltage Versus Interelectrode Pressure at Various Current Levels

increasing the discharge current causes the electron density to increase more rapidly than the collision frequency, so the resistance decreases. With the 2A discharge current, the discharge became unstable and repeatedly extinguished at interelectrode pressures near 125 Torr. Figure 9 shows that 4A discharge current operation could be extended to 425 Torr, and 6A operation was achieved at pressures as high at 750 Torr. With higher currents the discharge was operated to interelectrode pressures of 1000 Torr.

The cathode orifice plate material also appears to influence the anode voltage versus interelectrode pressure characteristics, as indicated in Fig. 10. At relatively low pressures (around 60 Torr) with a 12A discharge current the boron nitride orifice (circular data points) began to melt and/or erode rapidly. This resulted in orifice enlargement which caused the cathode interior pressure to rise, allowing spot emission from the insert which led to insert degradation. The anode voltage is seen in Fig. 10 to increase rapidly with interelectrode pressure up to 150 Torr, where an anode voltage of 150 volts was required to sustain the 12A discharge. The discharge repeatedly extinguished at pressures above 150 Torr. Thus, a boron nitride orifice plate does not appear suitable for high pressure operation. The graphite orifice plate (square data points) performed better than the boron nitride one. The anode voltage increased slowly with interelectrode pressures, and a 12A discharge was sustained to 1000 Torr, with an anode voltage of only 120V. After a few hours of operation the graphite orifice plates were also found to be eroded; dozens of hemispherical depressions provided evidence that the electron emission had been coming from the orifice plate exterior at high interelectrode pressures. Of the three orifice plate materials tested tungsten exhibited the best operating characteristics. The required anode voltage was relatively steady at about 100 volts for interelectrode pressures in the range from 150 to 1000 Torr. After testing the tungsten orifice plate exhibited no signs of melting or erosion, so tungsten may be a suitable material for high pressure operation.

Visual observation of the discharge with the tungsten orifice plate could be made through the quartz window shown in Fig. 2. Such observations revealed the electron emision coming through the orifice at low interelectrode pressures with the concentric anode but increasing this pressure into the range near 150 Torr caused a transition to occur: the site of the electron current passage moved from the orifice to a spot on the orifice plate even though the orifice plate was electrically isolated from the insert. At interelectrode pressures above this transition point, the current flow through the orifice plate prevailed. Apparently, after the transition occurs the electrons are emitted from the insert and they flow through the cathode interior plasma to the interior surface of the orifice plate. Then they flow through the orifice plate and are emitted from its exterior surface to the interelectrode region, where they are attracted to the anode. It is postulated that the impedance along this path is actually less than the impedance of the path through the orifice itself at the high interelectrode pressures. This is supported by the data of Fig. 11, which show a 30 volt decrease in anode voltage (upper curve) at the transition point. The data of Fig. 11 were obtained using a centerline anode in the vertical test orientation. In comparison with a concentric anode, the centerline anode decreases the current path length and hence the impedance through the interelectrode plasma from the orifice to the anode. To facilitate viewing of the orifice, however, the anode tip was offset from the orifice centerline by about 2 mm. With this arrangement the transition to current flow through the orifice plate rather than through the orifice occurred at interelectrode pressures near 260 Torr. It was concluded that the change from the concentric anode to the centerline anode facilitated the increase (from 150 to 260 Torr) in the transition pressure.

Comparing Figs. 4 and 11, it can be seen that the orifice plate voltage is about equal to the cathode fall at low interelectrode pressures. Hence, the orifice plate voltage was taken as a reasonable estimate of the cathode fall. At the tran-

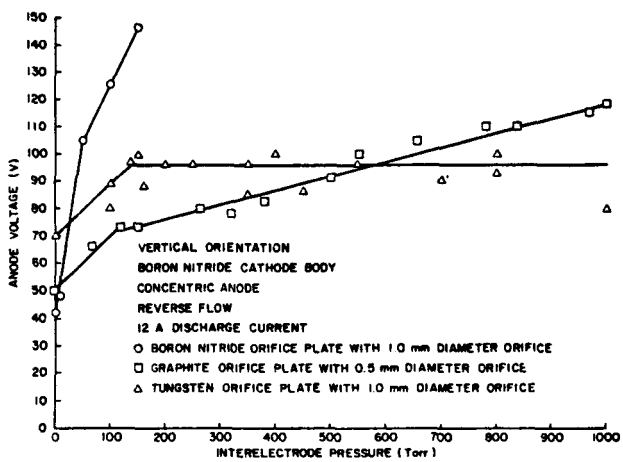

Fig. 10 Anode Voltage Versus Interelectrode Pressure for Various Orifice Plate Materials

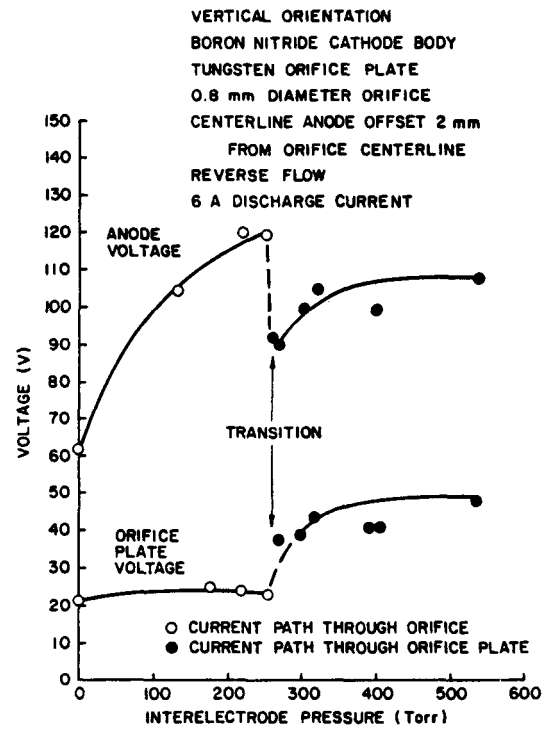

Fig. 11 Anode and Orifice Plate Voltage Versus Interelectrode Pressure

sition point, this voltage is shown to increase by 15V. During other tests the orifice plate voltage remained constant at around 25 volts before and after the transition. The reason for this discrepancy is not known.

To decrease the path length from the insert through the orifice to the anode further, the anode tip was aligned with a fraction of a millimeter of the orifice centerline. Figure 12 shows that the transition pressure was raised to 375 Torr with the anode along the centerline; nonetheless, the undesired current flow path through the orifice plate developed at all pressures above the transition. The cathode interior pressure was also observed to drop slightly with the transition to current flow through the orifice plate, as shown in Fig. 13. This may be due to the change in pressure drop at the orifice induced by eliminating the electron and ion flow through the orifice when the transition occurs.

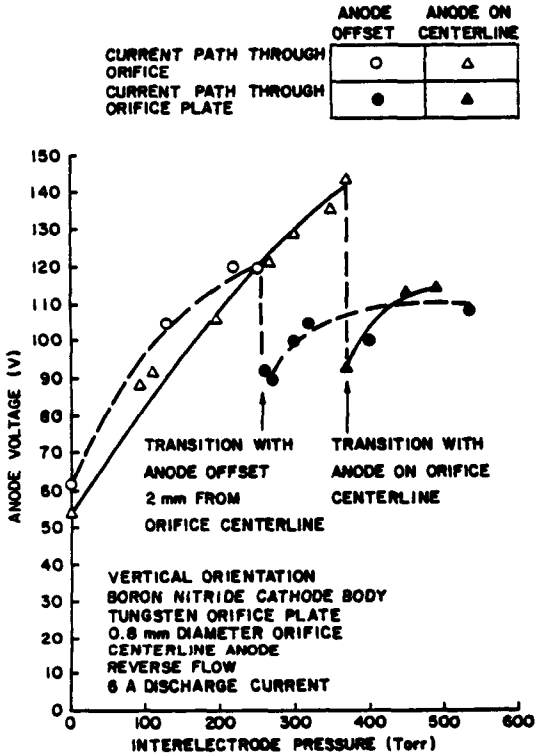

Fig. 12 Effect of Anode Position on Voltage/ Interelectrode Pressure Characteristics

One final modification was made to decrease the path length from the insert to the anode: the insert diameter was decreased to 2 mm. As a result of this it was possible to sustain a discharge through the orifice at interelectrode pressures up to 500 Torr. The anode and orifice plate voltages associated with this change are shown plotted against interelectrode pressure in Fig. 14. Even with this configuration, however, emission was occasionally observed to come from the orifice plate exterior at pressures over 400 Torr. Hence it appears that no strong tendancy exists for the discharge to come through the orifice at high interelectrode pressures.

Based on the results of this study, it appears that an ideal orifice plate and cathode body material would have the following properties:

1) electrical insulation, to prevent current flow through the orifice plate or body;

2) high melting temperature;

3) chemical stability in the presence of typical high temperature arcjet propellants.

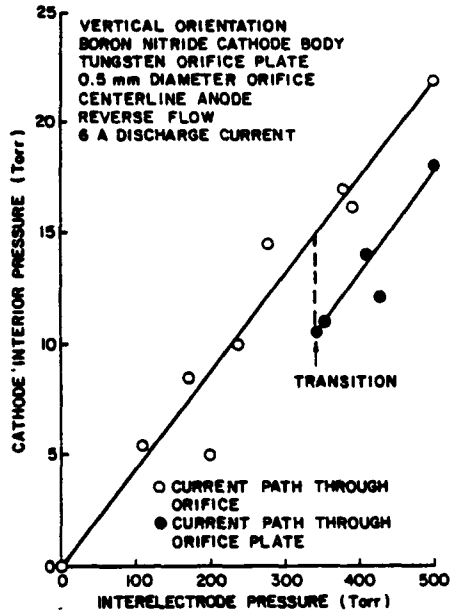

Fig. 13 Effect of Transition on Cathode Interior Pressure

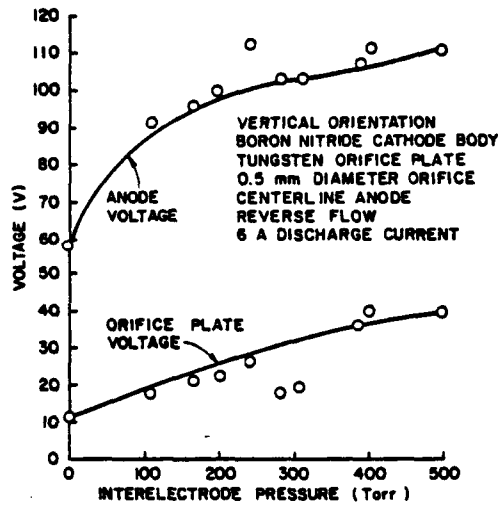

Fig. 14 Anode and Orifice Plate Voltage Versus Interelectrode Pressure

One material which may best meet these requirements is diamond, but no tests were conducted with a diamond orifice plate. It should be noted that some material problems were observed when ammonia propellant was used with a tantalum anode and insert: after high pressure operation one anode and many inserts became highly embrittled. Auger electron spectroscopy[6] of the anode revealed that nirogen atoms had diffused into these surfaces and this may have caused the embrittlement. Hydrogen is also

known to embrittle materials, but its presence cannot be detected using auger electron spectroscopy.

Conclusions

Results of this study have led to the following conclusions:

1) Hollow cathodes will operate satisfactorily with ammonia propellant.

2) The cathode fall remains relatively small at higher pressures, so the hollow cathode itself should not introduce significant inefficiences into arcjet operation.

3) Ammonia hollow cathodes will operate satisfactorily with bare tantalum foil, R-500 treated tantalum foil, lanthanum hexaboride, and impregnated tungsten inserts, but a substantially higher anode voltage is required to operate with the bare tantalum foil insert.

4) The cathode insert must be electrically isolated from the orifice plate in order to keep the electron emission site on the insert. Emission from the orifice plate or cathode body is undesirable because it may result in melting of these cathode components.

5) High cathode interior pressures promote electron emission from a small spot on the insert which leads to its degradation and eventual destruction.

6) Hollow cathode operation at high interelectrode pressures requires a low interior cathode pressure to promote diffuse electron emission from the insert. This can be attained using:

a) reverse propellant flow, and
b) a small orifice diameter.

7) Given a hollow cathode and anode geometrical configuration and materials, propellant gas, and discharge current, the cathode-to-anode voltage drop appears to depend primarily on interelectrode pressure.

8) The cathode body and orifice plate must be constructed from high melting temperature materials that can endure high pressure operation.

9) Tungsten is preferred as an orifice plate material over boron nitride and graphite because it sustained no damage during high pressure testing.

10) Cathode operation becomes more stable at high pressures as discharge currents are increased above 6A.

11) As interelectrode pressure is increased there is a tendancy for the current to flow through the orifice plate rather than from the orifice. This tendancy could be eliminated if the orifice plate could be fabricated from a sufficiently high melting temperature, insulating material.

12) Hollow cathodes with tungsten orifice plates can be operated to interelectrode pressures of 500 Torr with a diffuse emission from the cathode insert and current flow through the cathode orifice.

References

1. Siegfried, D., "A Phenomenological Model for Orificed Hollow Cathodes," NASA CR 168026, December 1982, pp. 37-60.

2. Hardy, T., and Curran, F., "Hollow Cathodes in High Pressure Arc Discharges," NASA TM 87098, September 1985, p. 2.

3. Wilbur, P., "Advanced Electric Propulsion and Space Contactor Research," NASA CR 175119, January 1986, pp. 81-82.

4. Aston, G., "Ion Extraction from a Plasma," NASA CR-1159 849, June 1980, pp. 12-19.

5. Hardy, T., private communication with Paul Wilbur, July 1986.

6. Davis, L., ed., Handbook of Auger Electron Spectroscopy, 2nd edition, Physical Electronics Industries, Eden Prarie, MN, 1976, p. 13.

AIAA'87

AIAA-87-1073

Constrained-Sheath Optics for High Thrust-Density, Low Specific-Impulse Ion Thrusters

P. J. Wilbur and J. Z. Han, Colorado State Univ., Fort Collins, CO

19th AIAA/DGLR/JSASS International Electric Propulsion Conference

May 11-13, 1987/Colorado Springs, Colorado

CONSTRAINED SHEATH OPTICS FOR HIGH THRUST DENSITY, LOW SPECIFIC IMPULSE ION THRUSTERS*

Paul J. Wilbur** and Jian-Zhang Han+
Colorado State University
Fort Collins, Colorado 80523

Abstract

The results of an experimental study showing that a contoured, fine wire mesh attached to the screen grid can be used to control the divergence characteristics of ion beamlets produced at low net-to-total accelerating voltage ratios are presented. The influence of free and constrained-sheath optics systems on beamlet divergence characteristics are found to be similar in the operating regime investigated, but it was found that constrained-sheath optics systems can be operated at higher perveance levels than free-sheath ones. The concept of a fine wire interference probe that can be used to study ion beamlet focusing behavior is introduced. This probe is used to demonstrate beamlet focusing to a diameter about one hundreth of the screen grid extraction aperture diameter. Additional testing is suggested to define an optimally contoured mesh that could yield well focused beamlets at net-to-total accelerating voltage ratios below about 0.1.

Introduction

The high specific impulse capabilities of ion thrusters have long been recognized as well suited to high characteristic velocity missions such as planatary and deep space probes. Over the past decade, however, most space programs have been directed more toward near-earth missions where low specific impulses are optimal. Under this condition where thrust densities also tend to be low, large numbers of ion thrusters are generally needed to develop desired thrust levels. The number of thrusters required could be reduced, however, if the thrusters could be operated at a low net accelerating voltage to achieve the low specific impulse and a high total accelerating voltage to achieve a higher thrust density. Both experimental and theoretical data have shown, however, that conventional (free-sheath), two-grid ion optics systems tend to exhibit high ion beamlet divergence and direct ion impingement losses when they are operated at low ratios of the net-to-total accelerating voltage (R).[1,2] Operation can be extended to lower net-to-total accelerating voltage ratios by using mechanically more complex three-grid ion optics systems but the associated reduction in net-to-total accelerating voltage ratio is still relatively modest.[2,3] The effort described here was undertaken to examine the possibility of constraining the shape of the sheath through which ions are extracted from the discharge plasma into the beam. This was persued on the premise that it could facilitate operation of two-grid optics systems at high current densities and low net-to-total accelerating voltage ratios without inducing the high beamlet divergence behavior that limits the performance of free-sheath optics systems.

In order to understand the mechanisms by which ions are accelerated and diverted from ideal, axial trajectories in typical ion-optics systems, it is instructive to consider the diagram shown in Fig. 1. This diagram shows equipotential contour lines associated with ion extraction from a flat plane at 500 V potential, acceleration through a 460 V screen grid aperture and a -2500 V accelerator grid aperture to a zero potential, flat plane at which neutralization of the ions is presumed to occur. The equipotential lines shown in the figure are the solid ones and the dotted line shows a conceptualized trajectory for an ion coming from the ion source plane and passing through the system at a substantial distance from the aperture pair centerline. The arrows emanating from the lettered points along the trajectory suggest the direction of electric field vectors along which forces act on the ions as they pass through the grid system. The arrow at position A suggests for example that electric field forces acting on an ion in the early phase of the acceleration process have both a downstream axial component and an inward radial component. This inward radial force component causes the ion to be directed closer to the aperture centerline as it accelerates between the grids and it continues to act until point B. The electric field contour at point B is flat and essentially perpendicular to the centerline. Beyond point B the

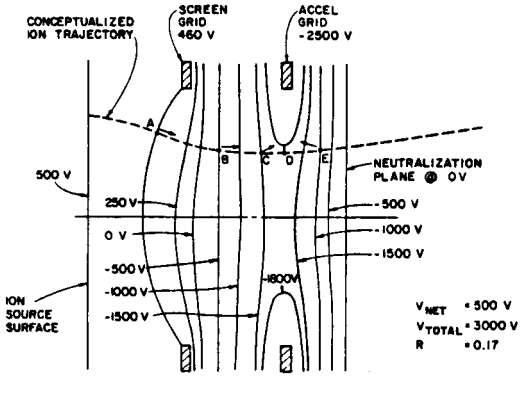

Fig. 1 Equipotential Contour and Ion Trajectory Diagram

*Work supported under Grant NGR-06-002-112 from NASA Lewis Research Center

**Professor, Dept. of Mech. Engineering, Member of AIAA

+Visiting Scholar, Dept. of Mech. Engineering, from Lanzhou Institute of Physics, Lanzhou, China

electric field vectors begin to have a component of electric field directed radially outward as shown at point C. At point D the ion begins to decelerate due to a component of electric field that is directed axially upstream and similar forces continue to act through point E and on to but not beyond the neuralization plane. Figure 1 taken in total shows that the ion sees an outwardly directed radial force component that causes it to diverge from point B to the neutralization plane. As the accelerator grid is biased more and more negative (i.e. the R value is reduced) the ion sees a component of outwardly directed electric field force that is increasingly greater in magnitude and acts for an increasingly greater fraction of the time associated with its passage through the optics system. This in turn results in greater ion divergence from the axial direction.

An ion moving along the aperture pair centerline on the other hand, passes through equipotential surfaces that remain perpendicular to the centerline throughout its time of passage through the system. This ion therefore sees no radial component of electric field and as a result it does not diverge from an axial trajectory. One can see from this discussion that both the radial location at which an ion begins the acceleration process and the net-to-total accelerating voltage ratio influence the divergence angle associated with the ion at the time it passes the neutralization plane. One can also see that low divergence operation at a low net-to-total accelerating voltage ratio could be achieved if the bulk of the ions extracted from the discharge plasma could be directed through the grids along trajectories that follow the aperture pair centerline.

If ions were to be extracted at an ion source surface contoured in such a way that they would all be directed toward the aperture pair centerline, one might be able to minimize the radial force components and thereby minimize the mean divergence of the beamlet exiting the grid system. In contact ion thrusters[4] and in electron beam forming systems that utilize an "emission grid"[5] this type of source surface forming is used to induce and sustain optimal focusing over a relatively wide range of emission current and accelerating voltage conditions. In conventional two and three-grid ion optics systems used with electron bombardment discharge chambers, on the other hand, the ion source surface shape, i.e. the ion extraction sheath shape, is determined by the requirement that the rate at which ions are supplied from the discharge be equal to the rate at which they are extracted through the optics system. Hence changing the discharge plasma density or the total accelerating voltage causes the sheath to move until it assumes the shape that will assure continued operation at the new space-charge-limited condition. In this "free-sheath" case "the ion source surface" moves as operating conditions change and as a result the divergence character of the beam also changes. Optimal focusing may as a result not be achievable and near-optimal focusing will probably be realized at only one beam current for each accelerating voltage condition. If on the other hand one could apply a properly shaped fine wire mesh over the screen aperture it might be possible to establish an "ion source surface" having any desired shape ("constrained sheath"). It is conceivable that this shape could be selected so it would induce optimal focusing over a wide range of beam current and accelerating voltage conditions. Presumably the mesh would be shaped in this case to direct the ions along trajectories that would pass near by and parallel to the aperture pair centerline where low-divergence operation at low net-to-total accelerating voltages could be achieved.

The suggestion that a mesh could be used to control the shape of an ion emission surface in an electron bombardment ion source and thereby decouple the ion extraction and beamlet formation process from the ion acceleration and deceleration process appears to have been suggested first by Reifenschweiler and Fröhner.[6] They investigated this concept at high net accelerating voltages (20 to 100 kv) and high net-to-total accelerating voltage ratios and found that it did facilitate ion divergence control. Byers[7] also attempted to operate at high net accelerating voltages but found that his screen-constraining mesh melted as a result of heating by secondary electrons generated as a result of ion bombardment of the accelerator grid. Subsequent experiments[8] again conducted at high net accelerating voltages have verified that a sheath constraining mesh can be 1) used to control beamlet focusing by controlling the mesh contour, 2) used to hold the beamlet divergence constant as beam current and/or accelerating voltage is varied over a wide range and 3) made to tolerate high heat fluxes without melting if the mesh is made of tantalum wire. In a related series of tests Aston[9] used the concept of decoupling ion extraction and acceleration with somewhat different apparatus than other investigators have employed to generate well-focused beams.

Apparatus and Procedure

In order to conduct these experiments a sheath constraining mesh was spot welded to the screen grid aperture of an ion source. It served as an interface between the discharge plasma and the ion acceleration region established through the screen and accel grids and was arranged as shown in Fig. 2. This figure also shows the symbols used to define such dimensions as the diameters of the screen and accelerator grid apertures (d_s and d_a), the spacing between them (l_g) and their thicknesses (t_s and t_a). For all cases considered in this study, the sheath constraining mesh was made of 0.25 mm dia tantalum wire formed into a square mesh with a ~ 2mm wire-to-wire spacing (~ 88% open area). For all tests the mesh was formed into a spherical segment contour defined by a radius curvature r_c as illustrated in

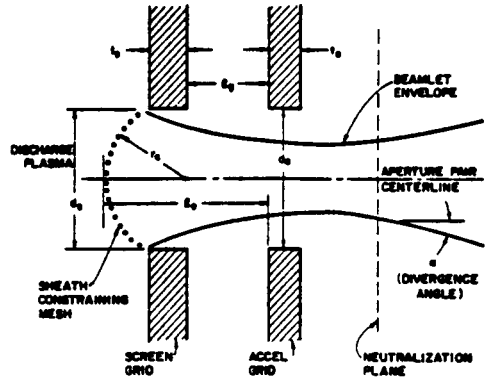

$$\left(\frac{t_s}{d_s}\right)^2 \cdot \left\{\frac{t_s}{d_s} + \frac{l_g}{d_s} + \frac{t_a}{d_s}\left(1 - \cos\left[\sin^{-1}\left(\frac{d_s}{2r_c}\right)\right]\right)\right\}^2$$

Fig. 2 Constrained-Sheath Ion Extraction and Acceleration System Schematic

Fig. 2. This mesh contour was selected, though it was considered suboptimal, because it could be generated reproducibly using molds having the desired radii of curvature.

The effective acceleration length ℓ_e, which is shown in Fig. 2, is defined in terms of the other geometric parameters by the equation given below the figure. This length was used to compute the perveances that were used as the independent variable in presenting beamlet divergence data. The beamlet divergence half-angle (α in Fig. 2) is defined as the half-angle of the cone with its apex at the accelerator grid which encloses 95% of the beamlet current being extracted through the grid system.

The bulk of the tests were conducted using an 8 cm dia ring cusp ion source having a single, centered, 2.9 cm dia screen aperture at its downstream end. All tests were conducted using argon propellant and the ion beam current density profile used to develop beamlet divergence data were measured 10.6 cm downstream of the accelerator grid using a Faraday probe that could be swept across the beam and could detect ions passing the neutralization plane with divergence half-angles less than 50°. Reference 8 gives the design details of the ion source and Faraday probe system used. In order to conduct the tests a stable argon discharge was established in the ion source and the screen and accelerator grids were then biased to achieve the desired net and total accelerating voltage condition. The ion source discharge current was increased in steps and ion beam current, impingement current and current density profiles were measured at each operating condition. The ion beam current was measured directly using the beam current meter and was compared to that determined indirectly by integrating the beam current density profile. The extent to which the integrated beam current agreed with the directly measured one was used as a measure of the fraction of ion trajectories that were so divergent that their contribution to the integrated beam current could not be detected by the Faraday probe.

During one of the tests the 0.25 mm dia. tungsten wire neutralizer that extended diametrically across the accelerator aperture happened to be positioned exactly on the centerline of the single beamlet being studied and it was observed on the current density profile that this wire intercepted a substantial portion of the beamlet. The apparatus was subsequently modified so the wire could be moved both along and normal to the beamlet centerline while the source was operating. With this arrangement it was possible to use the wire as a probe suitable for investigating the structure of the focused beamlet. The location of this wire (interference) probe relative to other critical elements of the test apparatus is shown in Fig. 3. This figure also shows the position of the ground screen which was kept centered so it would have a reproducible effect on beamlet ion trajectories. The distance Z, which could be varied, represents the axial location of the centered probe measured from the accelerator grid. The distance Y is the height of the umbral portion of the shadow (i.e. zero current density portion) cast by the wire on the current density profile. The beamlet envelope trajectory shown in Fig. 3 is indicative of typical outermost trajectories that were detected using the Faraday probe.

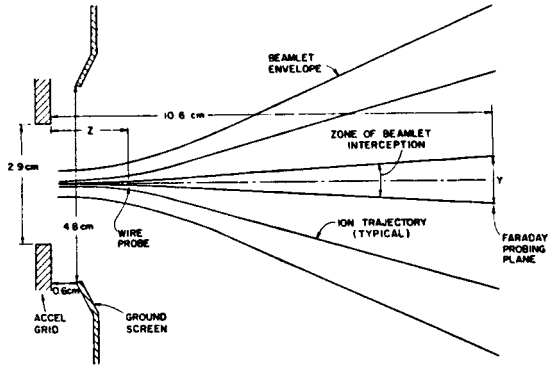

Fig. 3 Conceptual Diagram Showing Interference Wire Probing of Beamlet

While most of the testing was conducted using the single aperture extraction grid pair, one set of tests utilized a seven aperture pair. This grid set had screen and accelerator grid holes that were both 1.1 cm in diameter so the total screen (and accel) aperture area was the same as that associated with the single aperture system. The center-to-center spacing for the apertures in this grid system was 1.2 cm and its divergence characteristics were also determined using current density profiles measured using the Faraday probe described previously.

Results

It is convenient to present grid performance data in terms of normalized perveance per hole so the effects of changes in accelerating voltages, grid spacing and aperture diameter on beam current will be normalized properly and the effects of parametric changes on beamlet divergence can be compared. Normalized perveance per hole is defined in this report by the equation

$$\text{Perv} = \frac{J_B}{V_T^{3/2}} \left(\frac{\ell_e}{d_s} \right)^2 \qquad (1)$$

where J_B is the beam current per hole, V_T is the total accelerating voltage, ℓ_e is the effective acceleration length (defined in Fig. 2 for a constrained sheath) and d_s is the screen hole diameter. In order to evaluate the appropriateness of Eq. 1 for the various grid systems being studied at low net-to-total accelerating voltage ratios, data like those shown in Fig. 4 were collected. These typical data show a 3/2 power dependence between the maximum beam current that could be extracted from the grids and the applied total accelerating voltage and they thereby confirm the suitability of perveance as a correlating parameter for both constrained (circles and triangles) and free (squares) sheath optics systems. The maximum beam current in these tests was found by increasing discharge chamber power to the point where accelerator grid impingement current was increasing at the same rate as the screen current. The data of Fig. 4 also show that typical free and constrained-sheath, single-aperture optical configurations result in the same maximum beam current accelerating voltage correlation and that the seven aperture maximum beam current per hole is lower at a given total accelerating voltage. The lower beam

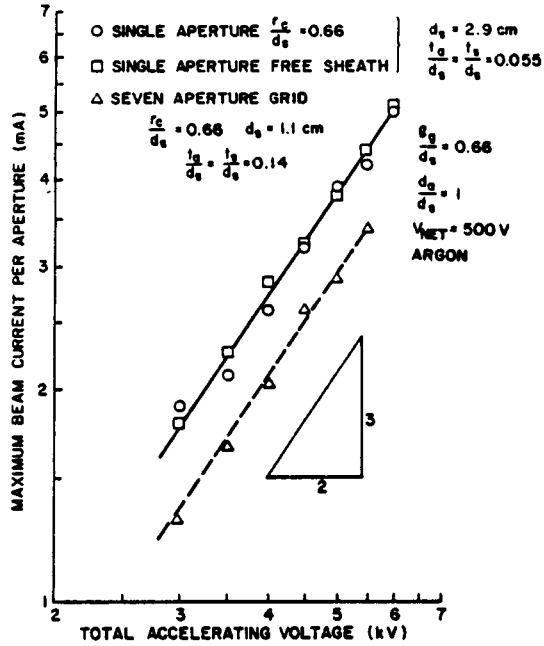

Fig. 4 Correlations Between Maximum Beam Current and Total Accelerating Voltage

currents associated with the seven aperture set may be related to the fact that the normalized grid and mesh wire thicknesses were greater for it.

Divergence Characteristics of Constrained-Sheath Optics Systems

Three ion beam profiles showing the typical progression of the beam profile structure with increases in perveance observed with the single-aperture, constrained-sheath optics apparatus are shown in Fig. 5. At low perveance values the

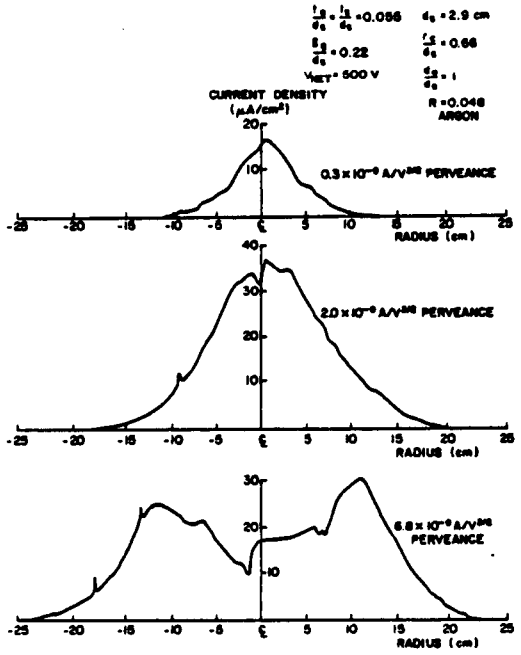

Fig. 5 Typical Constrained-Sheath Optics Current Density Profiles

profiles are gaussian in shape, however, at high perveance values they tend to bifurcate producing two peaks away from the centerline of the beamlet. It is suggested that this bifurcation might be due to either repulsion forces that tend to develop when too many ions are forced along the centerline of the apertures or else to ion trajectory crossover behavior which could be induced at high perveances.

In order to characterize the current density profiles, measured data like those of Fig. 5 were put into a computer program which generated a polynomial curve fit of the data. These curve fits were then integrated to determine a beam current and the beamlet divergence half angle. The half angle was found by first determining the radial distance to which the profile had to be integrated to obtain a beam current that was 95% of the total integrated beam current. The arc tangent of this radius divided by the distance from the accelerator grid to the probing plane yielded the desired half-angle. The computer program was also used to determine the ion beam divergence factor which is defined as the ratio of the thrust produced by the beam to the maximum thrust that would be produced if all of the ion trajectories leaving the aperture system were parallel to the aperture pair centerline. The computer program determined this factor by integrating the product of the current density and divergence angle cosine over the complete current density profile.

Typical results obtained from experimentally measured beamlet profile data like those in Fig. 5 are shown in Fig. 6. These plots of beamlet divergence angle and divergence factor as a function of

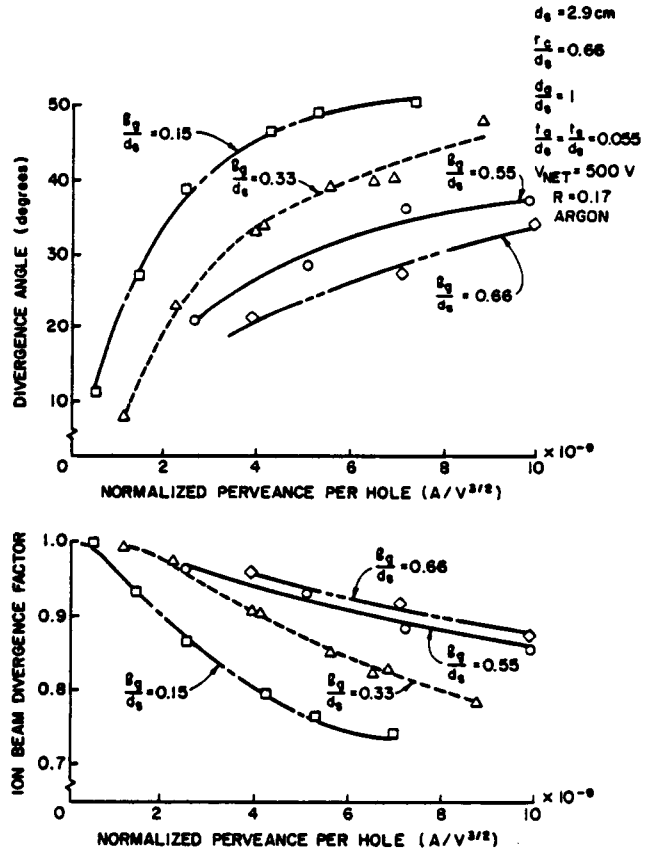

Fig. 6 Effect of Grid Separation on the Divergence Characteristics of Constrained-Sheath Optics Beamlets

normalized perveance per hole show the effect of changes in normalized grid separation distance on beamlet divergence when the other parameters are held constant at the values defined in the legend. The general trend suggested is that divergence angle increases substantially as normalized perveance per hole is increased with closely spaced grids. These increases in divergence angle are reflected as a reduction in ion beam divergence factor with values extending as low as about 0.75 for closest grid spacing. As grid separation is increased the extent to which changes in perveance influence the divergence angle and divergence factor is reduced substantially. It should be noted that the net-to-total accelerating voltage ratio for these data is 0.17 and the lowest value of net-to-total accelerating voltage ratio investigated by Aston for two-grid free-sheath, multiaperture optics systems was about twice this value.[1] He reports that attempts to operate at lower net-to-total accelerating voltage ratios resulted in poor divergence characteristics and high impingement currents. In the case of the free sheath data of Ref. 1 the adverse effect of perveance on divergence angle was much more subdued than the constrained-sheath data of Fig. 6 and divergence angles less than 20° were generally observed.

One startling feature of the data of Fig. 6 is the maximum normalized perveance at which data were obtained. It was expected that the sheath-constraining mesh on the screen grid would collect a portion of the ion current and hence the maximum normalized perveance at which the grids could be operated would be substantially below the theoretical limit which for argon is 6.8×10^{-9} A/V$^{3/2}$. In the present case, however, normalized perveance values approaching 10×10^{-9} A/V$^{3/2}$ are achieved. It could be that the high perveance is realized because the constrained sheath, which remains fixed in space, continues to maintain a large sheath area exposed to the discharge plasma as the plasma density is increased. In the free-sheath case, on the other hand, the sheath collapses toward a plane at the screen grid thus reducing its effective area for the discharge chamber ion extraction as plasma density is increased.[10] The high perveance realized in the present case could, however, also be related to the definition of the effective acceleration length ℓ_e identified in Fig. 2. This length which extends from the upstream plane of the accelerator grid to the upstream tangent to the sheath constraining mesh is appropriate for ions passing on the centerline of the extraction system, but may be too long for ions extracted from the discharge near the screen grid edge. Finally regarding the ion beam divergence factors in Fig. 6, it is noted that beamlet divergence induces some thrust loss, but this loss may be more than compensated by the capability of the constrained-sheath optics system to operate at higher total accelerating voltages where the current densities are higher than those that could be extracted from similar free-sheath optics systems.

The effect of changing the net accelerating voltage, while holding the net-to-total accelerating voltage ratio and the geometrical factors associated with the constrained-sheath optics system constant, is shown in Fig. 7. These data indicate that reducing the net accelerating voltage from 500 to 250 V induces no substantial change in divergence characteristics. In regard to the Fig. 7 data it is suggested that the triangular data point at the high perveance associated with 500 V operation is probably erroneous.

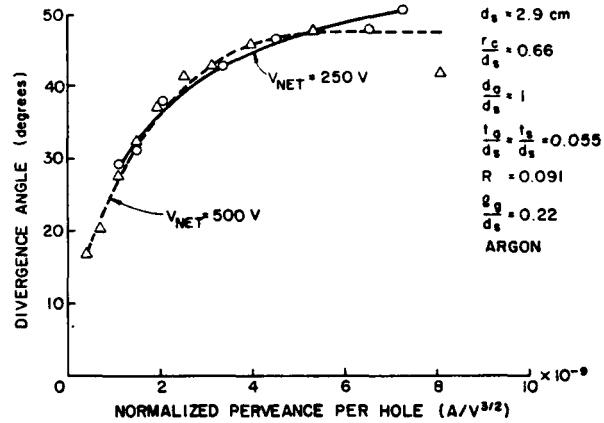

Fig. 7 Effect of Net Accelerating Voltage on Divergence Characteristics of Constrained-Sheath Optics Beamlets

The effect of changing the radius of curvature associated with the sheath constraining mesh is illustrated in Fig. 8. These data suggest that it is preferable to operate with the smaller radius of curvature mesh which presumably directs ions nearer to the aperture pair centerline where theory suggests the radial components of electric field that induce divergence are smaller. Figure 9 shows the effect of changing the net-to-total accelerating voltage ratio on divergence when the net accelerating voltage and geometrical factors are held constant. These data show decreases in divergence angle accompany increases in net-to-total accelerating voltage ratio. At high perveances, however, the data suggest the divergence characteristics at the two values of R may approach each other.

It is noted at this point that beam currents determined by integrating the current density profiles obtained at each operating condition agreed with the associated measured ion beam current to within about 10% when the net-to-total accelerating voltage ratio was 0.17 and above. As the net-to-total accelerating voltage ratio was reduced below 0.17, however, the integrated beam currents determined from current density measurements were systematically less than the measured ones. This effect is illustrated by the data of Fig. 10 which

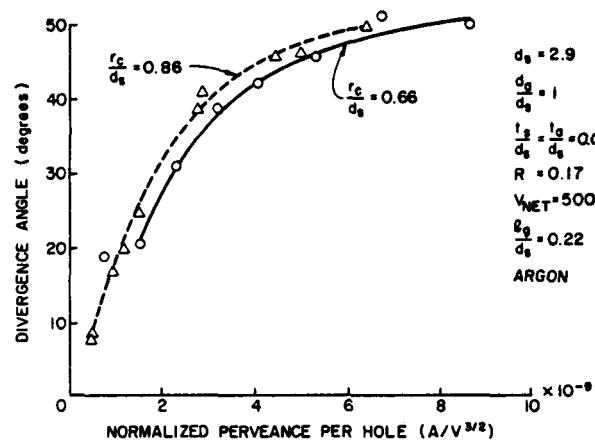

Fig. 8 Effect of Constraining Mesh Radius of Curvature on Divergence Characteristics

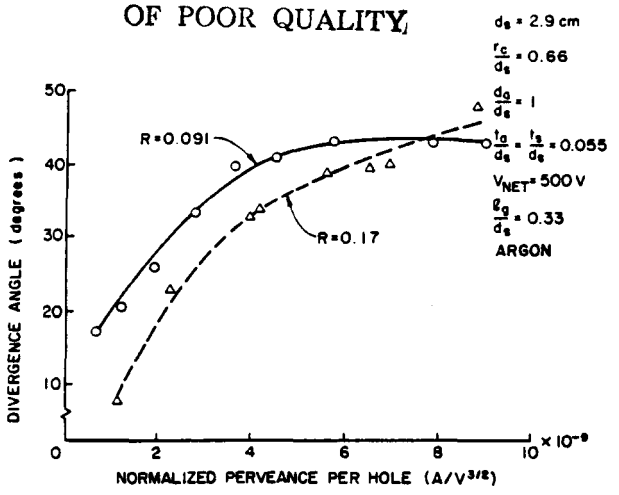

Fig. 9 Effect of Net-to-Total Accelerating Voltage Ratio on Divergence Characteristics of Constrained-Sheath Optics Beamlets

show integrated to measured beam current ratio dropping off as net-to-total accelerating voltage ratio is decreased for data obtained at a perveance of 4 x 10^{-9} A/V$^{3/2}$ and a wide range of other parameters. An integrated beam current that is less than the corresponding measured one is indicative of significant numbers of ions that are escaping on trajectories that are sufficiently divergent so they go undetected by the Faraday probe. These ions presumably pass through the plane of the Faraday probe at sufficiently large radii so that the integrated effect of their small current densities contributes substantially to the total ion current. Additional evidence that this was occurring was also provided by comparing current density profiles like those in Fig. 5 at different net-to-total accelerating voltage ratios (R). The current density profiles of Fig. 5, which were obtained at low R values, have a slope at the radius where current density drops to zero that also approachs zero. At high R values, on the other hand, the profiles at the zero current density point were more vertical. Based on the arguments presented regarding Fig. 1, it is suggested that the highly divergent ions are those which pass through the grid apertures sufficiently far from the centerline and so they see large radial components of electric field that induces their large divergence.

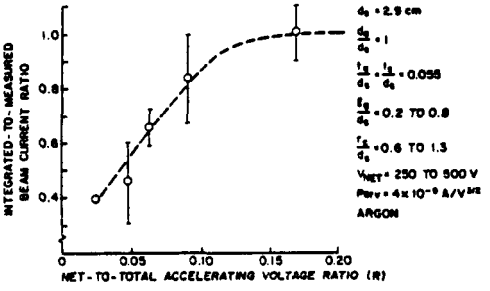

Fig. 10 Effect of Net-to-Total Accelerating Voltage Ratio on the Beam Current Fraction Detected by the Faraday Probe

Direct Free-Sheath/Constrained-Sheath Performance Comparisons

While the data in Figs. 6 to 10 suggest that constrained-sheath optics systems can be used to extract ion beamlets at low net-to-total accelerating voltage ratios, no direct evidence is presented to show that these grids produce beamlets that are less divergent than the free-sheath ones. In order to obtain a direct comparison of performance of free-sheath and constrained sheath optics a series of tests was performed first with a sheath-constraining mesh on the screen grid aperture and then again with it removed. In order to present the free-sheath data it was necessary to define an effective acceleration length (ℓ_e) to use in Eq. 1. For these data the length was defined as the distance from the centerline at the upstream plane of the accel grid to the upstream edge of the screen grid aperture.[1] Typical results obtained in these tests are shown in Figs. 11 and 12. Figure 11 presents beamlet divergence data obtained at two net accelerating voltages and two net-to-total accelerating voltage ratios which show that the constrained-sheath optics data obtained with meshes contoured to two different radii of curvature exhibit only slightly less divergent behavior than the free-sheath data. These data also show, however, that operation with the constrained-sheath optics facilitates operation to sightly higher normalized perveance levels. The data of Fig. 12 show that the free sheath optics systems operate at slightly higher impingement current levels than the constrained-sheath optics systems do and that the maximum perveance achievable before the onset of high direct ion impingement is greater with the constrained-sheath optics apparatus. Again, however, there is not a dramatic difference in the divergence data obtained using the two different sheath concepts.

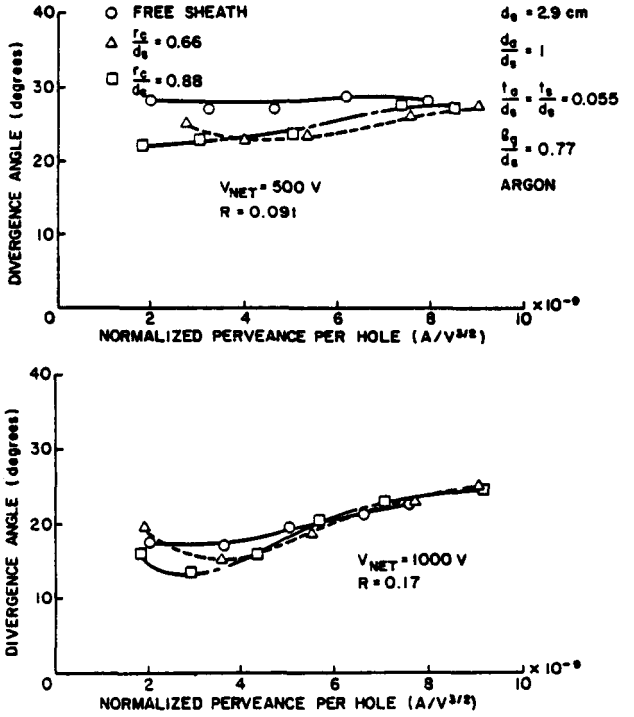

Fig. 11 Typical Divergence Characteristic Comparison Between Free and Constrained-Sheath Optics Systems

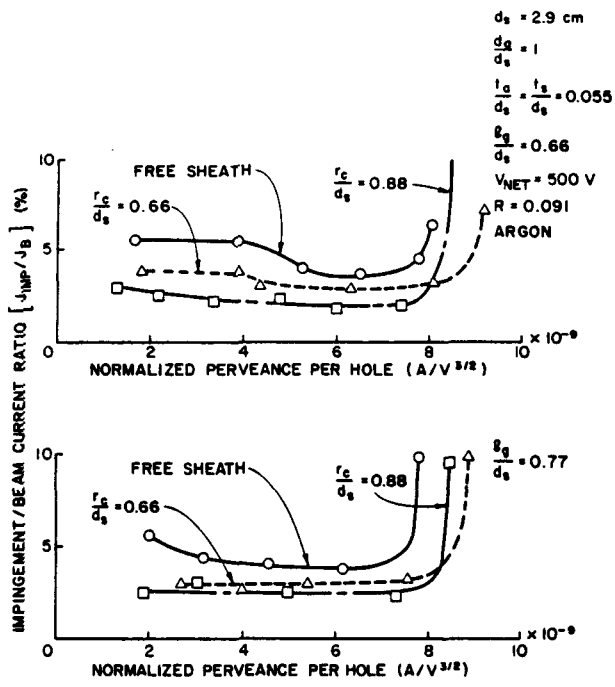

Fig. 12 Typical Impingement Characteristic Comparison Between Free and Constrained-Sheath Optics Systems

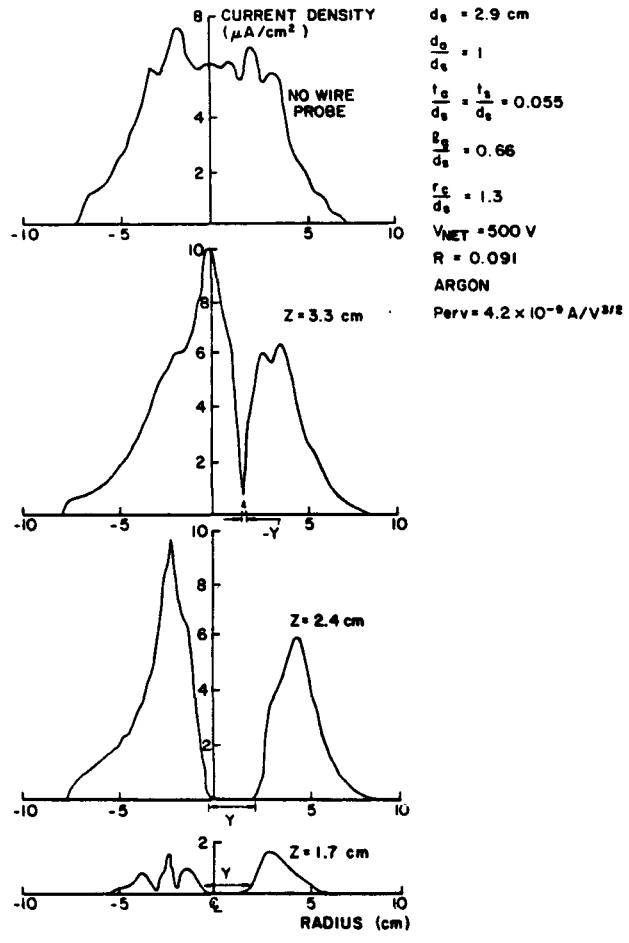

Fig. 13 Typical Beamlet Current Density Profiles Showing the Effect of Interference Probe Axial Position

Beamlet Interference Probing

When the fine (0.25 mm dia) interference probe shown in Fig. 3 was moved into the beamlet coming from a single aperture grid pair, it was possible to intercept a portion of the beamlet and cast a shadow onto the current density profile measured using the Faraday probe. Interpretation of the data obtained from such measurements provides some insight into the structure of the beamlet. It should be noted that it is probably convenient to make this type of measurement only on single aperture pair ion extraction systems where the results are not confused by the overlapping ion currents from adjacent apertures. Figure 13 shows a typical set of data obtained using a particular constrained-sheath optics grid pair operating at a perveance near 4 x 10^{-9} $A/V^{3/2}$. The progression of beamlet current density profiles begins at the top with the current density profile in its undisturbed state. Beneath this profile are other profiles measured as the interference probe was moved progressively closer to the accelerator grid i.e. the distance Z shown in Fig. 3 was decreased. As this distance is decreased the profiles show the probe casts a shadow with an increasingly greater umbral height (the distance Y defined in Fig. 3). It is noteworthy that the probe could be heated to thermionic emission temperatures or allowed to remain at room temperature and it could be biased over the range from zero to 30V below ground potential and the profiles like those shown in Fig. 13 remained unchanged. With the probe at Z = 3.3 cm the second profile in Fig. 13 is seen to be completely penumbral (negative Y). This profile also shows some evidence that the probe causes some of the ions to be deflected in such a way that the current density immediately adjacent to the wire increases (compare no-probe and Z = 3.3 cm cases). When the probe is moved to a position 2.4 cm downstream of the accel grid it casts a shadow that completely blocks a portion of the current density profile producing an umbral shadow of height Y. Moving the wire still closer (Z = 1.7 cm) results in a dramatic reduction of the current densities over the complete profile as the lowest plot shows. In this case it appears that the umbral shadow has about the same height as it has at a Z distance of 2.4 cm but the penumbral shadow extends over the entire profile. The most startling revelation associated with the data of Fig. 13 is that such a fine wire (0.25 mm) should be able to cast such a large shadow on the beamlet current density profile (2-3 cm at a location 10.6 cm downstream of the accelerator grid). The fact that it does suggests that the current being extracted passes through a very narrow zone (focal region) on the aperture pair centerline at a location a few centimeters downstream of the accelerator grid. This zone must have a diameter of the order of the wire (one hundreth of the accelerator grid aperture diameter) or the interference probe would be unable to intercept so much of it.

When data like those shown in Fig. 13 are plotted in the form of umbral zone height (Y) against wire axial position (Z) results like those shown in Fig. 14 are obtained. Negative values of umbral zone height shown in this plot correspond to profiles like the one for Z = 3.3 cm in Fig. 13 where the actual profile shows a completely penumbral

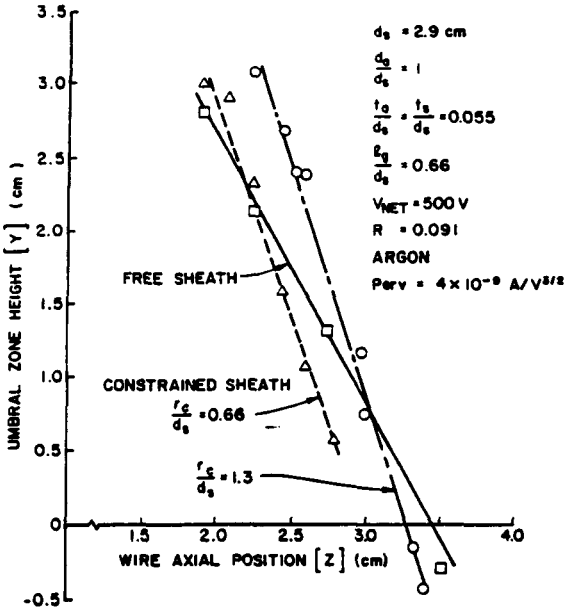

Fig. 14 Effect of Interference Probe Position on Umbral Shadow Height

interaction. Figure 14 shows a linear relationship between umbral zone height and wire axial position. It shows further that reducing the radius of curvature of the sheath constraining mesh causes the horizontal axis intercept of the line fitting the data to decrease, but does not change its slope. The results suggests that reductions in the constrained sheath radius cause the focal point of the emerging beamlet to move upstream but do not induce changes in the distribution of ion trajectories at the focal point. Changing from the constrained to the free-sheath configuration, on the other hand, causes the slope of the plots in Fig. 14 to change. This result indicates that a change in the sheath contour from from hemispherical to another one (the natural one in this case) does cause the distribution of ion trajectories at the focal point to change. This trend toward a zero slope characteristic in Fig. 14 as the sheath contour changes from spherical to free may be interpreted by recognizing that a horizonal characteristic would be produced by a beamlet composed of ion trajectories that all emerge parallel to the aperture pair axis. Hence the data of Fig. 14 suggest 1) the distribution of ion trajectories at the focal point can be controlled by controlling the sheath contour and 2) the free-sheath contour at a perveance of 4 x 10^{-9} $A/V^{3/2}$ is shaped to yield an ion trajectory distribution at the focal point that is closer to the ideal one (all parallel to the aperture pair axis). The spherical contour therefore does not produce the least divergent beamlet and it is also considered likely that the free-sheath one does not either. This suggests that improvements in the divergence behavior of ion optics systems could be achieved by using a constrained-sheath optics mesh contoured into another "ideal" shape.

The reason why the spherically-contoured constrained-sheath and free-sheath optics systems exhibit similar divergence characteristics (Fig. 11) can be understood by recognizing from Fig. 14 that both systems produce large umbral zone heights when a fine 0.25 mm dia. interference probe is placed into their beamlets. This indicates that both optics systems produce beamlets that focus into a small region at the aperture pair centerline in the operating regime under consideration. This in turn suggests that both systems induce trajectories that pass close to the aperture pair centerline where radial electric field components are minimal. As net-to-total accelerating voltage ratio (R) is reduced below ~0.1 the data of Fig. 10 suggest even the degree of focusing achieved with these grid sets is inadequate (the fraction of ions escaping Faraday probe detection increases markedly below this value of R). Hence even more precise ion trajectories, directed even closer and more nearly parallel to the aperture pair centerline are needed to reduce divergence at values of net-to-total accelerating voltage ratio below ~0.1.

Seven Aperture Grid Test Results

A final test sequence was conducted in which the single aperture constrained-sheath optics set was replaced with a seven aperture set having the same total aperture open area. Grid system parameter similarity was retained as the apertures were scaled down to the seven hole size (1.1 cm) except that the constraining-screen mesh wire and screen and accelerator grid thicknesses were not scaled but were the same absolute thickness for both grid sets. Figure 15, which shows the divergence characteristics of the seven aperture grid set compared to the single aperture set, indicates that the seven aperture set produces more divergent beamlets at a given perveance and that it cannot be operated at as high a normalized perveance per hole as the single aperture set can. This difference may be due in part to improper scaling of the grid and mesh wire thicknesses as the hole sizes were reduced to the values cited for the seven aperture set. The data of Fig. 15 do show, however, that screen grid apertures as small as 1.1 cm in dia. can be fitted with sheath-constraining meshes,, and it is believed that the concept can be scaled to even smaller aperture sizes.

Conclusions

A single aperture ion extraction system can be used to study the nature of the ion extraction process. Such a single aperture system can be probed

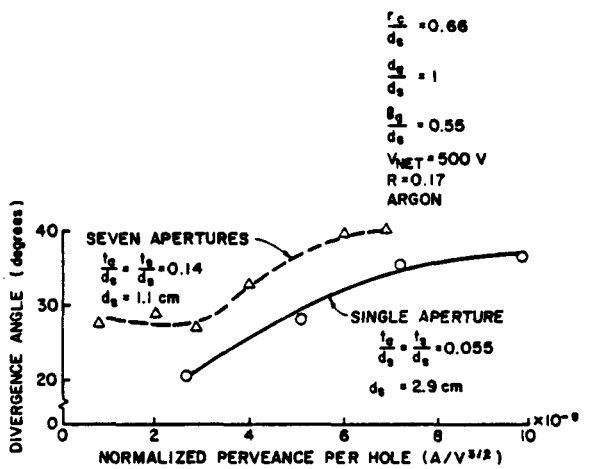

Fig. 15 Typical Comparison of Single and Multiaperture Constrained-Sheath Beamlet Divergence Characteristics

using a fine interference probe positioned just downstream of the accel grid which casts a shadow on the current density profile produced by the aperture set. A sheath-constraining mesh, attached to the screen grid can be used to control the position of the surface from which ions are extracted from the discharge plasma. When this constraining mesh has a spherical contour, it produces beamlets that have divergence characteristics similar to those observed when the constraining mesh is removed (free sheath case). Operation of both the free and spherically contoured constraining sheath grid systems at very low net-total accelerating voltages results in a beamlet that focuses into a region having a diameter of the order of one hundreth of the screen aperture diameter. This focal region is located at a point approximately one accel grid aperture diameter downstream of the accel grid. As net-to-total accelerating voltage ratio is reduced below about 0.1, the number of ions leaving the grid system on relatively divergent trajectories increases dramatically. It is believed, however, that proper contouring of the sheath-constraining mesh would produce an ion extraction surface that could cause the bulk of the ions to be directed onto trajectories passing still closer to and more nearly parallel to the aperture pair centerline at the focal point. This would be expected to produce low divergence beamlets at sill lower net-to-total accelerating voltage ratios. Sheath-constraining mesh wires do not appear to intercept a substantial fraction of the ions drawn through them. In fact constrained-sheath optics can even be operated at slightly higher perveance levels than free-sheath optics.

References

1. Aston, G., H. R. Kaufman and P. J. Wilbur, "Ion Beam Divergence Characteristics of Two-Grid Accelerator Systems," AIAA Journal, V. 16, No. 5, May 1978, pp. 516-524.

2. Kaufman, H. R., "Accelerator-System Solutions for Broad-Beam Ion Sources," AIAA Journal, V. 15, No. 7, July 1972, pp. 1025-1034.

3. Aston, G. and H. R. Kaufman, "Ion Beam Divergence Characteristics of Three-Grid Accelerator Systems," AIAA Journal, V. 17, No. 1, Jan. 1979, pp. 64-70.

4. Brewer, G. R., Ion Propulsion, 1970, Gordon and Breach, p. 185.

5. Spangenberg, K. R., Vacuum Tubes, 1948, McGraw Hill, pp. 348-349.

6. Reifenschweiler, O. and K. R. Fröhner, "A New Principle of Ion Extraction from a Gas Discharge Plasma," Nuclear Inst. and Meth., V. 30, 1964, pp. 298-302.

7. Byers, D. C., "Experimental Investigation of a High-Voltage Electron-Bombardment Ion Thruster," Electrochemical Science, V. 116, No. 1, Jan. 1969, pp. 9-17.

8. Wilbur, P. J. and L. O. Daniels, "The Development and Application of an Ion Implanter Based on Ion Thruster Technology," Vacuum, V. 36, No. 1-3, 1986, pp. 5-9.

9. Aston, G. and W. D. Deininger, "The DE-AC Accelerator System for High Beam Current Density," 17th International Electric Propulsion Conference Paper 84-85, Tokyo, Japan, 1984.

10. Aston, G., "Ion extraction from a plasma," J. Appl. Phys., V. 52, No. 4, April 1981, pp. 2614-2626.

DISTRIBUTION LIST

	Copies
National Aeronautics and Space Administration Washington, DC 20546 Attn:	
RP/Mr. Earl E. VanLaningham, MS B600	1
RP/Mr. Robert A. Wasel, MS B600	1
National Aeronautics and Space Administration Lewis Research Center 21000 Brookpark Road Cleveland, OH 44135 Attn:	
Technology Utilization Office, MS 7-3	1
Report Control Office, MS 60-1	1
Library, MS 60-3	2
Dr. M. Goldstein, Chief Scientist, MS 5-9	1
Mr. Dave Byers, MS 500-219	1
Mr. Jim Stone, MS 500-219	1
Mr. Vince Rawlin, MS 500-220	10
Mr. Bruce Banks, MS 302-1	1
Mr. Michael Patterson, M.S. 500-220	1
National Aeronautics and Space Administration Lyndon B. Johnson Space Center Houston, TX 77058 Attn:	
Dr. James E. McCoy, Code SN3	1
National Aeronautics and Space Administration Marshall Space Flight Center Huntsville, AL 35812 Attn:	
Mr. Robert Bechtel	1
Dr. Ralph Carruth	1
NASA Scientific and Technical Information Facility P.O. Box 8757 Baltimore, MD 21240 Attn:	
Accessioning Dept.	1
Dept. of the Navy Office of Naval Research Universiy of New Mexico Bandolier Hall West Albuquerque, NM 87131 Attn:	
G. Max Irving	1

	Copies
Case Western Reserve University 10900 Euclid Avenue Cleveland, OH 44106 Attn:	
Dr. Eli Reshotko	1
Procurement Executive, Ministry of Defense Royal Aircraft Extablishment Farnborough, Hants GU14 6TD ENGLAND Attn:	
Dr. D. G. Fearn	1
United Kingdom Atomic Energy Authority Culham Laboratory Abingdon, Oxfordshire OX143DB ENGLAND Attn:	
Dr. P. J. Harbour	1
Dr. A. R. Martin (Rm F4/135)	1
Intelsat M.S. 33 3400 International Dr. N.W. Washington D.C. 20008-3098 Attn:	
Mr. Rolland Schreib	1
Air Force Astronautics Lab Edwards AFB, CA 93523 Attn:	
LKDH/Lt. Robert D. Meya, MS 24	1
LKDH/Lt. Phil Roberts, MS 24	1
Giessen University 1st Institute of Physics Giessen, West Germany Attn:	
Professor H. W. Loeb	1
Jet Propulsion Laboratory 4800 Oak Grove Laboratory Pasadena, CA 91102 Attn:	
Technical Library	1
Mr. James Graf	1
Dr. Dennis Fitzgerald	1
Dr. Dave King	1
TRW Inc. TRW Systems One Space Park Redondo Beach, CA 90278 Attn:	
Mr. Sid Zafran	1

	Copies
National Aeronautics and Space Administration Ames Research Center Moffett Field, CA 94035 Attn:	
Technical Library	1
National Aeronautics and Space Administration Langley Research Center Langley Field Station Hampton, VA 23365 Attn:	
Technical Library	1
Hughes Research Laboratories 3011 Malibu Canyon Road Malibu, CA 90265 Attn:	
Mr. J. H. Molitor	1
Dr. Jay Hyman, MS RL 57	1
Dr. J. R. Beattie, MS RL 57	1
Dr. J. N. Matossian, MS RL 57	1
Princeton University Princeton, NJ 08540 Attn:	
Dean R. G. Jahn	1
Dr. Arnold Kelly	1
Boeing Aerospace Co. P. O. Box 3999 Seattle, WA 98124 Attn:	
Mr. Donald Grim, MS 8K31	1
Lockheed Missiles and Space Co. Sunnyvale, CA 94088 Attn:	
Dr. William L. Owens Dept. 57-24	1
Rocket Research Co. P.O. Box 97009 Redmond, WA 98073-9709 Attn:	
Mr. William W. Smith	1
Mr. Paul Lichon	1
Electrotechnical Laboratory 1-1-4, Umezono, Sakura-Mura, Niihari-Gun Ibaraki, JAPAN Attn:	
Dr. Katsuya Nakayama	1

	Copies
Sandia Laboratories P. O. Box 5800 Albuquerque, NM 87185 Attn:	
Mr. Ralph R. Peters, Mail Code 4537	1
Mr. Dean Rovang, Mail Code 1251	1
Ion Tech Inc. 2330 E. Prospect Road Fort Collins, CO 80525 Attn:	
Dr. Gerald C. Isaacson	1
Dr. Dan Siegfried	1
Mr. Larry Daniels	1
EG & G Idaho P. O. Box 1625 Idaho Falls, ID 83401 Attn:	
Dr. G. R. Longhurst, TSA-104	1
Michigan State University East Lansing, MI 48824 Attn:	
Dr. J. Asmussen	1
Dr. M.C. Hawley	1
Aerospace Engineering Department Faculty of Engineering Tokai University Kitakanome, Hiratsuka-shi, Kanagawa-ken, JAPAN 259 Attn:	
Prof. Itsuro Kimura	1
Department of Electronics Tokyo National Technical College No. 1220-2 Kunugida-cha, Hachioji 193 Tokyo, JAPAN Attn:	
Mr. Susumum Masaki	1
Tuskegee Institute School of Engineering Tuskegee Institute, AL 36088 Attn:	
Dr. Pradosh Ray	1
Mr. Lee Parker 252 Lexington Road Concord, MA 01741	1

	Copies
Physics Department Naval Postgraduate School Monterey, CA 93943-5000 Attn: Dr. Chris Olson, Mail Code 61-OS	1
Dr. Kevin Rudolph MS M0482 Martin Marietta Aerospace P. O. Box 179 Denver, CO 80201	1
Dr. Ira Katz Systems, Science and Software P. O. Box 1620 LaJolla, CA 92038	1
Dr. David Finkelstein Physics Department Georgia Institute of Technology Atlanta, GA 30332	1
Dr. Rod Burton G-T Devices, Inc. 5705 A General Washington Dr. Alexandria, VA 22312	1
Instituto de Pesquisas Espaciais - INPE Library and Documentation Division C.P. 515 Sao Jose dos Campos - SP 12200 - BRAZIL	1
Mr. Curtis Haynes Teletronix Inc. MS 50-431 P. O. Box 500 Beaverton, OR 97077	1
W. J. Schafer Assoc. Inc. 1901 North Fort Meyer Dr., Suite No. 800 Arlington, VA 22209 Attn: Dr. Herbert Cohen Dr. Robert Vondra	 1 1
Electric Propulsion Laboratory, Inc. St. Rt. 2, Box 3406A Tehachapi, CA 93561 Attn: Dr. Graeme Aston Dr. John R. Brophy	 1 1
Internal Distribution Prof. Steve Robinson	 1

1. Report No.	2. Government Accession No.	3. Recipient's Catalog No.
NASA CR-182130		

4. Title and Subtitle	5. Report Date
ADVANCED ELECTRIC PROPULSION RESEARCH	Jan. 1988
	6. Performing Organization Code

7. Author(s)	8. Performing Organization Report No.
Paul J. Wilbur	
	10. Work Unit No.

9. Performing Organization Name and Address	11. Contract or Grant No.
Department of Mechanical Engineering Colorado State University Fort Collins, CO 80523	NGR-06-002-112
	13. Type of Report and Period Covered Annual Jan. 1, 1987-Jan. 1, 1988

12. Sponsoring Agency Name and Address	14. Sponsoring Agency Code
National Aeronautics and Space Administration Washington, D.C. 20546	

15. Supplementary Notes

Grant Monitor - Vincent K. Rawlin, NASA Lewis Research Center
Cleveland, Ohio 44135

16. Abstract

Experimental results are presented which show that hollow cathodes can be operated on ammonia but that sustained operation at the high pressures where arcjet thrusters operate (of order 1000 Torr) is difficult to achieve. The concept of using contoured, fine wire meshes attached across the screen grid apertures in an ion thruster to effect control of the ion beamlet divergence is introduced. The concept is compared to conventional (free sheath) ion extraction and is shown to be potentially attractive. The performance-related effects of changing the anode and cathode locations and of interchanging hollow cathode and refractory filament electron sources within an 8 cm diameter, argon, ring cusp ion thruster discharge chamber are examined experimentally. The effects induced in discharge chamber performance by changes in magnetic field strength and configuration and in propellant flow distribution are also measured. Results of these studies are presented in terms of changes in the parameters that describe the effectiveness of primary electron utilization and ion extraction into the beam. The apparatus and instrumentation that is being used to study hollow cathode operation at high electron emission levels (of order 100 A) is described. Preliminary results obtained on a hollow cathode operating at lower current levels, which indicate the apparatus and instrumentation are working properly and that analysis techniques being used to interpret the data are valid, are presented.

17. Key Words (Suggested by Author(s))	18. Distribution Statement
Electrostatic Ion Thruster Arcjet Thruster Hollow Cathode Ion Optics	Unclassified-Unlimited

19. Security Classif. (of this report)	20. Security Classif. (of this page)	21. No. of Pages	22. Price*
Unclassified	Unclassified	101	

* For sale by the National Technical Information Service, Springfield, Virginia 22161